UNIVERSIDAD
NACIONAL
DE COLOMBIA

TU
RP
Rheinland-Pfälzische
Technische Universität
Kaiserslautern
Landau

Physical processes influence on the dynamics of the main greenhouse gases in mountain tropical reservoirs

Eliana Bohórquez Bedoya

Joint Supervision of Doctoral Work

Universidad Nacional de Colombia
Faculty of Mines, Departament of
Geosciences and Environment
Medellín, Colombia

Technische Universität Kaiserslautern-Landau
Faculty of Natural and Environmental Sciencies,
Institute for Environment
Landau, Germany

2023

Physical processes influence on the dynamics of the main greenhouse gases in mountain tropical reservoirs

By

Eliana Bohórquez Bedoya

A dissertation submitted in partial satisfaction of the requirements for the degree of:

Doctor of Engineering - Hydraulic Resources by the Universidad Nacional de Colombia
Doctor of Natural Sciences by the Technische Universität Kaiserslautern-Landau

Supervisors:
Prof. Dr. Evelio Andrés Gómez Giraldo
Prof. Dr. Juan Gabriel León Hernández
Prof. Dr. Andreas Lorke

Joint Supervision of Doctoral Work

Universidad Nacional de Colombia
Faculty of Mines, Departament of Geosciences and Environment
Medellín, Colombia

Technische Universität Kaiserslautern-Landau
Faculty of Natural and Environmental Sciencies, Institute for Environment
Landau, Germany

2023

To my grandmother, in heaven

Science must be a place of peace, of cooperation, that leads human beings away from ambition and the selfish exercise of power, that sets an example to the world.

“Para la guerra, nada”
Marta Gómez

Declaration of originality

I declare the following:

I have read Agreement 035 of 2003 of the Academic Council of the Universidad Nacional de Colombia. "Regulations on Intellectual Property" and the National Regulations related to the respect of copyrights. This dissertation represents my original work, except where I have acknowledged the ideas, words, or materials of other authors.

Where ideas or words of other authors have been presented in this dissertation, I have made their respective acknowledgment by correctly applying the citation and bibliographic reference schemes in the required style.

I have obtained permission from the author or publisher to include any copyrighted material (e.g., tables, figures, survey instruments, or large portions of text).

Finally, I have submitted this dissertation to the academic integrity tool, as defined by the university.

____

Eliana Bohórquez Bedoya

8th-July-2023

Acknowledgements

Thank the Universidad Nacional de Colombia and the University Koblenz-Landau for providing me with an excellent educational infrastructure and teaching staff during my doctoral training.

To my professors Andreas Lorke, Andrés Gómez and Juan Gabriel León for their teaching, perseverance and trust in me.

To my family and life partner, for whom I have no words of gratitude enough. They are my daily motivation and what gives meaning to my life.

To all my colleagues at both universities, especially my friends Mónica Bonilla, María Angélica Prada, Isabel Pulgarín, Johana Yepes, Aleen Pertuz, Natalia Acevedo, Ricardo Román, Alejandro Cáceres, Alejandro Henao, Juan David Osorio, Diana Arroyave, Lina Ramírez, Sebastián Gómez, Mateo Bonilla, David Quintero, Edwin Echeverry, Edwin Puerto, Laura Rodríguez, Clara Mendoza, Mayra Ishikawa, Gerrit Rau, Lediane Marcon and all those I forget to mention, to whom I owe the coffee breaks and sharing times that allowed me to endure this hard process with satisfaction and happiness, for their advice, for their invaluable friendship, for the questions and answers, for the unconditional availability and help.

Many thanks to Victoria Ramírez, César Jaramillo, Lina Ramírez, Ricardo Román, Óscar Beltrán, Andrés Monsalve, Christoph Bors, Zhongyong Yang, Lianghong Long, Mayra Ishikawa and Juan Sebastián Navas who participated in the field and laboratory work.

Special thanks to the undergraduate student David Bedoya for all his support in Colombia during my stay in Germany and to Lorenzo Rovelli, postdoc at Landau with whom a great work was possible during my stay.

Thanks to the entities who founded my doctoral studies with the programs: Scholarship Program No. 757 - National Doctorates of the Ministry of Science, Technology and Innovation of Colombia; Research Grants - Short-Term Grants, 2019 (57440917) of the German Academic Exchange Service (DAAD) and the German Research Foundation (DFG).

And to Empresas Públicas de Medellín (EPM) for its support during the field work and supporting information. Thanks also to Rockland Scientific Inc. for the constant support microCTD data processing.

Resumen

Título: Influencia de los procesos físicos en la dinámica de los principales gases efecto invernadero en embalses tropicales de montaña

Los embalses tropicales están reconocidos como fuentes de gases de efecto invernadero (GEI) de importancia mundial. Zonas tropicales montañosas de gran desarrollo hidroeléctrico han sido escasamente estudiadas. El objetivo de este estudio es comprender la dinámica de los GEI en embalses tropicales de montaña. Se recolectaron datos de la dinámica estacional y diurna de GEI durante seis campañas de campo en el embalse Porce III, en los Andes colombianos, donde se evidenció la importancia de la producción óxica de CH_4 en la en la variabilidad del gas disuelto en superficie, así como la variación de los niveles de agua como factor incidente en los flujos de GEI a escala estacional. Se monitoreó el flujo de CO_2 en la interfaz agua-atmósfera del embalse con una técnica de alta resolución durante periodos de varias semanas, donde se infirió la importancia de la productividad primaria en el ciclo diurno de los flujos de CO_2, mostrando alternancia como sumidero-fuente, y se observaron pulsos de flujos de CO_2 a escala sinóptica como consecuencia de la ocurrencia simultánea de incrementos en las concentraciones superficiales y alta velocidad del viento. En experimentos de laboratorio, se encontró una relación entre la tasa de lluvia, la tasa de disipación de la energía cinética turbulenta y la velocidad de transferencia de gases, contribuyendo a la modelación de este fenómeno con aplicabilidad en aguas continentales. En general, los resultados obtenidos contribuyen al entendimiento de la dinámica de GEI en embalses tropicales eutrofizados.

Palabras clave: embalses tropicales de montaña, gases efecto invernadero, transferencia de gases en la interfaz agua-atmósfera, variabilidad estacional, ciclo diurno, tasa de lluvia.

Abstract

Title: Physical processes influence on the dynamics of the main greenhouse gases in mountain tropical reservoirs

Tropical reservoirs are recognized as globally important sources of greenhouse gases (GHG). Tropical mountainous areas of high hydroelectric development have been poorly studied. The objective of this study is to understand GHG dynamics in tropical mountain reservoirs. Data on seasonal and diurnal GHG dynamics were collected during six field campaigns in the Porce III reservoir in the Colombian Andes, where the importance of oxic CH_4 production in the variability of dissolved gas at the surface, as well as the variation of water levels as an incident factor in GHG fluxes on a seasonal scale, was evidenced. CO_2 flux at the reservoir water-atmosphere interface were monitored with a high-resolution technique over periods of several weeks, where the importance of primary productivity in the diurnal cycling of CO_2 flux was inferred, showing alternation as sink-source, and pulses of synoptic-scale CO_2 flux were observed as a consequence of the simultaneous occurrence of increases in surface concentrations and high wind speed. In laboratory experiments, a relationship was found between rain rate, turbulent kinetic energy dissipation rate and gas transfer rate, contributing to the modeling of this phenomenon with applicability in inland waters. In general, the results obtained contribute to the understanding of GHG dynamics in eutrophic tropical reservoirs.

Keywords: tropical mountain reservoirs, greenhouse gases, gas transfer at the water-atmosphere interface, seasonal variability, diurnal cycle, rainfall rate.

Contents

Pag.

1. Chapter 1: Introduction

1.1. The climate change and emissions from inland waters

Since the middle of the 20th century, the resulting data of both climate monitoring and atmospheric gases, allow to establish a recent empowerment of the greenhouse effect and its relation with the increasing of carbon dioxide in the atmosphere (Treut et al., 2007). In 1990, the Intergovernmental Panel for Climatic Change – IPCC, presented the first evaluation report which made official the theory that in addition to the natural greenhouse effect, our planet was in front of a substantial raising of the atmospheric concentrations of the greenhouse gases (GHG) caused by anthropic activities; carbon dioxide (CO_2), methane (CH_4), chlorofluorocarbons compounds (CFC) and nitrous oxide (N_2O), were highlighted as the main gases causing of that phenomenon (IPCC, 1990).

In 2013 the IPCC recognized inland waters: wetlands, rivers and lakes as natural sources of GHG (Ciais et al., 2013). At that time, inland waters had rarely been included in the terrestrial carbon balance at global or regional scales, even though they are parts of the terrestrial landscape (Bastviken et al., 2011; J. J. Cole et al., 2007). Several studies have feed estimates of emissions from inland waters showing that they are significant for global carbon balances, with CO_2 and CH_4 emissions estimated at 2.1 PgC yr^{-1} (Raymond et al., 2013) and 398 Tg CH_4 (9.95 CO_2 eq) yr^{-1} (Rosentreter et al., 2021) respectively, which may be regarded significant considering that land carbon sinks is $\sim$3.0 PgC yr^{-1} (Le Quéré et al., 2018). Reservoirs are continental aquatic ecosystems that, similar to natural lakes, are considered sites of intense carbon processing which produce huge amounts of greenhouse gases such as CH_4 and CO_2 related to anthropogenic origin but associated to natural processes, contributing to the global carbon budget (Deemer et al., 2016). Recently, in 2019, the IPCC included flooded lands in the guidelines for national greenhouse gas inventories (IPCC, 2019) as a result of the effort of the scientific community in studying these, so far overlooked, sources of GHGs.

Even though the recognizing of streams, rivers, lakes and reservoirs as important sources of GHG to the atmosphere is increasing (Borges et al., 2015), large uncertainty prevails in GHG flux global estimates for inland waters because the scarcity of available data, the heterogeneity of emissions according to geographic location as well as the high complexity and poor understanding of underlying processes and drivers (Borges et al., 2015; Bridgham et al., 2013; Paranaíba et al., 2018b; Raymond et al., 2013). Specially, large uncertainties in estimates of emissions from tropical inland waters requires studies at adequate temporal and spatial scales (Barbosa et al., 2020). In this sense, studies contributing to feed the available data and the comprehension of the processes involved in GHG emissions from reservoirs are needed.

1.2. GHG from hydroelectric reservoirs

Important research about GHG emissions from hydroelectric reservoirs conducted at different latitudes show that these systems emit gases to the atmosphere indicating that hydroelectricity is no so clean type of energy production and that, on the contrary, it is not carbon neutral (Barros et al., 2011; Deemer et al., 2016). GHG emissions from reservoirs have different pathways, at low hydrostatic pressure, bubbles or ebullitive fluxes are able to escape from the sediments directly into the atmosphere; there is also exchange of gases by diffusion at the water-atmosphere interface, and, in stratified reservoirs, the usually methane-enriched deep waters enter the turbines and the gases are released to the atmosphere (Bastviken et al., 2004a, 2008; Kemenes et al., 2016)

Many studies have concluded that reservoirs in tropical zones emit important amounts of GHG – mainly CO_2 and CH_4 - because of the high temperatures promoting the microbial activity and large amounts of flooded biomass including primary forests (Abril et al., 2005; Delmas & Galy-lacaux, 2001; Galy-lacaux et al., 1997). Several authors argue that emissions from tropical reservoirs could be representative of global gas balances (Abril et al., 2005; Galy-Lacaux, 1999; Guérin et al., 2006) and according to Raymond et al. (2013) tropical lakes and reservoirs which constitute only 2.4% of the global lake area contribute to 34% of the global CO_2 emission from lake systems. Nowadays, tropical hydroelectric reservoirs are recognized as possessing the highest mean GHG fluxes compared to reservoirs from boreal and temperate locations (Fearnside, 2015; Galy-Lacaux, 1999; Raymond et al., 2013; Soumis et al., 2005; L. Yang et al., 2014).

Most studies in tropical and equatorial regions have been concentrated in Amazonian basin and a few studies conducted in Ivory Coast (Africa), Australia and India have been published (Demarty & Bastien, 2011; Panneer Selvam et al., 2014), covering only some tropical environments such us equatorial forest, tropical forest, savannas, agricultural and urban areas (Demarty & Bastien, 2011; Galy-Lacaux, 1999). As different conditions of the ecosystem may influence GHG dynamics in reservoirs, studies in different environments are needed to understand the issues related to this topic.

In Colombia, a tropical South American country, hydraulic resources are of great importance for the energy sector as they contribute about 67% of the electricity production in this country (UPME, 2016a), which is still under development. Currently, there are about 7 large projects in the planning phase or under construction in Colombia (Opperman et al., 2017; UPME, 2016b). Most Colombian hydroelectric dams are built or planned in mountainous areas of the Andean region (UPME, 2016a), taking advantage of the topography for hydroelectric production.

Despite the importance of hydroelectric power in the national energy matrix, and the evidence that exists since the 1990s on the contribution of hydroelectric reservoirs to carbon emissions (Rudd, 1993), until now, published studies on GHG emissions in Colombian reservoirs and, in general, in mountain tropical reservoirs have been very scarce (Castro - González & Torres-Valdés, 2015) and very little is known about the processes that govern their dynamics.

1.3. Processes involved in GHG dynamics in reservoirs

River damming results in the inundation of large areas of natural terrestrial and aquatic ecosystems, followed by the death of associated vegetation and the permanent loss of a potential carbon sink (Soumis et al., 2005; L. Yang et al., 2014). Thus, reservoirs become a net source of GHGs that negatively affect the ecosystem enough to note an increase in GHG production, exceeding those of natural water bodies (Soumis et al., 2005).

After impoundment, degradation of organic matter (OM) from the flooded soil and plant biomass occurs under aerobic or anaerobic conditions, emitting C gases such as CO_2 and CH_4 (Abe et al., 2005; Barros et al., 2011; Soumis et al., 2005; L. Yang et al., 2014). These emissions from pre-existing biomass tend to reduce and stabilize over time (Rocha Lessa et al., 2015) and could be the main source of C gases in tropical reservoirs even 10 years after impoundment (Abril et al., 2005; Guérin et al., 2008). On the other hand, allochthonous and autochthonous OM are permanent sources of carbon available for decomposition, as OM inputs from inflows and runoff are continuous, as well as aquatic primary production, respiration and regrowth of plants during drawdown periods in the reservoir operation phase (Abril et al., 2005; Barros et al., 2011; Soumis et al., 2005).

One of the most important sources of C gases in reservoirs are bottom deposits, where waters and sediments are usually anoxic, especially in tropical regions (Abe et al., 2005; Barros et al., 2011; Soumis et al., 2005). Sediment has been considered as responsible for most of the CH_4 emissions in reservoirs through methanogenesis and part of the CO_2 emissions in smaller proportion (Abe et al., 2005; Wallin et al., 2016), although a large fraction of that CH_4 is oxidated to CO_2 by methanotrophic bacteria living at the oxic – anoxic boundary in the water column (Abe et al., 2005; Guérin et al., 2008). Importantly, recent studies provide evidence that the oxic water methanogenesis is also a significant component of the CH_4 budget in inland waters (Bogard et al., 2014; Günthel et al., 2019).

While biochemical mechanisms explain the processes of GHG production and transformation in reservoirs, physical processes control GHG fluxes and largely explain the spatial and temporal distribution of GHGs in waters. In a broad sense, physical processes affect the distribution of substances throughout the reservoir area and water column. Turbulent mixing (Bartosiewicz et al., 2015), thermal stratification (Boehrer & Schultze, 2009) and advective transport (Peeters & Kipfer, 2009) are considered the main processes involved in fluxes of dissolved substances and transport through reservoirs.

A significant fraction of GHG exchange in lakes and reservoirs occurs through diffusive flux at the water-atmosphere interface, where the gas moves from higher to lower concentrations, considering solubility factors. According to Fick's first law, the difference in concentration between water and air times gas transfer velocity (*k*) quantifies the flux. *k* is usually normalized for CO_2 at 20°C and is denoted k_{600} and this parameter is a function of physical processes, which require hydrodynamical forcings to make possible their occurrence or predominance. Thereby, forcings, most of them hydrometeorological in nature - wind, rainfall, heat exchange, and inflows - influence the C gases' emissions, storage, and distribution (Bartosiewicz et al., 2015; Wüest & Lorke, 2009).

1.4. GHG dynamics in mountain tropical reservoirs

Even though there is literature about the physical behavior of GHG in lakes and reservoirs, the heterogeneity of the lake systems makes it difficult to frame the dynamics of all the systems in a singular way. Particularly, tropical mountain reservoirs have a lot of different physical and biogeochemical conditions when compared to temperate and boreal lakes and reservoirs. Nevertheless, limnological studies about the GHG from the physical point of view in tropical lake systems are scarce.

Wind speed has been widely recognized as the main forcing affecting the gas transfer velocity in lakes and reservoirs, based primarily on studies in boreal and temperate areas. However, in mountainous areas, topography may function as a barrier to wind favoring the dominance of other physical processes rather than turbulent mixing produced by wind shear (Eugster, 2003).

Many studies around the world have highlighted the importance of seasonal variability in GHG emissions from lakes and reservoirs. In tropical areas, seasonal variability does not produce as strong changes in the physical conditions of the lake system compared to temperate areas, where between the summer and autumn seasons lakes can change from strong stratification to complete mixing as a result of seasonal variability. In contrast, at low latitudes, there is a constant weak stratification in the water column and the seasonal variability is determined by differences in precipitation rates between rainy and dry seasons, affecting runoff and promoting variations in the biochemical and physical conditions in the reservoir. In a broad sense, since inflow plumes are one of the most important processes of advective renewal in tropical systems (Peeters & Kipfer, 2009), it is expected that they have potential to affect the GHG dynamics. (Ojala et al., 2011) concluded that the link between catchment and the lake is strongly controlled by hydrological events after they found important increasing in the GHG fluxes during and just after the rains in two boreal lakes. These physical processes and their influence on the GHG behavior in lakes and reservoirs have not been broadly approached especially in mountain tropical systems.

In contrast to the widely studied seasonal dynamics of GHGs in lakes and reservoirs, diurnal dynamics have been scarcely addressed worldwide. Some studies have concluded on the physical processes that influence the diurnal behavior of GHGs in inland waters. In this regard, nocturnal changes in gas fluxes have been related to variations in day-night heat exchange patterns. (Liu et al., 2016) found that nighttime CO_2 fluxes were about 70% higher than daytime fluxes in a temperate reservoir, largely as a result of heat loss and wind-induced processes. (Poindexter et al., 2016) found, in a natural temperate wetland, that convection-enhanced diffusion contributed 54% of total nighttime CH_4 fluxes versus 18% of total daytime emissions. (Anthony & MacIntyre, 2016) consider that the implications of these dynamics for tropical systems may be large.

Short-duration events such as rainfall have also been recognized in some field studies to cause peaks in C gas fluxes; (Guérin et al., 2007a) obtained positive relationships between rainfall rates and CO_2 and CH_4 gas transfer rates and, for a diurnal scale, rainfall accounted for about 25% of the gas transfer rate in an Amazonian reservoir. Ojala et al. (2011) found changes in CO_2 and CH_4 flux during or just after rainfall in a boreal zone, resulting in CO_2 and CH_4 peaks responsible for 46% and 48% of the annual flux, respectively; although this study was conducted to assess seasonal patterns, it may indicate that point rainfall events may be potential sources of variability in C gas emissions on a shorter scale.

In Colombian mountain Andes, a region with significant hydroelectric development, the annual cycle is given by a bimodal rainy regime which monthly precipitation can increase around 10 times between the driest season and the rainiest season, but other weather features such as wind speed, solar radiation, air and water temperatures do not present large seasonal changes. Dynamics of GHG under these particular conditions are explored in this research work.

1.5. Research question and hypotheses

According to the scientific discussion around the knowledge of physical dynamics and the broad development of the biochemical principles of GHG in lakes and reservoirs and taking into account the national importance of the hydroelectric energy generation and hence dams and mountain reservoirs its long-term projection as well as the scarcity of physical-based GHG studies on these latitude and topographical environments, a research question arise:

How is the temporal behavior of the main GHG concentrations and emissions in mountain tropical reservoirs in function of the main physical processes and their hydro-meteorological forcings involved?

The following two hypotheses were tested in this research:

Convective mixing because of heat loss and turbulence from heavy rain events are the predominant physical processes determining of the GHG dynamics at diurnal scale in tropical mountain reservoirs. Likewise, variations of the mean rainfall and the characteristics of the inflow plumes along an annual cycle based on the rainy regime could explain the seasonal dynamics of GHG in tropical mountain reservoirs.

1.6. Objective and scope

In order to response the research question this thesis worked on the following objective:

To explain the interaction between the gas’s generation and transformation processes and the dominant physical processes involved in the temporal dynamics of the main GHG emitted from mountain tropical reservoirs

The specific objectives initially proposed for this research work were as follows:

1. To recognize the set of laws, theories and concepts related to the production and transformation of GHG in aquatic ecosystems and the transport of substances in lake systems.

2. To identify the susceptible variables to be related to the understanding of the production and transformation of GHG and the physical processes involved in the dynamics of the main GHG emitted from mountain tropical reservoirs.

3. To characterize the main production, transformation, and physical processes and their hydrometeorological forcings which influence the behavior of the GHG generation, transport, mixing, transformation and air-water transfer in tropical mountain reservoirs.

4. To conceptualize the dynamics of the GHG in function of the interactions between the main processes of substances production and transformation and the dominant physical based on hydrometeorological forcings which take place in tropical mountain reservoirs.

Throughout Chapters 2, 3 and 4, the objectives stated in the proposal will be resolved and chapter 5 synthesizes each one of them. Recognizing the theory behind the processes involved and identifying the variables to be related to GHG dynamics in tropical mountain reservoirs was necessary to formulate the objectives of each study in the framework of this thesis as well as the methodology and discussion of the results. The characterization of the processes involved in GHG dynamics in tropical reservoirs was carried out through field work in two stages (Chapters 2 and 3) and, additionally, the interest in understanding the possible effects of rainfall, as one of the main distinctive variables of tropical zones, on gas exchange at the water-atmosphere interface, led this research to carry out laboratory experiments not initially considered (Chapter 4). Finally, the synthesis of results and their discussion led to a conceptualization of GHG dynamics in tropical mountain reservoirs (Chapter 5).

Chapter 2 is planned to be submitted to indexed Journal as research article. The coauthors contribution is as follows:

- Eliana Bohórquez-Bedoya: Project administration, Field work, Conceptualization, Formal analysis, Data Curation, Writing-Original Draft, Visualization, Editing.
- Juan Gabriel León-Hernández: Funding acquisition, Conceptualization, Methodology, Field work, Formal analysis.
- Andreas Lorke: Conceptualization, Formal analysis, Writing-Review and Editing.
- Andrés Gómez-Giraldo: Funding acquisition, Project administration, Conceptualization, Methodology, Field work, Formal analysis, Writing-Review and Editing.

Chapter 3 is planned to be submitted to indexed Journal as research article. The coauthors contribution is as follows:

- Eliana Bohórquez-Bedoya: Funding acquisition, Project administration, Conceptualization, Methodology, Field work, Formal analysis, Data Curation, Writing-Original Draft, Visualization.
- David Bedoya-Taborda: Field work, Data Curation, Formal analysis.
- Andrés Gómez-Giraldo: Project administration, Field work, Writing-Review and Editing

Chapter 4 has been published on a pre-print server and can be found in: https://www.essoar.org/doi/10.1002/essoar.10509986.1. The manuscript is currently under review at the Journal of Geophysical Research: Biogeosciences. The coauthors contribution is as follows:

- Eliana Bohórquez-Bedoya: Funding acquisition, Laboratory work, Formal analysis, Data Curation, Writing-Original Draft, Visualization, Editing
- Lorenzo Rovelli: Conceptualization, Methodology, Laboratory work, Formal analysis, Writing-Review and Editing.
- Andreas Lorke: Funding acquisition, Conceptualization, Methodology, Formal analysis, Writing-Review and Editing.

2. Chapter 2: Surface CO_2 and CH_4 dynamics in a eutrophic tropical Andean reservoir

2.1. Introduction

Reservoirs emit globally significant amounts of greenhouse gases (GHG) such us carbon dioxide (CO_2) and methane (CH_4) to the atmosphere, following the decomposition of organic matter in the sediments and water column (Deemer et al., 2016; Rudd, 1993; Soumis et al., 2005). Although there is still a high uncertainty, recent estimates suggest that reservoirs represent approximately between 1.3% and 7% of anthropogenic CO_2 equivalent emissions over a 100-year period (Deemer et al., 2016; St. Louis et al., 2000). Tropical inland waters were recognized as particularly strong sources, compared to those located in the boreal and temperate zones, because of the high content of organic matter and favorable temperature for microbial activity all year round (Ciarlini et al., 2019; Fearnside, 2015; Kemenes et al., 2011; Raymond et al., 2013; Soumis et al., 2005).

In freshwater reservoirs, CO_2 and CH_4 can be produced and consumed through biochemical processes occurring in the sediment and in the water column, and surface emission rates are additionally affected by vertical transport processes in the basin interior and at the water surface (Soued & Prairie, 2021). Turbulent mixing produced by wind stress (Bartosiewicz et al., 2015; Wüest & Lorke, 2009), convective mixing caused by surface cooling (MacIntyre et al., 2010; Monismith & MacIntyre, 2009), and advective transport (Boehrer & Schultze, 2009) are the main physical processes involved in transport and evasion of dissolved gases from the reservoir.

Typically, reservoirs are characterized by longitudinal gradients from the riverine inflow to the dam, as well as by high temporal variability of hydrodynamic transport processes in response to meteorological forcing, at seasonal and diurnal scales. Primary productivity is also a major factor controlling the surface dynamics of CO_2 and CH_4 in aquatic systems

(Pacheco et al., 2013, 2015; Paranaíba et al., 2018a; West et al., 2016; Y. Yang et al., 2019) and eutrophic systems produce more of GHG emissions (Deemer et al., 2016). Thus, the interplay of dynamic physical drivers and production/consumption processes, such as photosynthesis, respiration, methanogenesis or methanotrophy, regulates the complex patterns and dynamics of atmospheric emissions. A mechanistic approach using a simplified mass balance of dissolved gas in the surface layer of a reservoir can be described in terms of the horizontal advection in the presence of longitudinal concentration gradients, vertical fluxes describing exchange with deeper layers, production/consumption of gases in the surface layer, and atmospheric evasion rates, which is mediated by turbulent mass transfer at the air-water interface (Bartosiewicz et al., 2015; Guérin et al., 2007b; MacIntyre et al., 2010).

Important and unvaluable effort has been done to understand emissions from tropical reservoirs (Kemenes et al., 2016; Melack et al., 2004, 2022). However, most studies of GHG in tropical reservoirs have been limited to plain zones in South America such us Amazon Forest and savannas, using mainly statistical approaches where physical and chemical variables are correlated to the GHG fluxes. Mechanistic approaches have been scarce and the processes that regulate the dynamics of gas fluxes in tropical reservoirs located in other biomes, such us the Andean mountains, are largely unknown. The objective of this study is to understand the dynamics of dissolved CO_2 and CH_4 concentrations in the surface layer of a eutrophic tropical Andean reservoir. The relative importance of physical and biochemical processes involved in the spatial, seasonal and diurnal dynamics of CO_2 and CH_4 is analyzed using a mass balance approach applied to observed concentrations and fluxes. Turbulence measurements are used to establish a first model for the gas transfer velocity for an Andean reservoir.

2.2. Methods

2.2.1. Study site

Porce III is a canyon type, long and narrow hydroelectric reservoir flooded in 2011, with a surface area of 4.61 km^2, 12 km length, and average and maximum depths of 45 m 137 m, respectively. It is located at 690 m.a.s.l. in wet tropical forest of the Colombian Andes, with average precipitation of ~2500 mm yr^{-1}, and is part of a series of cascading reservoir, with two reservoirs upstream (Troneras and Porce II). Its main tributary is the Porce river, which transports municipal wastewater from a metropolitan area with almost 4 million inhabitants and multiple land uses including urban, agricultural and industrial. The river is dammed upstream in the Porce II reservoir and reaches Porce III with significant concentrations of nitrate, ammonium and phosphate (Table S1). As expected from the morphology of the reservoir, the predominant direction of wind speed follows the canyon shape, and the main direction of the wind is from the north-east to the south-west in the morning and the opposite in the afternoon. Three sampling stations along the reservoir were selected to evaluate the longitudinal variability and were considered representative of three zones of the reservoir: transition zone (P3), medium lake zone (P2) and dam zone (P1), with 24.3 m, 53.0 and 112 m mean water depth, respectively, during the study period, (Figure 2-1) and variations of 1 m to 14 m in water level were observed between consecutive campaigns.

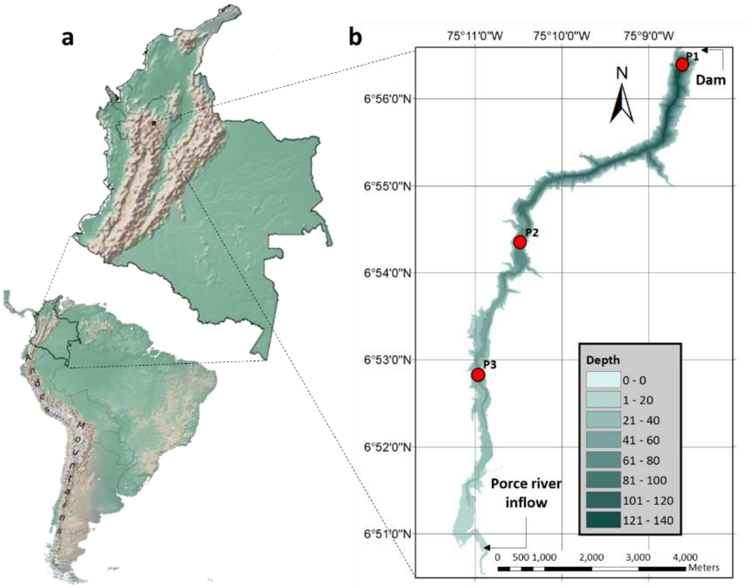

Figure 2-1. Porce III location and bathymetry of Reservoir. a) The continental and regional location showing the study area placed in the Colombian Andes. b) Bathymetry of the reservoir with color scale contours of the water depth, the location of the Porce river entry, the dam and the sampling stations.

2.2.2. Data collection

Hydrological and meteorological data were continuously collected from May 2017 to February 2019. Six field campaigns were carried out, the first in May 2017 and the remaining five between May 2018 and February 2019. The campaigns include periods of high (>673 m.a.s.l.), low (<665 m.a.s.l.) and medium (665 to 673 m.a.s.l.) water levels (Figure S1). Although the hydrology of the Porce III reservoir is mainly regulated by the operation of the upstream chain of reservoirs and by its own operation and not so much by the hydrological regime, we consider that the hydrological condition of the basin could be related to the state of water quality in the reservoir and, therefore, it is considered in the following analysis. Therefore, the field campaigns were named according to the basin's hydrological condition and the water level during the sampling period (Table 2-1). The first field campaign (C1-H-Wet) was only partially considered in the analysis, while for most analyses we considered the following five campaigns. Two field campaigns were affected by El Niño that is associated with drier weather in the study region.

Table 2-1. General description of the field campaigns. ID campaign indicates: campaign number (C1 to C6), water level condition (high level "H", low level "L", medium level "M") and basin's hydrological condition (Wet season "Wet", Dry-wet transition "DWT", Dry season "Dry"). *Based on the monthly reports from the Institute of Hydrology, Meteorology and Environmental studies of Colombia *-IDEAM)*

ID	**Date**	**Water level**	**Basin's hydrological condition***
C1-H-Wet	09 to 12 May/2017	High	Wet season
C2-H-Wet	08 to 12 May/2018	High	Wet season
C3-L-Dry	31 July to 02 Aug/2018	Low	Dry season
C4-L-DWT	18 to 21 Sep/2018	Low	Dry-wet transition
C5-M-Wet	13 to 15 Nov/2018	Medium	Wet season mitigated by the influence of a weak El Niño
C6-M-Dry	26 Feb to 01 Mar/2019	Medium	Dry season, accentuated by El Niño

Sampling at P1 was done three times a day: morning P1-M (08:00-12:00), afternoon P1-A (14:00-20:00) and night P1-N (22:00-03:00) to explore the diurnal dynamics. In the study zone, the daylight hours are very stable from 06:00 to 18:00 throughout the year, so some samples in the afternoon were taken during the first hours of darkness. During most of the campaigns, diurnal surface measurements were made twice a day at P3 and P2. For the spatial analysis we chose P1-M to be compared with P2 and P3 which were monitored mostly in the morning and midday.

2.2.3. Hydrological and meteorological data collection

A Davis Vantage Pro2 digital weather station was installed floating on the water surface (1.5 m height) near P1 allowed to rotate and a static WeatherHawk XP/X weather station was located on the dam. Both stations monitored meteorological variables including wind speed (~ 2.0 m above the water surface), air temperature, relative humidity, atmospheric pressure and solar radiation with a sampling resolution of 1 h. Data were also available from a fixed meteorological station (El Roble), located on land 2.7 km from the reservoir at coordinates 06°57'41.9"N, -75°07'55.7"W. The floating station was taken as the main data source for the analysis due to its ideal location in relation to the flux measurements, and missing data were filled after correlation with data from the other two stations (Table S2).

Surface water temperature was monitored with hourly resolution using Hobo thermistor located at 0.2 m depth at P1 and cloud cover was obtained from ERA 5 reanalysis data (Hersbach et al., 2020). The reservoir water level, inflows and outflows were provided by the operator of the reservoir at 1h resolution (Empresas Públicas de Medellín - EPM). Air temperature, relative humidity, cloud cover and wind speed were collected for the whole study period, while surface water temperature was collected for the campaign C1-H-Wet and then from C2-H-Wet onwards (Figure S2).

2.2.4. Physicochemical data and vertical structure

Vertical profiles of water temperature (*T*) and turbidity (*Turb*) were measured using a SeaBird CTD SB25 and profiles of dissolved oxygen concentration (*DO*) and *pH*, using a YSI EXO 1 multiparametric water quality sonde (MWQS). Vertical layering was defined from those profiles before sampling of CO_2 and CH_4 concentrations in each layer. The reservoir was divided in five layers from top to bottom: Surface mixed layer (SML), thermocline, over-plume layer (OPL), inflow plume and bottom. The selective withdrawal currents were always located in the layer defined by the plume (Figure S3).

Secchi disk depth (*SD*) was measured at least once during the diurnal sampling, except for the campaign C4-L-DWT. *SD* was taken as an indicator of the trophic status and although we did not measure it, high algae concentrations and green-colored water at the surface were always observed during the study period, especially during C2-H-Wet, C6-M-Dry and around P3 in C3-L-Dry.

2.2.5. Dissolved CO_2 and CH_4 in the water column

At least two samples were taken in the SML and one sample in the other layers to determine the concentration of dissolved CO_2 and CH_4 in the water column following its vertical structure. The samples were collected using a Mariotte bottle close to the surface (~ 0.20 m) and a UWITEC 5L vertical water bottle for deeper samples. The samples were immediately transferred to 20 mL vials, which were sealed and stored on the boat until the end of the data collection session and then preserved by adding $HgCl_2$. Samples were analyzed for CO_2 and CH_4 by gas-phase chromatography SRI (GPC) in the lab, using the headspace technique (Guérin et al., 2007b). Dissolved concentrations were computed using the temperature-dependent solubility coefficients: Henry (mol L^{-1} μatm^{-1}) and Bunsen (dimensionless) for CO_2 and CH_4, respectively (Wanninkhof, 2014).

2.2.6. Turbulence profiles

Direct velocity shear profiles were obtained with a microstructure profiler MicroCTD RSI, performing a minimum of three profiles. Data were not obtained for P1-M and P1-A in C5-M-Wet and all C6-M-Dry due to a damage of the instrument. Vertical profiles of dissipation rates of turbulent kinetic energy (ϵ_m) were estimated by processing the data from two shear probes and one micro-temperature probe (FP07). Each shear probe provides one component of the vertical gradient of horizontal velocity fluctuations, which are used to estimate ϵ_m for isotropic turbulence as described by (Lueck, 2016):

$$\epsilon_m = \frac{15}{2} v \overline{\left(\frac{\partial u}{\partial z}\right)^2} = \frac{15}{2} v \int_0^\infty \psi(\kappa)\,\mathrm{d}\kappa \tag{2-1}$$

where v is the kinematic viscosity of water, ψ is the power spectrum of the turbulent shear stress, $\frac{\partial u}{\partial z}$ is the vertical gradient of each component of horizontal velocity fluctuations, u or v, and κ is the wavenumber. Equation (2-1) applies equally to the component of shear $\frac{\partial v}{\partial z}$.

For each profile, a first idea of the order of magnitude of turbulent dissipation and the profiling velocity were obtained using conservative generic parameters to apply the algorithm in the software Matlab 2019. Once the order of magnitude of the turbulent dissipation rate is known, the algorithm is re-applied by changing the parameters by those with stablished criteria: the Nasmyth spectrum (Oakey, 1982), which represents the canonical expectation for a shear spectrum and is useful for judging a shear measurement (Lueck et al., 2013), is used to check the wavenumber and the minimum segment length (min_seg_length) for which a meaningful estimate of the integral of the spectrum can be obtained (0.5 -1.7 m). The min_seg_length was converted to time units by dividing by the profiling speed (0.5 - 0.9 m s^{-1}) using Taylor´s frozen hypothesis. For each estimate of the dissipation rate three segments were considered (diss_length = 3min_seg_length) and the overlap was half the estimated length (0.9 - 3 s).

The large segment lengths of the dissipation estimates, relative to those obtained when using the temperature microstructure, were due to the high profiling speed with the shear profiler and the nature of the Nasmyth spectrum, which is shifted to smaller wavenumbers than that of the temperature fluctuations (Bachelor spectrum). Individual ϵ_m profiles were obtained by averaging the profiles from both shear probes, then values every 0.50 m were obtained on every profile by cubic interpolation and finally a representative profile of ϵ_m was obtained by logarithmically averaging over 2-m bins. Smaller bins address to low statistical robustness.

Vertical turbulent diffusivity (K_z) was calculated as (Osborn, 1980):

$$K_z = \gamma_{mix} \frac{\epsilon_m}{N^2} \tag{2-2}$$

where γ_{mix} is the mixing efficiency estimated according to the turbulent intensity parameter dependent mixing regime, whether molecular, buoyancy-controlled, transitional or energetic ((Bouffard & Boegman, 2013) and N is the buoyancy frequency, defined by $N^2 = (g/\rho)(\partial\rho/\partial z)$, where g is the gravity acceleration, ρ is the temperature dependent water density and z is the depth.

Because of the large bins obtained from the shear profiles, the dissipation rates of the surface (0.15 m depth) were estimated by using parametrizations (see below).

2.2.7. Surface fluxes of CO_2 and CH_4, and k_{600}

Fluxes of CO_2 and CH_4 across the air-water interface were measured using floating chambers (Guérin et al., 2007a). Two chambers of ~ 40 L were deployed simultaneously. The plastic chambers were covered with aluminum tape to minimize heating inside the chamber (Vachon et al., 2010) and equipped with a valve for aeration and a butyl stopper that allowed gas sampling with a syringe and needle. The chambers were tied to the boat with a rope of 10 m length, one initial sample was taken right after deployment (0 min) and the chambers were allowed to drift for 15 min, then the chambers were gently dragged to the boat for sampling. This procedure was repeated three times for a total measuring period of 45 min. During each gas sampling, replicated samples (duplicates or triplicates) were obtained. After collection, samples were immediately stored in 5 mL vials previously sealed, and gas concentrations in the samples were analyzed by gas chromatography in the laboratory. Sample for measuring dissolved gas concentration in surface water (C_w) were collected at ~ 0.20 m depth the during chamber deployments and analyzed using the method explained above for dissolved gases (section 2.2.5). The fluxes across the air-water interface, $F_{g,T}$, were calculated using linear regressions based on the concentration change of a given gaseous species over the 45 - minutes sampling period, the chamber volume (V_{cham}) and area (A_{cham}) as:

$$F_{g,T} = (dC_{cham}/dt_{cham})\, V_{cham} \;/\; A_{cham} \tag{2-3}$$

We accepted measurements associated with regressions with $r^2 > 0.70$ and estimated gas fluxes of CO_2 and CH_4 averaging over the replicated samples. Then, the gas transfer velocity was estimated using the first Fick's Law:

$$F_{g,T} = k_{g,T}\,(C_w - C_{eq}) \qquad (2\text{-}4)$$

where $k_{g,T}$ is the gas transfer velocity and C_w and C_{eq} are the dissolved gas concentrations in the surface water and of equilibrium with the atmosphere, respectively. Eq (2-4) was solved for k_g and then normalized to k_{600}, the gas transfer velocity for CO_2 at 20°C:

$$k_{600} = k_{g,T}\left(\frac{600}{Sc_{g,T}}\right)^{-n} \qquad (2\text{-}5)$$

where $Sc_{g,T}$ is the Schmidt number of the gas at the given temperature (Wanninkhof, 2014) and n was assumed to be 1/2 for wind speed > 3.7 m s^{-1} and 2/3 for wind speed ≤ 3.7 m s^{-1}, following the criterium given by Guérin et al. (2007a), assuming that this cut off of the wind speed determines how wavy the surface is and taking the exponents proposed by (Jähne et al., 1987).

CH_4 flux measurements that were affected by ebullition were discarded for diffusive fluxes analysis, since eq. (2-4) is only meaningful for describing diffusive fluxes (Bastviken et al., 2004b). To identify bubble-affected chamber deployments, we used the surface renewal model (Lamont & Scott, 1970) by estimating the highest theoretically possible gas transfer velocity (k_{600_max}) for the wind speed and water temperature during the chamber deployments based on eq. (2-6.1):

$$k_{600\_SRM} = A\,600^{-n}(\epsilon v)^{1/4} \qquad (2\text{-}6) \quad \left[\begin{array}{l} 1)\ \ \epsilon_{u*} = u*^3/(\kappa\, z\,);\ u* = \left(\frac{\rho_a C_d U^2}{\rho_w}\right)^{0.5} \\ 2)\ \ \epsilon_{u*\_\beta} = c_1(u*^3/(\kappa\, z\,)) + c_2\beta;\ \beta = (g\,\alpha\, H)/(c_{pw}\,\rho_w);\ \beta < 0 \end{array}\right.$$

where A is an empirical coefficient, $u*$ is the water friction velocity computed from shear stress at the air-water interface following (MacIntyre et al., 2002), κ is the von Karman constant (0.41), z is the water depth taken as 0.50 m following (Esters et al., 2017), ρ_a and ρ_w are the density of air and water, respectively. U is the wind velocity measured 2.0 m above the water surface and C_d is the drag coefficient considering atmospheric stability following (Verburg & Antenucci, 2010). We estimated that the maximum theoretical dissipation rate (ϵ_{u*}) (eq. (6.1)) and the maximum kinematic viscosity (v) were 4 × 10^{-6} m^3 s^{-2} and 9.15 × 10^{-7} m^2 s^{-1}, respectively, used the maximum proportionality coefficient reported in the literature (A = 1.46) (Esters et al., 2017) to be conservative obtaining k_{600_max} = 30 cm h^{-1} for the maximum measured wind speed. Values higher than k_{600_max} were disregarded. Most CO_2 diffusive fluxes were inconsistent with the measured surface concentrations (see below), so only CH_4 fluxes were considered for further analysis.

The other equation (2-6.2) was used for the k_{600} modelling (see section 2.2.8), where β is the buoyancy flux, c_1 and c_2 were 1.5 and -0.5, respectively (MacIntyre et al., 2010), g is the gravitational acceleration, α is the thermal expansion coefficient, H is the net surface heat flux and c_{pw} is the specific heat of water.

2.2.8. k_{600} modelling

The estimates of the gas transfer velocity obtained from measured CH_4 fluxes ($k_{600\_CH_4}$), using eqs. (2-4) and (2-5), were compared with three existing empirical models describing its wind-speed dependence, as the main driver for near-surface turbulence k_{600_C98}, k_{600_M10}, k_{600_W14} (J. Cole & Caraco, 1998a; MacIntyre et al., 2010; Wanninkhof, 2014) (Table S3). Additionally, the surface renewal model (SRM) was applied as a mechanistic approach using two different ways for estimating ϵ, as described in eq. (2-6): 1) SRM_u*, where dissipation rate (ϵ_{u*}) was calculated as a function of wind speed dependent friction velocity cubed assuming boundary-layer scaling, 2) SRM_u*_β, where dissipation rate (ϵ_{u*_β}) was calculated as a function of friction velocity and surface buoyancy flux under cooling conditions (β<0)

In eq. 2-6.2, the net heat flux entering the reservoir (H) was:

$$H = SW_{net} + LW_{net} + H_{sens} + H_{lat} \qquad (2\text{-}7)$$

where SW_{net} is the net short wave radiation flux, LW_{net} is the net long wave radiation flux, and H_{sens} and H_{lat} are the sensible and latent heat fluxes, respectively which were calculated for stable or unstable atmosphere, according to the Obukhov's stability parameter and the iterative process followed by (Verburg & Antenucci, 2010). Both H and β were limited to the periods with surface temperature recording with the thermistor. Inlets were taken as positive. Details on the calculations are in Table S4.

2.2.9. Mass balances and net methane production

Mass balances of dissolved CH_4 were estimated for the SML (Eq. (2-8)). Mass balances were evaluated for an area of 1 m^2 for local analysis around the sampling points, but also, to observe results at full-basin scale, we extrapolated the results of the mass balances to three proportional areas of the reservoir around each sampling point obtained by dividing the length of the reservoir into three equal parts. The mass rate of change of dissolved CH_4 in the control volume ($V\Delta C/\Delta t$) is dominated by vertical turbulent transport across the thermocline as the lower base of the SML (*diff_low*), evasion to the atmosphere (*evasion*), net horizontal advective transport (*advection*) and biochemical reactions (*reactions*), representing production (positive rates) or consumption (negative rates) of CH_4 in the control volume (Eq. (2-8), Table 2-2):

$$V\Delta C/\Delta t = diff\_low - evasion + advection + reactions \qquad (2\text{-}8)$$

Eq. (2-8) was solved for the *reactions* term, which could not be estimated from measurements. These results are equivalent to the net methane production (P_{net,CH_4} in µmol L^{-1} d^{-1}) considering the conversion factors, which includes gains and losses of methane by biochemical pathways.

Table 2-2. Description of the terms of the mass balances.

Term	Expression	Description
V∆C/∆t	$\frac{\Delta C}{\Delta t}V$	Rate of change of mass in the control volume (V). Estimated from observed changes of dissolved gas concentration (C) over a period (Δt) of several hours (1-8 h). It is positive for increasing concentration.
diff_low	$\frac{C_{OPL} - C_{SML}}{h} K_{Z\_Therm}\ A_s$	Diffusive exchange at the base of the SML. C_{OPL} and C_{SML} are the concentrations measured in the SML and the OPL (closest to the thermocline), h

Term	**Expression**	**Description**
		is the thickness of the thermocline, Kz is the vertical diffusivity and K_{Z_Therm} is the vertical diffusivity averaged in the thermocline. Incoming fluxes to the control volume were considered as positive and outgoing fluxes as negative. A_s is the surface area. Since turbulence measurements were not done in P1-M and P1-A in C5-M-Wet and all C6-M-Dry (see section 2.2.6), we assumed K_{Z_Therm} of those as an average of the successful measurements at the respective site.
evasion	$F_{g,T} A_s$	Atmospheric exchange. The flux, $F_{g,T}$ was calculated using eq. (2-4) with $k_{g,T}$ from eq. (2-5) based on the modeled k_{600} and surface area A_s = 1 m^2. The negative sign of the evasion term indicates the flux from water to air.
advection	$\frac{C_{SML\_i+1} - C_{SML\_i}}{\Delta x} U_{SML} V$ $U_{SML}(z) = U_w - \frac{u_*}{\kappa} \ln\left(\frac{z}{z_0}\right)$	Horizontal advective transport. $\frac{C_{SML\_i+1} - C_{SML\_i}}{\Delta x}$ is the horizontal mean gradient of the concentration between two sampling points separated by a distance Δx. Upstream and downstream concentrations were measured around one day apart. Integrated concentrations over the SML depth were used. U_{SML} is the mean flow velocity in the SML, since overflow of the river plume was not observed during the study period. It was estimated by integrating the theoretical logarithmic profile produced by the wind speed U_{10} over the SML, every 1 cm of depth. The control volume: V(m^3) = 1 m × 1 m × h_{SML} (m) where h_{SML} is the thickness of the SML. In using this approach, we assume that horizontal concentrations follow a spatial pattern that not change significantly over an interval of 1-2 days.
reactions	To be solved most of the times.	This term represents the production or consumption of dissolved CH_4 in the SML.

The *advection* was estimated using the main wind speed direction (dam-to-inflow and vice versa) as the driver of advective flow at the water surface, where the estimated mean water surface velocity was ~1 cm s^{-1}. Under these conditions, for a particle to travel the distances from P3 to P2 and from P2 to P1 (3150 m and 5880 m, respectively) it needs approximately

~3.6 and 6.8 days and is expected to take even longer because the wind direction is inverted between morning and afternoon. Therefore, spatial gradients were assumed to have no significant changes during the sampling time elapsed between sampling points (1-2 days). On the other hand, lateral transport was assumed to be negligible both because the wind speed direction does not occur in the across-lake direction and because the shores have considerable depth in the canyon-like reservoir studied and lateral transport from the shoreline by cooling of the shore water is unlikely to occur.

2.3. Results

2.3.1. Meteorological variables and surface heat fluxes

The meteorological variables during the study period reflect typical conditions of the wet tropical forests in the Colombian Andes (Table 2-3): Small seasonality in solar radiation, high surface water and air temperatures around 25 and 24°C, respectively, relative humidity higher than 50%, atmospheric pressure around 1006 hPa and high cloud cover (88% on average) being lower in the dry season Dec/2018-Feb/2019 (Figure S2). The maximum wind speed during the study period was 10.3 m s^{-1} (mean U_{10} of 13.0 m s^{-1}) and the average of the time series was 2.9 m s^{-1}, with a slight increase in the period Jun-Sep/2018 and a decrease in the period Nov-Dec/2019 (Figure S2). The net heat flux (H) showed large diurnal variations but no pronounced seasonality and its dominant component was mostly the short wave radiation (SW_{net}), but in the period of Jun-Aug/2018 a significant increase in SW_{net} was counterbalanced by a decrease in latent heat (H_{lat}) and in the period of ending Nov/2018-Jan/2019 a decrease in the net heat flux was dominated by a decrease in the long wave radiation (LW_{net}) (Figure S4).

Table 2-3. Meteorological variables during the period from 09-May-2017 to 28-Feb-2019. Minimum (min), maximum (max) and mean ± standard deviation (std).

Variable	**Units**	**min**	**max**	**mean ± std**
Surface water temperature	°C	22.4	28.7	25.0 ± 0.83
Air temperature	°C	19.6	33.0	23.7 ± 1.91
Relative humidity	%	50.5	98.3	88.6 ± 7.26
Atmospheric pressure	hPa	1001	1011	1006 ± 1.7

Cloud cover	-----	0.00	1.00	0.88	±	0.20
Wind speed (U)	m s^{-1}	0.00	10.3	2.9	±	1.1
Corrected wind speed (U_{10})	m s^{-1}	0.00	13.0	3.7	±	1.4
Water friction velocity (u*)	m s^{-1}	0.00	8.6×10^{-3}	3.7×10^{-3}	±	1.7×10^{-3}
Buoyancy flux (β)	m^2 s^{-3}	-2.94×10^{-7}	6.62×10^{-7}	5.9×10^{-8}	±	1.7×10^{-7}
Net heat flux (H)	W m^{-2}	-362	1081	94.0	±	278

2.3.2. Water column characterization

Temperature and stratification

The reservoir was weakly stratified along the entire field period, showing, in general five layers as described in section 2.2.4 (Figure 2-2 to Figure 2-6). Hereafter, the focus was put on the analysis especially on the three upper layers (Surface mixed layer, thermocline and over plume layer). Continuous thermistor records showed that surface water temperature ranged from 22 to 29°C (mean value and standard deviation: 25.0 ± 0.97). Slightly lower temperatures were observed in the rainy seasons (May/2018 and Nov/2018) and the highest temperatures were reached in the dry season (Aug/2018) (Figure S2). During the daytime samplings, it was common to find a diurnal thermocline (Figure 2-2 to Figure 2-6).

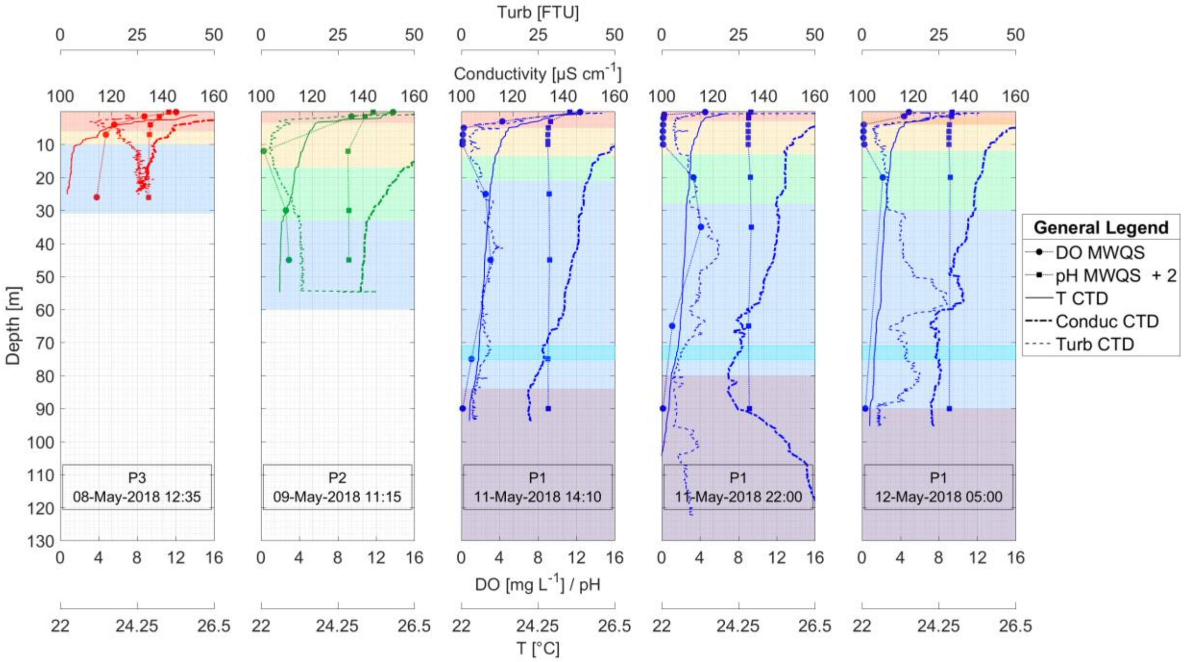

Figure 2-2. Physicochemical profiles and vertical structure of Porce III reservoir during C2-H-Wet: Dissolved oxygen (DO), pH, water temperature (T), electrical conductivity (Conduc) and turbidity (Turb) measured with the Multiparametric Water Quality Sonde EXO YSI (MWQS) or the CTD SeaBird 25 (CTD) as shown in the legend. The background color represents the layers according to the previously defined conventions (Figure S3).

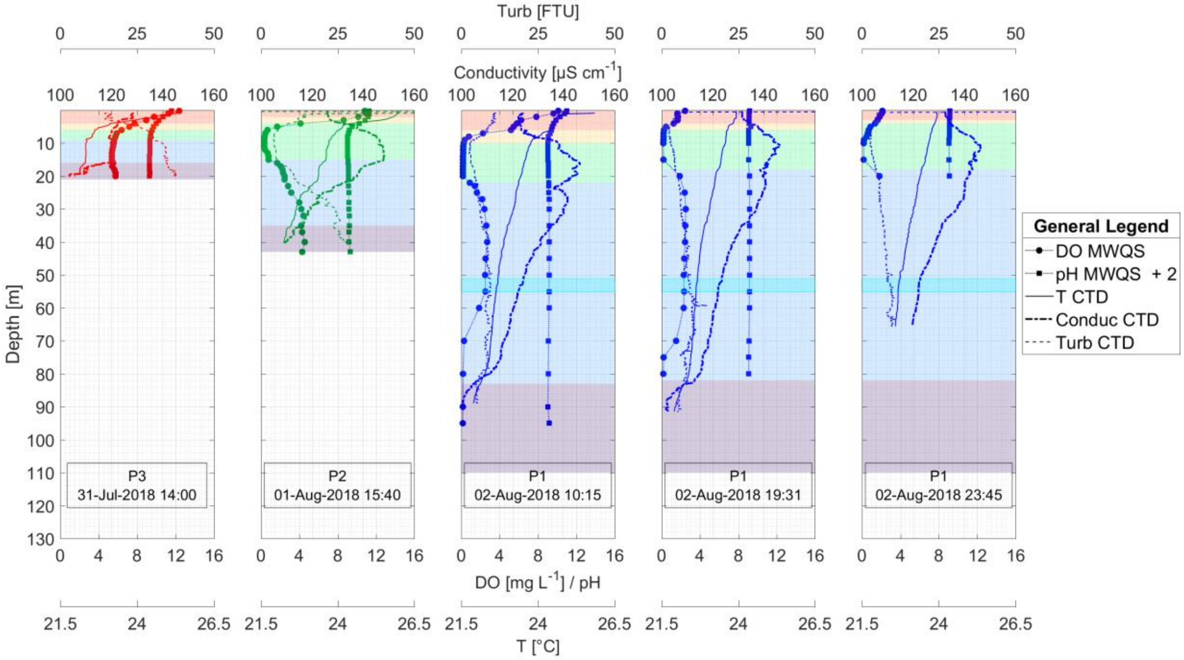

Figure 2-3. Physicochemical profiles and vertical structure of Porce III reservoir during C3-L-Dry. Abbreviations are explained in Figure 2-2 caption. The background color represents the layers according to the previously defined conventions (Figure S3).

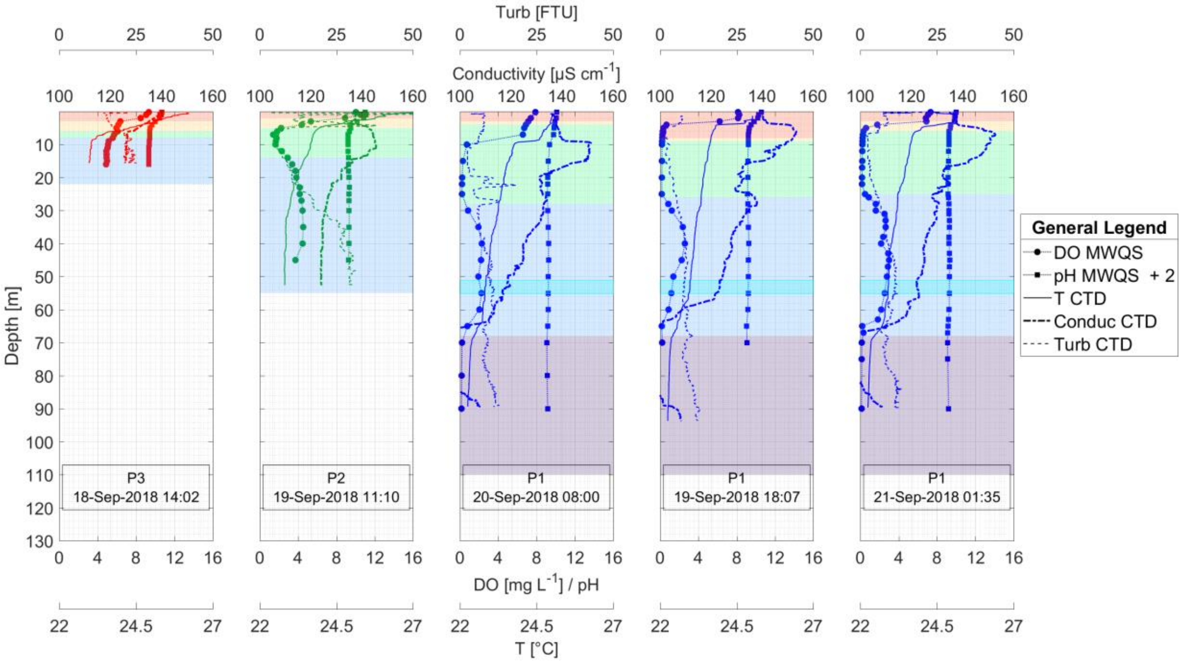

Figure 2-4. Physicochemical profiles and vertical structure of Porce III reservoir during C4-L-DWT. Abbreviations are explained in Figure 2-2 caption The background color represents the layers according to the previously defined conventions (Figure S3).

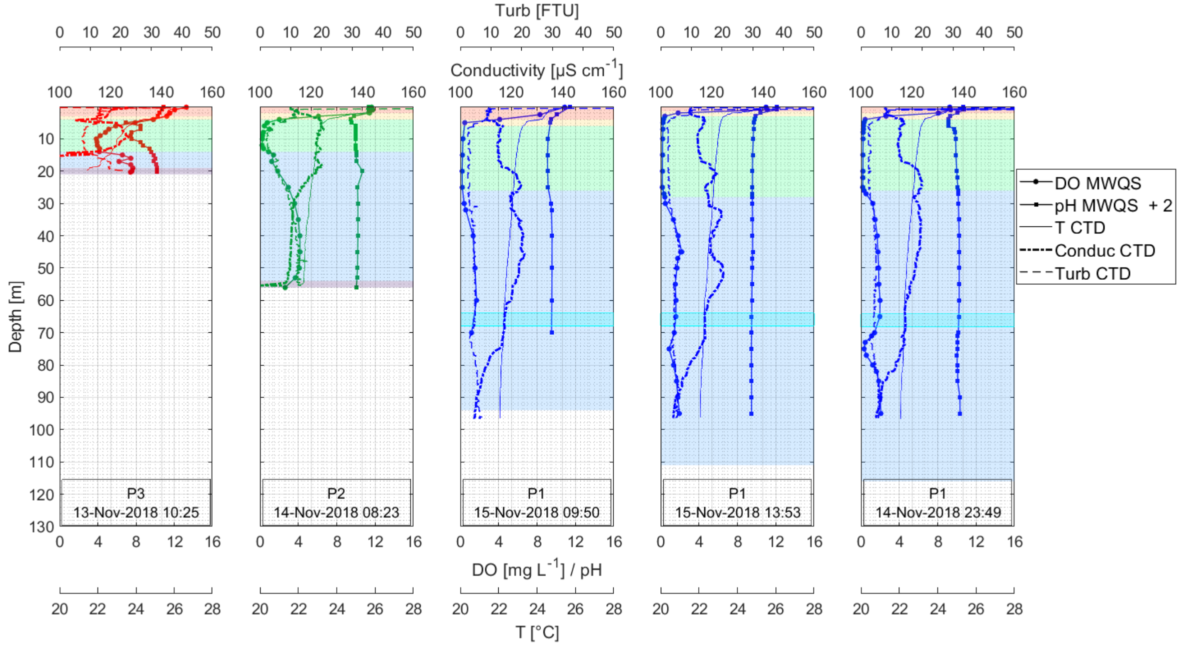

Figure 2-5. Physicochemical profiles and vertical structure of Porce III reservoir during C5-M-Wet. Abbreviations are explained in Figure 2-2 caption. The background color represents the layers according to the previously defined conventions (Figure S3).

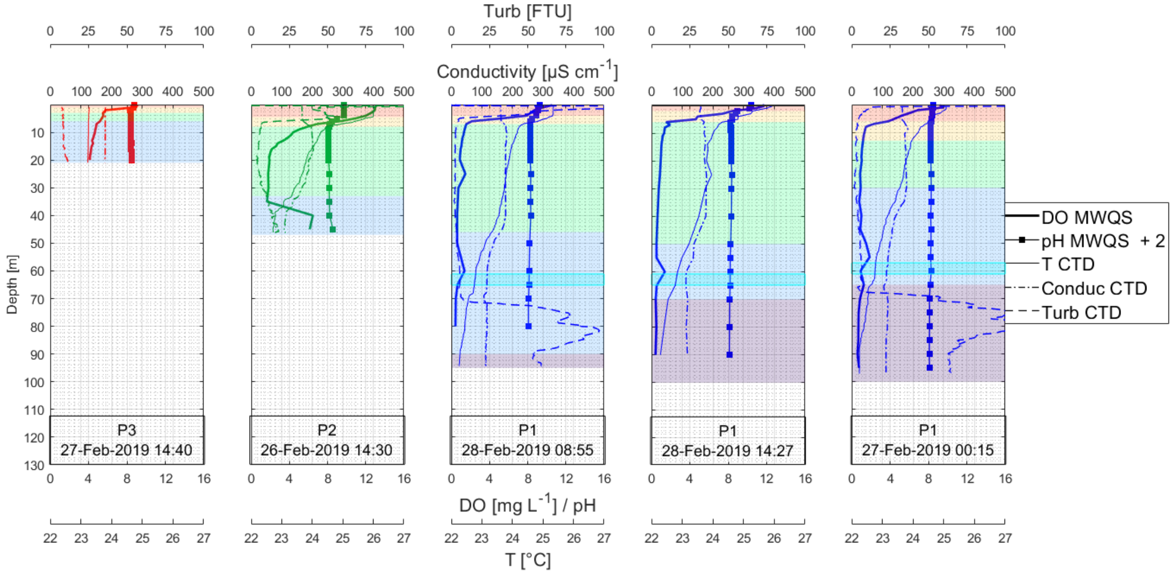

Figure 2-6. Physicochemical profiles and vertical structure of Porce III reservoir during C6-M-Dry. Abbreviations are explained in Figure 2-2 caption. The background color represents the layers according to the previously defined conventions (Figure S3).

During the field measurements (discrete samples), surface water temperature ranged from 25 to 28°C and below the thermocline, in the OPL, water temperature ranged from 22 to 24°C. SML thickness ranged from 1.5 to 8 m and was generally higher in the morning and smaller in the afternoon at P1 and also lower at P2 compared to the other two sampling stations. The thermocline was particularly thick during C2-H-Wet, when it was up to 13.5 m, but it usually ranged from 1 to 4.5 m thickness during the other campaigns (Figure 2-2 to Figure 2-6).

Dissolved oxygen, pH and Secchi disk depth

Dissolved oxygen (*DO*) profiles showed that the transition zone (P3) was always under oxic conditions showing *DO* saturation > 44% even below the thermocline. From the medium lake zone (P2) to the dam zone (P1) we observed rapid vertical decrease of *DO* reaching anoxic conditions below the thermocline (Figure 2-2 to Figure 2-6).

At the surface, *DO* supersaturation was constant during all field campaigns and at all three sampling points during daytimes (114 - 172%), indicating a continuous positive net production of the ecosystem promoted by eutrophic condition (Figure 2-7). This idea is also supported by the alkaline *pH* found from C2-H-Wet to C5-M-Wet in the diurnal samples (8.1 to 9.7) and by the strong differences between day and night observed in both *DO* and *pH*. Especially during C2-H-Wet and C3-L-Dry, diel changes with amplitudes of about 100% in *DO* saturation and 2 *pH* units were observed (Figure 2-7), suggesting that photosynthetic activity highly influences the dynamics of both variables. Slightly lower values of *DO* and *pH* were observed during C4-L-DWT in daytime samples respect to the other campaigns and also were observed lower day-night difference as well as during C5-M-Wet, with changes of 10% and 23% in *DO* saturation and 0.6 and 1.4 *pH* units from daylight to darkness, respectively, indicating probably weaker photosynthetic activity in the period Sept-Nov/2018 respect to May-Aug/2018. During C6-M-Dry (Feb/2019) relative low surface *pH* was closer to neutral conditions in daytime samples (6.8 to 8.4), but *DO* supersaturation was still present and lower values of both variables were found in nighttime samples, showing that eutrophic condition was maintained (Figure 2-2 to Figure 2-6). In the campaigns in which afternoon samples (P1-A) were taken during daylight (from C4-L-DWT to C6-M-Dry), we observed that *DO* and *pH* considerably increased from the morning to the afternoon.

DO and *pH* generally decreased in the dam zone (P1) with respect to the upstream sections of the reservoir (P3 and P2) from C2-H-Wet to C4-L-DWT. During C6-M-Dry *DO* and *pH* did not show strong spatial variability without any clear spatial pattern, except that the medium lake zone (P2) showed higher *pH* and *DO* than the other two points as well as it does during C2-H-Wet and C4-L-DWT. Also, Secchi disk depth *(SD*) often shows lower values in P2 (Figure 2-7). During C6-M-Dry, strong spatial variations of *SD* were observed, with a very low *SD* at P2 (0.67 m) and a relative clear surface water at P1 (2.8 m) after an intense rainfall event (Figure S16).

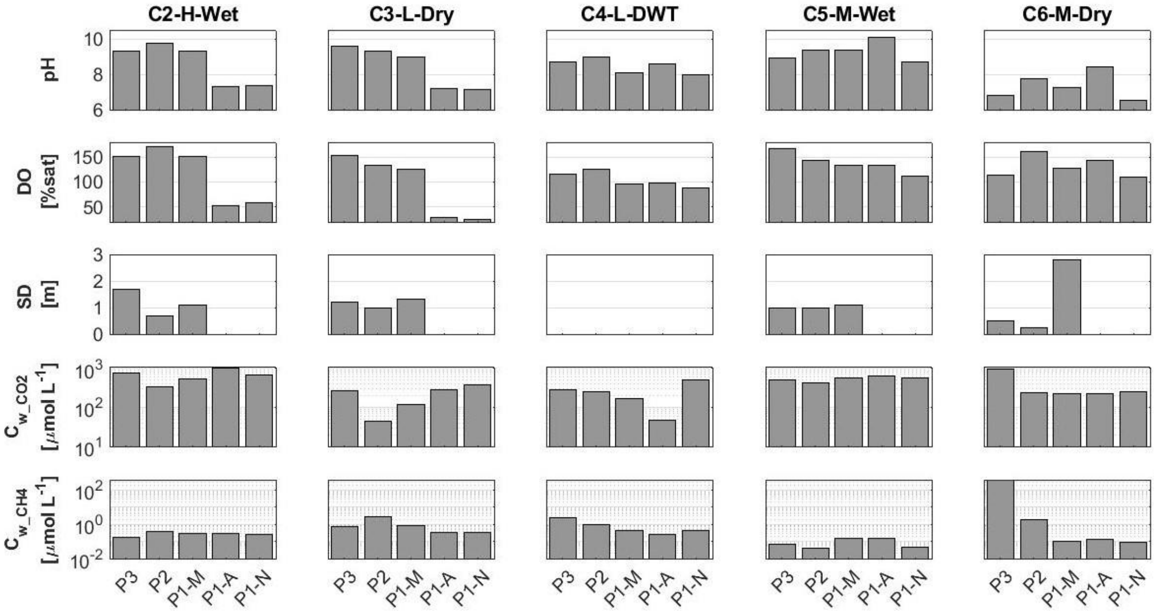

Figure 2-7. Properties of surface water at the three sampling stations (P3, P2, P1), including diurnal variation (P1-M, P1-A, P1-N). Bars indicate the results of the measurements during the chamber deployments. At the top are the field campaigns corresponding to each column. The bottom panel shows the bar labels for the entire figure. The scale of the vertical axis of the concentrations is logarithmic. *SD* was not taken during C4-L-DWT. P1-A in C2-H-Wet and C3-L-Dry corresponds to darkness. C_{w_CO2} was overestimated by the headspace method and discarded from the analysis.

Dissolved CO_2 and CH_4

Very high CO_2 surface water concentrations were estimated in Porce III (379 ± 226 µmol L^{-1}), always exceeding the equilibrium concentrations, in contrast to several negative fluxes (from the air to the water) measured by floating chambers (detailed below). Regarding this, we concluded that the high *pH* of the water surface in the reservoir caused an overestimation of the CO_2 concentration by the headspace procedure (see discussion), and we did not consider CO_2 concentrations in the following analysis.

CH_4 concentrations usually increased in the deeper layers, sometimes there were peaks between the thermocline and the OPL and decreased in the inflow plume where *DO* concentrations were slightly higher (Figures S10 to S15). When the bottom anoxic layer occurred, there were always very high CH_4 peaks at >80 m depth (~ 5×10^1 - 5×10^2 µmol L^{-1}). In the OPL, CH_4 concentrations were from ~ 1 to 5 µmol L^{-1} and smaller concentrations of ~ 5×10^{-2} to 8×10^{-1} were found in the rainy periods C2-H-Wet and C5-M-Wet as well as the dry period C6-M-Dry. Usually, CH_4 concentrations in the SML were close to ~ 3 × 10^{-1} µmol L^{-1}, often, but not always lower than those in the OPL. During the C5-M-Wet rainy season concentrations were lower by up to ~1 order of magnitude and also no bottom CH_4 peaks were observed as the oxygenated river plume traveled along the bottom throughout the entire reservoir (Figures S5 and S10), suggesting that during this period there was little CH_4 transported vertically from the bottom. Three extremely high values between ~ 6 × 10^1 (at P1-M) and ~ 4 × 10^2 µmol L^{-1} (at P3) where found at the SML, two of them during C6-M-Dry (Figure 2-7) under low wind speed (<1.8 m s^{-1}) according to the records of the meteorological station (and zero according to the field notes) (Figures S16 to S21), suggesting possible accumulation of dissolved CH_4 in the SML. After the high values in C6-M-Dry at P1-M and P1-A showed typical concentrations as the other campaigns, just after a very intense rain event (Figure S16). Even excluding those exceptional values, CH_4 concentrations in the SML was on average 2.4 times higher during low water levels compared to high and medium water levels (Table 2-4).

Table 2-4. Seasonal averages (mean ± std) of the variables related to the atmospheric fluxes of CH_4: field gas transfer velocity (k_{600_CH4}), surface water concentrations (C_{w_CH4}), measured diffusive atmospheric flux (F_{CH_4}). Also, quotients between groups of data (according to water level conditions) are presented. *Values given for low and medium levels reflect mostly the results of P1, because several flux measurements at P2 and P3 were rejected during quality assessment mostly due to bubbles (Table S6).

Water level	Campaign	C_{w_CH4} (µmol L^{-1})	F_{CH_4} (mmol m^{-2} d^{-1})*	F_{CO_2} (mmol m^{-2} d^{-1})*
High	C1-H-Wet and C2-H-Wet	0.46 ± 0.06	0.46 ± 0.65	14.3 ± 59
Low	C3-L-Dry and C4-L-DWT	1.09 ± 0.92	1.68 ± 0.82	34.7 ± 97
Medium	C5-M-Wet and C6-M-Dry	0.40 ± 0.88	0.73 ± 0.16	-17.3 ± 20
Low / High		2.4	3.7	2.43
Low / Medium		2.7	2.3	-2.0

Turbulent dissipation rates and diffusivity in the SML

In the SML, mean dissipation rates of turbulent kinetic energy (ϵ_m) ranged from ~10^{-9} to ~10^{-6} m^2 s^{-3} and the turbulent diffusivity (K_z) ranged between ~10^{-5} and ~10^{-4} m^2 s^{-1} (Table 2-5, Table S4). The maximum measured ϵ_m of ~10^{-6} m^2 s^{-3} occurred during C4-L-DWT in the presence of strong wind (U_{10} > 6 m s^{-1}) (Table 2-5), showing the high sensitivity of this variable to the dynamical atmospheric conditions, which makes difficult to observe seasonal patterns from episodic measurements.

The vertical structure of the ϵ_m in the SML showed logarithmic profiles decreasing with depth at the lake zone (P2) and dam zone (P1), where both K_z and ϵ_m were higher in the SML compared to the lower layers, whereas at the transition zone (P3) it was higher in the bottom-attached plume, except during C4-L-DWT when K_z and ϵ_m were higher in the SML due to the strong wind (Table S5, Figs S17 to S20). This suggests a relatively higher potential for transport of dissolved gases from the bottom at location P3, and a relatively higher potential for gas evasion at P2 and P1. Sometimes high turbulence and K_z reached the thermocline after persistent strong winds (C3-P1-A, C4-P1-A). Between the thermocline and 30 m depth, K_z and ϵ_m decreased in magnitude from P3 to P1 (Figs S17 to S20), showing the influence of upwelling of the plume over the calm thin upper layers in the transition zone (P3).

Table 2-5. Summary of the measured turbulent dissipation rates (ϵ_m in m^2 s^{-3}) and the estimated turbulent diffusivities (K_z in m^2 s^{-1}) in the SML.

	C2-H-Wet		C3-L-Dry		C4-L-DWT		C5-M-Wet	
Station	ϵ_m	K_z	ϵ_m	K_z	ϵ_m	K_z	ϵ_m	K_z
P3	6.50×10^{-8}	4.50×10^{-5}	1.90×10^{-8}	1.30×10^{-5}	3.30×10^{-6}	3.50×10^{-4}	1.30×10^{-7}	4.90×10^{-5}
P2	2.30×10^{-7}	1.20×10^{-4}	7.30×10^{-7}	9.60×10^{-5}	4.20×10^{-8}	8.10×10^{-5}	2.3×10^{-8}*	1.1×10^{-4}*
P1 - M	1.00×10^{-8}	4.10×10^{-5}	5.20×10^{-9}	1.30×10^{-5}	1.10×10^{-9}	2.90×10^{-6}	ND	ND
P1 - A	2.20×10^{-7}	1.40×10^{-4}	4.10×10^{-8}	1.10×10^{-4}	9.70×10^{-8}	1.50×10^{-4}	ND	ND
P1 - N	1.40×10^{-8}	1.30×10^{-5}	2.40×10^{-8}	8.40×10^{-5}	4.00×10^{-8}	1.50×10^{-4}	1.20×10^{-7}	1.30×10^{-4}

*Assumed as the thermocline, at 2 m depth.

In all campaigns where we observed diurnal variation (C2-H-Wet, C3-L-Dry and C4-L-DWT), an increase of ~ 1 - 2 orders of magnitude of surface ϵ_m was observed between morning and the afternoon, when the wind speed increased, followed by a slower decrease between the afternoon and the night. All minimum values per campaign of ϵ_m in the SML were observed at P1-M. The diurnal variability of K_z was not as large in magnitude, but slightly higher values were observed in the afternoon measurements (Table 2-5).

2.3.3. Measured gas fluxes and k_{600}

Estimates of CH_4 diffusive fluxes (F_{CH_4}) were always positive and ranged from 0.046 to 2.3 mmol m^{-2} d^{-1} showing that the reservoir was a continuous source of CH_4 throughout the study period (Table S6). The seasonal sampling revealed that F_{CH_4} was 3.7 times higher during low water level than during high level periods, when also $k_{600\_CH_4}$ and $C_{w\_CH_4}$ were higher (Table 2-4). No spatial patterns of the diffusive fluxes could be observed because most of the fluxes measured at P3 and P2 were rejected (Table S6), suggesting consistent interference of bubbles during the floating chamber measurements in the southern part of the reservoir. Gas transfer velocities ($k_{600\_CH_4}$) estimated from CH_4 fluxes in floating chambers ranged from 0.01 to 27.7 cm h^{-1} (Table S6) for wind speed (U_{10}) between 0.5 and 7.8 m s^{-1}.

The CO_2 diffusive fluxes measured by floating chambers were highly variable (-53.0 – 320.6 mmol m^{-2} d^{-1}) and recurrently negative in the diurnal samples (Table S6), indicating that sometimes, the reservoir was a sink of CO_2 (-25.1 mmol m^{-2} d^{-1} on average, only negative results) what is expected in water surfaces with high photosynthetic activity and agrees with the physico-chemical indicators of eutrophic conditions. This behavior was more frequent in the southern part of the reservoir where the proportion of negative respect to the total accepted fluxes was 77% and 100% in P2 and P3, respectively, versus 45% in P1 (only daylight samples). CO_2 flux was influenced by the time of sampling and during the late afternoon, evening and early morning hours the flux tends to be positive, while during the morning, midday and early afternoon hours the flux is lower and tends to be negative, suggesting a possible diurnal cycle of the variable (Figure 2-8).

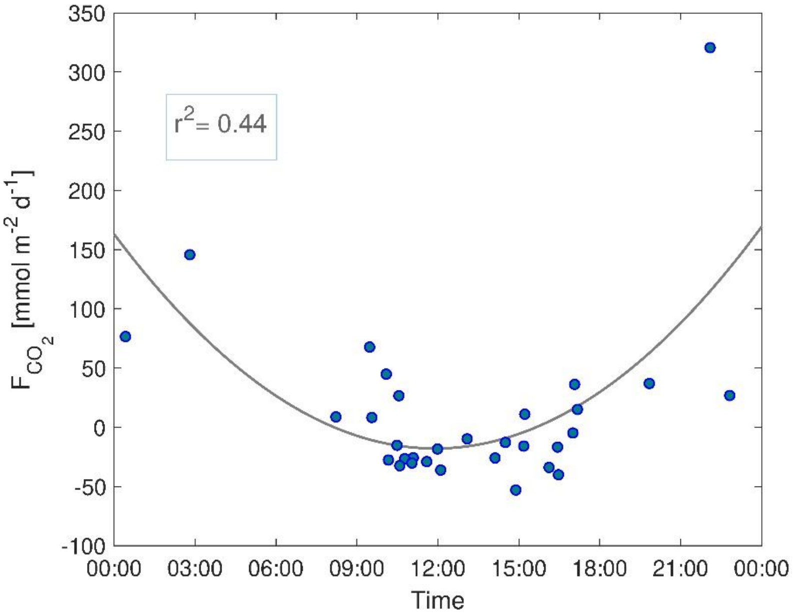

Figure 2-8. CO_2 flux vs. time. The blue points are the CO_2 flux measured with floating chambers and the text box shows the determination coefficient of the fitting polynomial curve (solid grey line)

Similar to CH_4 behavior, seasonal sampling showed that F_{CO_2} was higher during the low water level and dry periods being 2 times and 19 times higher than high level and wet periods, respectively. However, the average of the dry periods (22.6 ± 108 µmmol L^{-1}) was exacerbated by the very high flux measured at C3-LW-Dry at 22:05 (321 mmol m^{-2} d^{-1}) and excluding this value, the average of the dry periods reverts to -10.6 ± 28 µmmol L^{-1}, showing the large variability of the CO_2 flux in dry seasons and the high sensitivity of the average to possible peaks during discrete measurements such as floating chambers. Dry-wet transition was very similar to dry periods average.

In conflict with the recurrent measured negative fluxes, all dissolved CO_2 concentration measurements showed supersaturated concentrations relative to atmospheric equilibrium, always suggesting CO_2 evasion. This inconsistency may be associated with the overall high *pH* (> 7.5) found at the reservoir water surface which, according to recent revelations, leads to alter the initial gas content in the vessel during the equilibrium process in the headspace (Koschorreck et al., 2021) (see discussion). Because of these contradictory results, only the flux measurements of CH_4 were considered for the gas transfer velocity calculations and the further analysis.

2.3.4. Modelling k_{600}

Measured gas exchange velocities ($k_{600\_CH_4}$) were generally higher than predicted by wind-based former models, where the slopes of linear regressions between the measured and the wind-based predicted ones were 2.5 for J. Cole & Caraco (1998b) and 1.3 for both (MacIntyre et al., 2010) and Wanninkhof (2014) with acceptable correlations r^2 ~ 0.60 for all models tested, using all data (diurnal and nocturnal) (Figure 2-9). These results probed the robustness of chamber-based estimations of CH_4 emissions and k_{600} and even stronger correlations, close to 0.70, were found when only diurnal data were collected (Figure S21). We decided to continue working with all data so that our own model can be used at any time.

The two approaches for estimating k_{600} through the surface renewal model (equation (2-6)) yielded similar results with coefficient A ~ 0.7- 0.8 and r^2 ~ 0.6 for linear fits (Figure 2-9), which indicates that both options are valid for estimating dissipation rates.

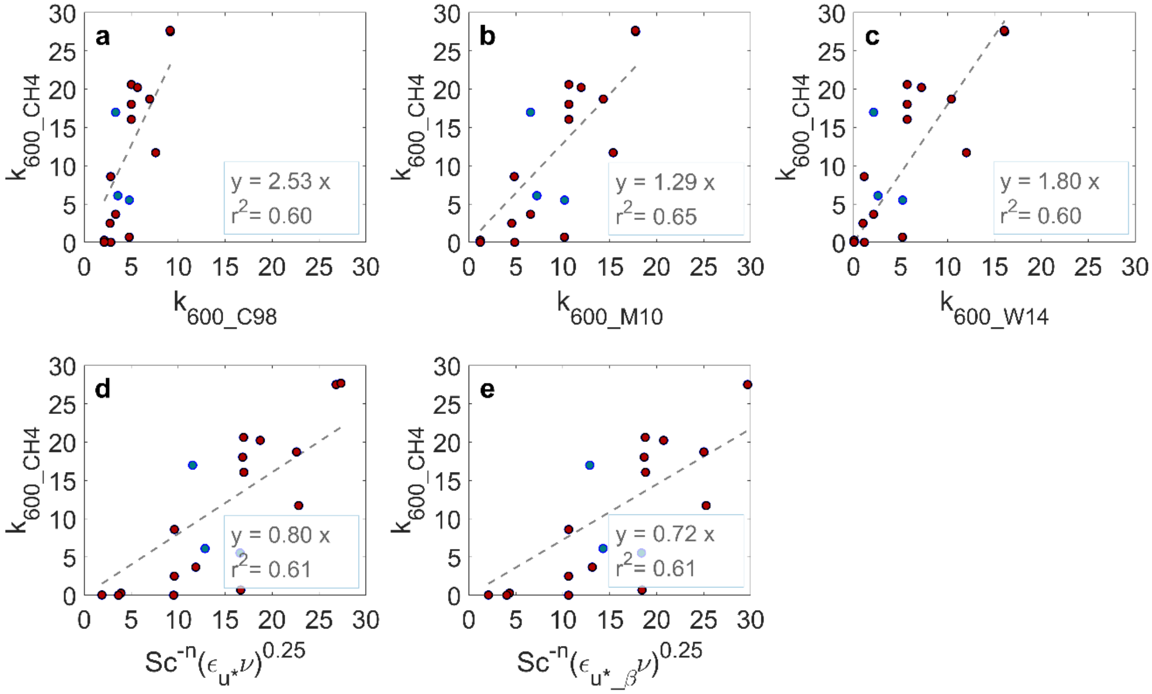

Figure 2-9. Gas exchange velocities estimated from CH_4 fluxes ($k_{600\_CH_4}$) vs. predicted k_{600}. The panels show different approaches used to for predicted k_{600}: **a**. Derived from wind speed (Cole & Caraco (1998)), **b**. from wind speed and buoyancy flux when cooling (MacIntyre (2010)), **c**. wind speed following (Wanninkhof (2014) **d**. SRM_u*, **e**. SRM_u*_β and

Due to the underestimated k_{600} obtained from the wind-based models, we adopted a model based on the SRM in which the coefficients were fitted to the field data. We consider the SRM _u* to be the simplest model (equation 2-6.1) and to have least uncertainty, since it only depends on the wind speed that was continuously measured in the field, whereas the other SRM (SRM_β_u*) ~~estimates~~ (equation 2-6.2) does involve no-directly-measured variables (such us cloud cover). Therefore, we propose the following model for the gas transfer velocity at Porce III reservoir:

$$k_{600\_model} = 0.8 \times 600^{-0.5} \left(\epsilon_{u^*} \nu\right)^{0.25} \qquad (2\text{-}9)$$

k_{600_model} ranged from 1.5 to 21.9 cm h^{-1} (mean 11.8 ± 4.8) (Table S6) and was strongly correlated with $k_{600\_CH_4}$ ($r^2 = 0.73$) as well as when only data of day hours were tested ($r^2 = 0.66$) (Figure 2-10).

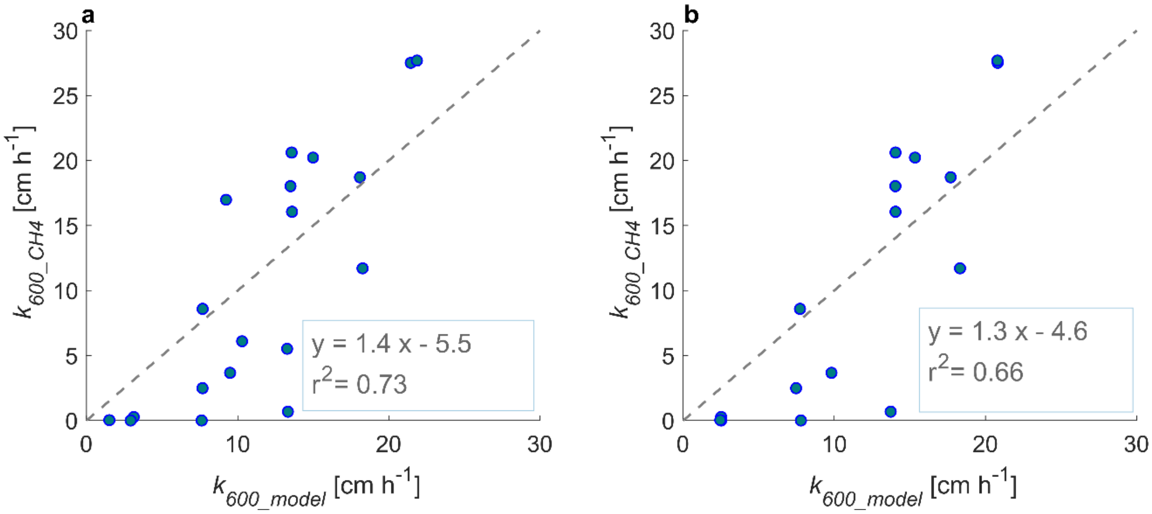

Figure 2-10. Gas exchange velocities estimated from CH_4 fluxes ($k_{600\_CH_4}$) vs. modeled k_{600}. **a**. all accepted data and **b**. only daytime data

2.3.5. CH_4 Mass balances

Except for the obvious difference in the magnitude of the terms, the local and full-basin mass balances gave similar results. The main difference in approach was related to the *advection* term, which was mostly negligible in the discrete mass balances and completely negligible when the balances were performed for the full basin (Figure S22). Here, we detail the results obtained from the local mass balances.

The mass balances indicate that changes of surface water CH_4 concentration over time were mainly explained by *evasion* and *reactions* (Figure 2-11). During the wet seasons (C2-H-Wet and C5-M-Wet) those terms were larger in the transition and medium lake zones of the reservoir (P3 and P2) ($\sim 10^{-6}$ - 10^{-7} g s^{-1}) than the dam zone (P1) ($\sim 10^{-7}$ - 10^{-8} g s^{-1}) and during the dry and low water level seasons (C3-L-Dry, C4-L-DWT and C6-M-Dry) were additionally significant at daylight hours near the dam. In C6-M-Dry the values were exceptionally high (up to $\sim 10^{-4}$ g s^{-1}) due to a possible accumulation of CH_4 after long low-wind periods (or no wind according to the field notes) at P3 and P1-M (Figure S16) and a large net methane production in this campaign causing significantly higher CH_4 surface concentrations in comparison to the other campaigns (by 3 orders of magnitude). In contrast and regardless of the season, CH_4 mass balance terms were always smaller at night (P1-N) ($\sim 10^{-7}$ - 10^{-8} g s^{-1}) in all campaigns. Spatial and diel patterns agree with those found for the trophic state indicators (*pH* and dissolved oxygen), suggesting that the CH_4 hour-scale variations, *evasion* and *reactions* favors by processes occurring during daylight hours and are stronger where eutrophic condition is stronger.

When strong turbulence and diffusivity were found in the thermocline along with large differences in CH_4 concentrations in the SML versus the OPL, the exchange of dissolved CH_4 with the lower layers (*diff_low*) became important (at P3 during C2-H-Wet and C5-M-Wet, P1-A during C3-L-Dry and P1-M during C4-L-DWT), especially transporting CH_4 from the OPL to the SML due to recurrent peaks in CH_4 concentrations in the OPL.

Particularly, the results obtained for the *evasion* term indicate that the southern part of the reservoir is the most important source of diffusive CH_4 to the atmosphere which may be related to higher CH_4 concentrations at water surface and also the increasing turbulent dissipation rates towards the river inflow.

Reactions were always among the dominant terms of the balances and showed an alternation of net production and consumption. Near the dam, the recurrent negative sign of the reactions term suggests the dominance of CH_4 consumption (oxidation) versus production in the morning and night (P1-M and P1-N) and the opposite in the afternoon, whereas in the transition and medium lake zones of the reservoir, the dominance of the consumption/production processes did not show seasonal patterns. However, it is difficult to define whether consumption or production generally dominated the SML mass balances, because the balances were performed from discrete measurements. For example, during C6-M-Dry the concentration increased dramatically (3 orders of magnitude) from P1-N to P1-M in 30 hours between one sample and the other (Figure S16), showing a high methane accumulation at the surface, which according to the methane profiles is not coming from below (Figure S10), suggesting that is produced in the SML. However, the balance was performed between 9 a.m. and 12 p.m (~ 3 hours), where there was a slight relative decrease between both samples of the SML already loaded with high CH_4 concentrations, resulting in a very high methane consumption when solving the balance (Figure 2-11e). An additional case is C6-M-Dry at P2, where high differences in concentrations between P2 and P1 produced high advection estimates and high reactions when solving the balance.

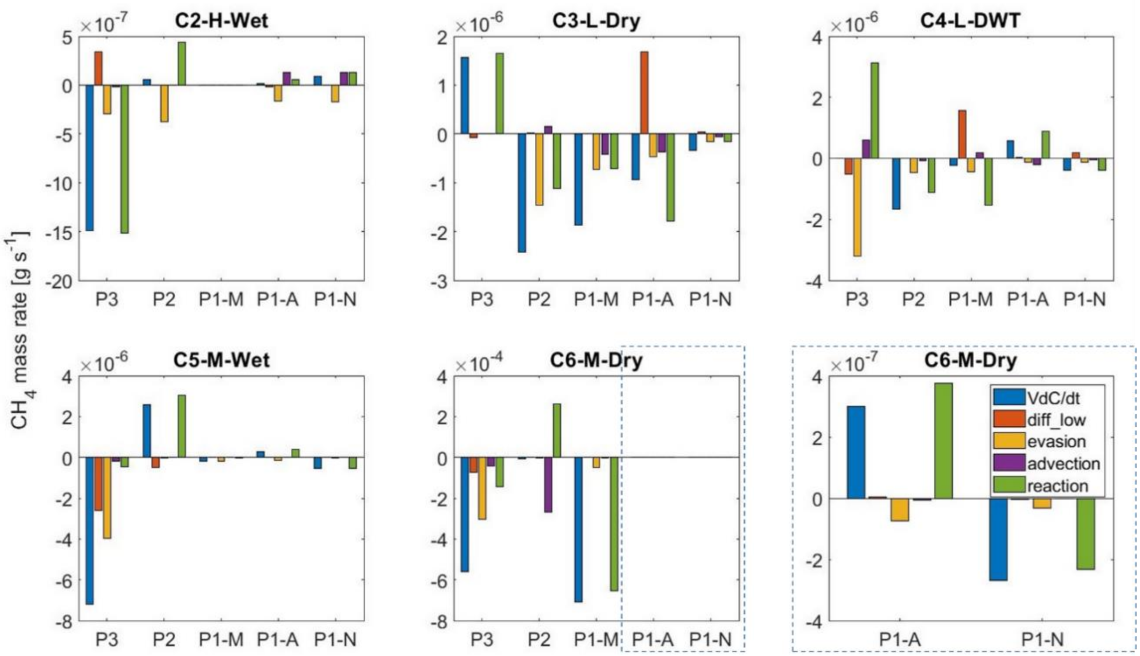

Figure 2-11. Terms of the CH_4 mass balances (in g s^{-1}) in the surface mixed layer at different sampling locations and times (P1-P3) and for the different campaigns: panel titles refer the field campaigns. Scales of the subplots are different in order to observe all terms. The sign of the flux denotes whether the flux is incoming (positive) or outgoing (negative) with respect to the SML.

Net Methane Production ($P_{net,CH4}$) ranged between -3.0 µmol L^{-1} d^{-1} and 8.3 µmol L^{-1} d^{-1} for all campaigns, except for C6-M-Dry when it showed exceptional values between -883 and 316 µmol L^{-1} d^{-1} at P3, P2 and P1-M (Figure 2-12), associated with exceptionally high surface CH_4 concentrations measured in this campaign and are discussed below. These discrete results reflect the changes within few hours, showing very high consumptions in P1-M. However, the increase in CH_4 concentrations from the other campaigns to C6-M-Dry lead us to believe that exceptional positive $P_{net,CH4}$ were happening during the last period. Since low wind speed occurred between the time of P1-N and P1-M, we assume that the only important terms of the balance are the change over time and the reactions, that yield that a $P_{net,CH4}$ of 49 µmol L^{-1} d^{-1} would be required to accumulate 62 µmol L^{-1} in the SML at P1 in the 30 hours.

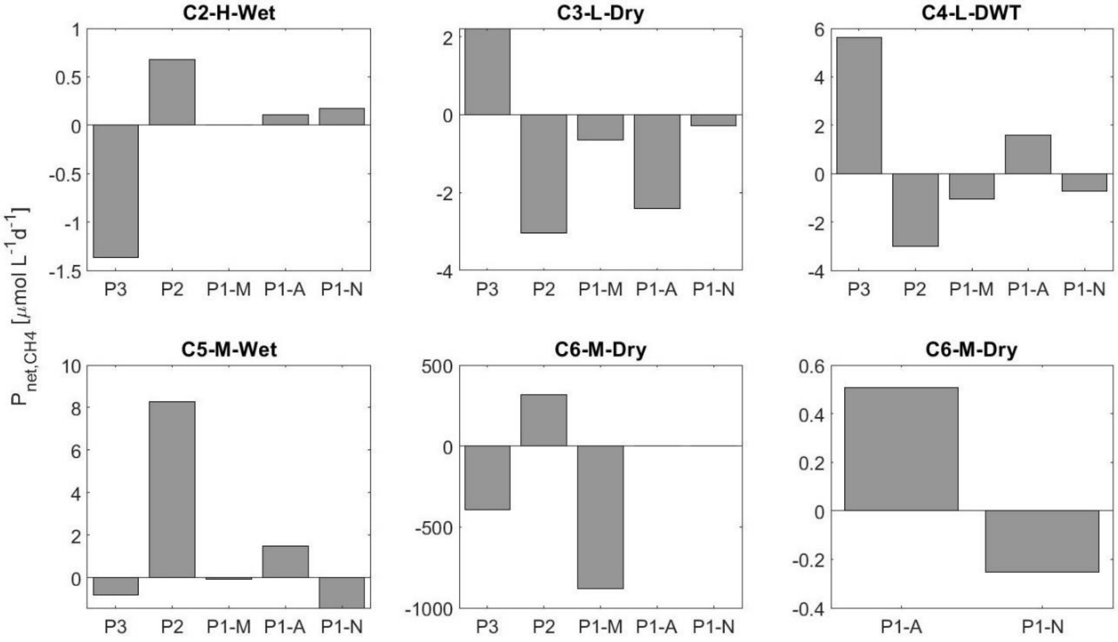

Figure 2-12. Net methane production ($P_{net,CH4}$). panel titles refer the field campaigns. Positive values correspond to net CH_4 production and negative values, to CH_4 consumption.

2.4. Discussion

2.4.1. Trophic state, CO_2 fluxes and CO_2 concentrations

In addition to the evident high phytoplankton abundance observed (not measured) during the field campaigns, the recurrently observed diurnal negative CO_2 fluxes (F_{CO_2}), the supersaturation of dissolved oxygen (*DO*) as well as its high variability between daytime and darkness, the hypoxic and anoxic conditions in the hypoliminion (<10% of saturation), and the consistent low Secchi disk depth (*SD* < 2 m) at most of the sampling stations, indicate eutrophic conditions in the reservoir during the study period (Chapra, 1997). This is further supported by data from the reservoir operator on the trophic state index (*TSI*) (Toledo et al., 1983), showing a constant eutrophic condition of Porce III surface between 2016 and 2018 (*TSI* >54) (Figure S23 and Figure S24). Eutrophic conditions are mostly caused by nutrient enrichment (Camargo & Alonso, 2007; Jorgensen et al., 2005), what is consistent with the high nutrients loads expected from the polluted inflowing Porce river. Eutrophic characteristics were more pronounced during May – August of 2018, weaker during September – November of 2018 and were strongly spatially variable in February of 2019. *SD* was consistent to show the medium lake zone (P2) as the one with the lowest transparency and *TSI* (company's information) was generally higher in the southern section of the reservoir and in the transition zone where also the negative CO2 fluxes were more frequent (Table S6). Similarly, (Pacheco et al., 2015) found the highest concentration of chlorophyll-a around the transition zone in Funil reservoir (Brazil), found the highest concentration of chlorophyll-a around the inflow region in Funil reservoir (Brazil), probably related to the effect of wind pattern.

In contrast to the negative CO_2 fluxes, the CO_2 concentration in the surface water was consistently higher than the atmospheric equilibrium concentration (~13.0 µmol L^{-1}). We therefore concluded that CO_2 surface concentration measurements are not reliable. It is widely known that dissolved CO_2 is involved in a dynamic chemical equilibrium with other carbonate species (Stumm & Morgan, 1996), which makes the headspace method potentially flawed (Koschorreck et al., 2021) and this effect has been typically assumed to be small (Hope et al., 1995). However, recent research has proved that the headspace method, used in the gas chromatography procedure, can largely overestimate CO_2 concentrations for under-saturated samples or *pH* above 7.5, which represent typical conditions in eutrophic systems (Koschorreck et al., 2021). It is possible to correct CO_2 concentration results from pH and alkalinity, with better approximations in waters with neutral to basic pH and high alkalinities (>1000 µmol/L), otherwise, overestimates (between

50 and 300%) could be incurred (Abril et al., 2015). For this reason, in future studies, water conditions should be considered before deciding to apply the headspace technique or to use direct in situ pCO_2 measurement methods. In this study, alkalinity was not measured, so the correction could not be applied.

2.4.2. CH_4 dynamics in the surface mixed layer

The diffusive fluxes of CH_4 (F_{CH_4}) (0.046 - 2.3 mmol m^{-2} d^{-1}) were in the range of fluxes reported for other tropical reservoirs (Deshmukh et al., 2016; Guérin & Abril, 2007; Paranaíba et al., 2018a). We found that during low water level, the CH_4 fluxes were up to 3.7 times higher compared to high water level seasons (Table 2-4). Other studies have also found higher emissions during dry seasons in tropical reservoirs, normally associated to low water levels when the system depends on the basin hydrology (Guérin & Abril, 2007).

Excluding the extreme values (orders of magnitude > 10^1 µmol L^{-1}), the measured CH_4 surface concentrations ($C_{w\_CH_4}$) are comparable with values previously reported for the epilimnion in other tropical reservoirs (Guérin & Abril, 2007; Paranaíba et al., 2018a; Rodriguez & Casper, 2018; Santoso et al., 2020), but the upper limit (3 µmol L^{-1}) can be considered to be at the high end for stratified waters, even if compared to values reported for tropical reservoirs with high organic load such as Furnas Reservoir in Brazil (Paranaíba et al., 2018a). However, values of similar magnitude, even as high as our extreme values, have been reported in other systems close to the epilimnion and have been attributed to oxic methane production (OMP) (Tang et al., 2016).

The lowest $C_{w\_CH_4}$ in the SML were found during the wet season of C5-M-Wet in which the river traveled the entire length of the reservoir along the bottom and no bottom anoxic layer occurred and, consequently, there were no extreme peaks of CH_4 at high depths (> 4 x 10^1 µmol L^{-1}) as in the other campaigns (see profiles in Figures S10 to S15). This behavior may be associated with CH_4 oxidation (Guérin & Abril, 2007; Rudd et al., 1976) during the vertical transport of the gas from the sediment to the surface in the fully oxic water column in the C5-M-Wet campaign as opposed to the other campaigns, in which a thick anoxic layer at the bottom might give less chance for CH_4 oxidation.

Dissolved methane surface concentrations ($C_{w\_CH_4}$) was rather constant along the reservoir during the high-level campaigns but showed a consistent longitudinal decline from the transition and medium lake zones towards the dam zone during the low-level campaigns. Then, we found interesting aspects of the seasonal and spatial dynamics of methane in the reservoir. Regarding seasonal variability in Porce III, we observed that the higher CH_4 concentrations are related to the hydrological condition prevailing during low water levels, which is an scarcely explored aspect of CH_4 dynamics in tropical reservoirs, where seasonal dynamics have been poorly studied and previous research has focused on the climatic regime rather than the reservoir water level, for example in (Guérin & Abril, 2007) where higher CH_4 concentrations were found in the epilimnion during dry seasons than during wet seasons. Regarding spatial variability, we observed that the higher CH_4 concentrations at the transition and medium lake zones of the reservoir coincided with the stronger eutrophic condition (higher dissolved oxygen and *pH* and lower Secchi depth) at these regions in comparison to the dam zone.

There is a traditional association of CH_4 production to anaerobic processes. However, besides the spatial pattern of higher methane towards the stronger oxic zone, the mass balances revealed frequent occurrence of CH_4 production in the SML (positive reaction rates). Several studies have shown that trophic state is positively related to CH_4 emissions and/or concentrations in reservoirs (Deemer et al., 2016; Delsontro et al., 2018; Paranaíba et al., 2018a), this is traditionally related to low oxygen concentration and high contents of autochthonous carbon in the hypolimnion, both promoting elevated CH_4 production (West et al., 2012). Beyond, recent research has revealed possible CH_4 production in the oxic euphotic zone of lakes and reservoirs (Soued & Prairie, 2021), recurrently showing peaks in the epilimnion or near the surface (Bogard et al., 2014; Donis et al., 2017; Günthel et al., 2019; Tang et al., 2014). Oxic methane production (OMP) has been associated with the autotrophic activity since it has been positively correlated to photosynthesis, O_2 concentrations and dissolved organic carbon (Blees et al., 2015; Donis et al., 2017; Grossart et al., 2011), suggesting a link between the OMP and algal derived substrates available for methanogens (Bogard et al., 2014; Donis et al., 2017; Tang et al., 2014) and even, the direct CH_4 production by cyanobacteria as suggested by (Bižić et al., 2020). Other explanations point to a non-microbial CH_4 production coming from the effect of radiation over organic compounds transforming them into CH_4 (Ma & Green, 2004; Obernosterer & Benner, 2004). Previous reported values show that rates of OMP in laboratory incubations and natural oligo-mesotrophic lakes (50 to ~200 nmol L^{-1} d^{-1}) (Bogard et al., 2014; Grossart et al., 2011) are about one to five orders of magnitude lower than our estimates.

Negative values of reaction rates (indicating consumption in the SML) obtained from the mass balances are expected to result from microbial CH_4 oxidation (MOx), which is occurring under oxic conditions in the epilimnion and hypolimnion (Guérin & Abril, 2007). Excluding the very particular period of C6-M-Dry, our MOx values, are 2 or 3 orders of magnitude higher than those reported for natural oligo-mesotrophic lakes (4 – 60 nmol L^{-1} d^{-1}) (Bogard et al., 2014; Donis et al., 2017) and oligotrophic tropical reservoirs (26 nmol L^{-1} d^{-1}) (Soued & Prairie, 2021), while the exceptional high MOx during C6-M-Dry are in agreement with the oxidation rates found by (Guérin et al., 2007a) in the water column of a tropical eutrophic reservoir (134 - 1600 µmol L^{-1} d^{-1}).

Clearly, we found a very wide range and little consistency in the dominance of both competing processes (MOx or OMP), keeping open the discussion to the complexity of interactions between drivers/inhibitors of CH_4 metabolism under eutrophic conditions and extreme periods such as C6-M-Dry. For example, our estimates of methane production near the dam during the last campaign (~50 µmol L-1 d^{-1}) are contradicted by methane loss when the concentration decreased between P1-M and P1-A (Figure 2-11e and Figure S16). The second measurement, however, was made after a very intense rain event (Figure S16) where k_{600} may have increased significantly (Ho et al., 1997) and surface methane may have been evaded rather than biochemically consumed. We cannot be certain that this happened considering that fluxes were not measured during the rain event, but this seems likely evidence that short-term events such as rainfall may play an important role in greenhouse gas emissions and balance in lakes and reservoirs, as other authors have found in field and experimental studies (Guérin et al., 2007a; Ho et al., 1997; Ojala et al., 2011). There are also scientific evidence that other highly variable factors may be involved in CH_4 dynamics such as oxygen concentrations and light exposure that have been shown to be inhibitory to MOx (Rudd et al., 1976; Tang et al., 2014).

2.4.3. Gas transfer velocities k_{600}

As the mass balances indicated that together with the reactions, evasion was an important term of the mass balances, it is important to look at the physical drivers of the gas transfer velocity (k_{600}) at greater details.

Both, the measured ($k_{600\_CH_4}$) and modeled gas transfer velocities (k_{600_mod}) agree with the ranges found in previous studies in tropical reservoirs (Guérin et al., 2007b; Paranaíba et al., 2018a) and in temperate lakes and reservoirs (MacIntyre et al., 2010; Vachon et al., 2010).

The coefficients of determination (~ 0.6) showed acceptable agreement between the gas transfer velocities estimated from CH_4 flux measurements and the ones predicted by empirical wind-based models (J. Cole & Caraco, 1998a; MacIntyre et al., 2010; Wanninkhof, 2014). Similar good correlations were found for the different approaches to estimate the k_{600} from the surface renewal model (SRM). However, existing wind-based empirical models underestimated k_{600} by a factor of 1.5 to 3.5, suggesting that the typically applied models could significantly underestimate the fluxes in tropical reservoirs, whereas the SRM could be fitted to our field data. The empirical coefficient A in the SRM varied from 0.72 to 0.8 for the two different approaches we used to calculate dissipation rates. These values are higher than most reported coefficients estimated from observations in large lakes and in the open ocean, which range from 0.25 – 0.44 (Esters et al., 2017; Vachon et al., 2010; Zappa et al., 2007) but lower than the few reported values found in temperate lakes and open ocean ranging from 1.2 to 1.6 (Esters et al., 2017; MacIntyre et al., 2010). To our knowledge, it is the first time that the empirical coefficient in the SRM was estimated for a tropical reservoir and more studies are required to confirm this relatively high coefficient for the specific hydrodynamic forcing conditions in these aquatic systems.

2.5. Conclusions

Our results demonstrate that the surface mixed layer (SML) is a zone of high microbial activity where reactions play an important role for the budget of CH_4 in tropical eutrophic systems. The surface dynamics change seasonally and the different components that contribute to the surface methane balance are affected by hydrological and meteorological conditions, suggesting that understanding of the surface processes involved in CH_4 dynamics of tropical eutrophic systems should be assessed on seasonal scales. Particularly, water level seems to play a relevant role, since in Porce III accumulation of CH_4 at the surface is higher at lower water levels. Also, diurnal patterns showed that CH_4 is more dynamic during daytime, showing generally higher changes over time associated to evasion and reactions, then only daytime sampling could cause bias in results.

Spatial patterns showed that towards the center to the transition zone of the reservoir, where the eutrophic condition was generally stronger, higher magnitudes of CH_4 reactions, and higher surface concentrations and emissions were also obtained. This is in agreement with recent studies associating photosynthetical activity with methane production. Importantly, our data frequently showed the occurrence of oxic methane production (OMP) in the SML and the high complexity of interactions between drivers/inhibitors of CH_4 metabolism under eutrophic conditions, especially in extremely dry periods. We strongly recommend that this be addressed in depth in future studies and directly measure the net production rates of methane.

Our measured gas transfer velocities were higher than those predicted from widely used wind-based models. The mechanistic surface renewal model reproduced well the field data of gas transfer velocity from the CH_4 chambers and the constant of proportionality A (~1) was higher than typical values reported in the literature. In this study we obtained a first model of the gas transfer velocity in an Andean reservoir that could be used as a reference for tropical eutrophic systems where, according to our results, the empirical wind-based models obtained for temperate zones could underestimate the emissions. The model should be carefully applied for similar conditions at which it was obtained: no-rain conditions, wind speed 0.5-7.8 m s^{-1} and for night times in places where the buoyancy flux or convection is not very strong.

3. Chapter 3: Observations on continuous monitoring of CO_2 fluxes in a eutrophic tropical Andean reservoir

3.1. Introduction

The physical processes affecting the dynamics of greenhouse gas (GHG) fluxes in reservoirs and other surface water bodies are related to the permanent and variable physical conditions of the study area. For example, it is presumed that topography in mountainous areas could function as a barrier to wind, favoring the dominance of other physical processes beyond permanent wind turbulence (Eugster et al., 2003). On the other hand, the environmental conditions that act as hydrodynamic forcing, which favor or disfavor the flux of gases at the water-air interface, change on different time scales such as seasonal and other smaller ones such as diurnal, therefore, it is expected that the physical processes involved in the behavior of GHG will also have variations on these same time scales.

Diurnal dynamics in GHG fluxes from inland waters have been primarily related to variations in surface heat exchange patterns between day and night (Czikowsky et al., 2018; Liu et al., 2016). Liu et al. (2016) found that nighttime CO_2 flux was approximately 70% greater than daytime fluxes in a temperate reservoir, largely as a result of heat loss and wind-induced processes. Poindexter et al. (2016) found, in a natural temperate wetland, that convection-enhanced diffusion contributed 54% of total nighttime CH_4 flux versus 18% of total daytime emissions. Anthony & MacIntyre (2016) note that the implications for tropical systems may be greater due to their typical strong convective processes. Besides physical processes that act as hydrodynamic forcings that increase or decrease the gas transfer velocity, the diurnal behavior of CO_2 flux may be associated with biochemical processes such as photosynthetical activity of algae at the water surface.

Most studies have focused on measuring the seasonal scale of GHG fluxes, since, for example, in temperate and boreal zones, seasonal changes are of great magnitude. On the other hand, obtaining results on a diurnal scale is not easy, and implies an additional sampling effort that is not always possible, for example due to safety or logistic conditions, in the case for example of discrete measurements such as by the method of manual floating chambers that requires human operation. Therefore, estimating CO_2 emission rates are usually conducted during daytime when fair weather conditions predominate. Automatic equipment can overcome these limitations by providing flux results with high resolutions. Unlike manual floating chambers, some technologies now allow data to be obtained continuously during day and night for time periods of several continuous months, resulting in the possibility of observing diurnal and seasonal dynamics, when this equipment can be installed long enough to reach seasonal changes.

The best-known methods for continuous GHG flux measurements are eddy covariance and automated chambers (Erkkilä et al., 2018). However, both are expensive and involve large investments in equipment and may require extensive data postprocessing (Bastviken et al., 2015). The EosFD (Eosense) is a relatively low-cost equipment that allows continuous measurements of CO_2 flux to be obtained through a forced diffusion (FD) dynamic chamber initially developed for soil fluxes (Risk et al., 2011), but directly transferable to the aqueous environment (Spafford & Risk, 2018). The dynamic chamber consists of a closed cylinder equipped with a membrane through which atmospheric air is pumped at a controlled rate to establish equilibrium between the atmosphere and the water surface gases rising into the chamber (Risk et al., 2011). The amount that the membrane limits the flow of gas out of the chamber is known, and thus by comparing the internal concentration to that outside of the instrument, the flux rate can be calculated. The relationships between these parameters are linear, and everything except the water surface and atmospheric concentrations are assumed to be constant, which simplifies to a single calibration slope (G). The flux is then calculated by multiplying the difference in water surface and atmosphere concentrations by the calibration slope (Inc, n.d.):

$$F_{FD} = G\,\frac{C_{cham} - C_{atm}}{A_s} \tag{3-1}$$

where G is the pump speed at which air is being drawn through the chamber, C_{cham} is the concentration of the chamber as measured in the outlet, C_{atm} is the concentration entering the chamber and A_s is the area of the chamber in contact with the water surface.

In this study, we used an FD chamber to observe and understand the dynamics of the CO_2 flux at diurnal and seasonal time scales in Porce III reservoir. It was hypothesized that wind might not be the most important factor for gas transfer velocity at the water-atmosphere interface all the time. During the field work conducted in Porce III reservoir (see Chapter 2), diurnal cycles of wind speed with low values at night (< 3 m/s) and in the morning, and higher wind speeds in the afternoon (~ 5 m/s) were observed. In addition, diurnal cycles of surface heat flux showed heat loss (negative buoyancy flux) in the reservoir at night. According to these diurnal meteorological cycles at Porce III and the associated available theory, the predominance of physical processes influencing GHG dynamics in the study area could vary on a diurnal scale, having a predominant convective mixing by cooling during the nights and an intermittent surface turbulence produced by wind shear stress in the afternoons, when wind speed is higher, both promoting the gas transfer velocity and improving the CO_2 flux at the air-water interface. Also, a permanent eutrophic condition may control the diurnal dynamics of the CO_2 surface fluxes in Porce III reservoir. Understanding these dynamics could be representative for explaining GHG behavior in reservoirs under similar meteorological and topographical conditions at low latitudes.

3.2. Methods

3.2.1. Study site and sampling period

We conducted this study in the Porce III reservoir, as in the study referred to in Chapter 2. This time we focused on the sampling station in the dam zone (P1) (Figure 3-1). The climate of the study area is determined by the bimodal regime characteristic of the Colombian Andes, where there are two dry seasons (January-February and July-August) and two wet seasons per year (April-May and October-November), with the other months acting as transition periods. This regime is frequently affected by the El Niño–Southern Oscillation (ENSO).

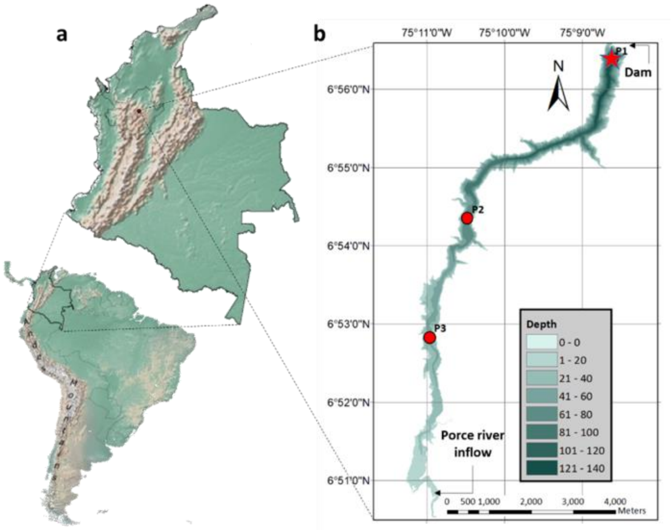

Figure 3-1. Porce III location and bathymetry of Reservoir. a) The continental and regional location showing the study area placed in the Colombian Andes. b) Bathymetry of the reservoir with color scale contours of the water depth, the location of the Porce river entry, the dam and the sampling stations (the star symbol marks the point where the measurements for this study were performed)

CO_2 flux, meteorological data and surface water temperature were collected over three multi-week periods between November 2019 and December 2021 for a total of 134 sampled days (Table 3-1). The three sampling periods were named according to the hydrological condition of the basin. Following the climatic regime in the study zone, the last measurement period can be sub-divided in three sub-periods (Table 3-1), but it is important to mention that all third period was affected by La Niña[a] which is associated with wetter weather in the study region.

---

[a] Information available in: https://origin.cpc.ncep.noaa.gov/products/analysis_monitoring/ensostuff/ONI_v5.php

Table 3-1. General description of the study periods. ID campaign indicates sampling period (SP1 to SP3) and basin's hydrological condition (Wet season "Wet", Wet-dry transition "WDT", Dry season "Dry", Dry-wet transition "DWT"). *Based on the monthly reports from the Institute of Hydrology, Meteorology and Environmental studies of Colombia -IDEAM)

Sampling period	**ID**	**Date**	**Basin's hydrological condition***
1	SP1-WDT	29/Nov to 10/Dec/2019	Wet-dry transition
2	SP2-Dry	10 to 25/Feb/2020	Dry season
3	SP3.1-DWT	06/Sep – 08/Oct/2021	Dry-Wet transition, wetter than normally because of La Niña
3	SP3.2-Wet	08/Oct – 30/Nov/2021	Wet season, wetter than normally because of La Niña
3	SP3.3-WDT	30/Nov to 10/Dec/2021	Wet-Dry transition, wetter than normally because of La Niña

3.2.2. Data collection

A floating circular monitoring platform was designed to support the equipment described below and a mast for mounting part of the system that must remain dry (power supply system, loggers and the weather station) (Figure 3-2). The platform was constructed based on a sandwich design made of wood expanded polystyrene in the middle and wood on outside and waterproofed with epoxy paint. Once on the water surface, a ballast was installed with leftover rope to allow the platform to float even with reservoir level changes and empty containers were distributed on the platform to reinforce its buoyancy. The EosFD was installed in a hole in the structure and fastened with plastic straps tensioned to the platform to give it stability. A thermistor was installed with a 20 cm rope below the platform.

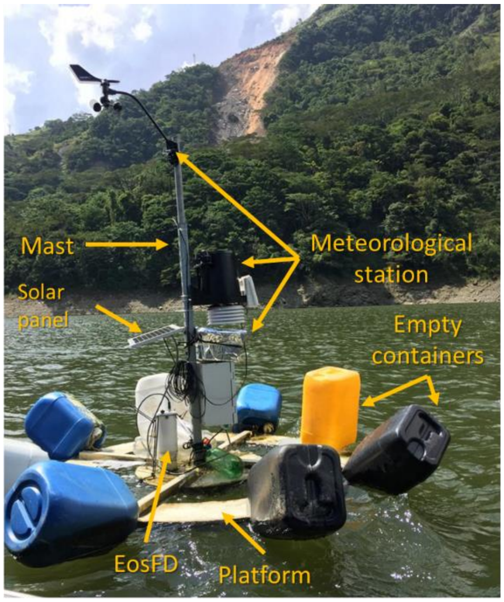

Figure 3-2. Floating platform and equipment assemblyon the water surface of the Porce III reservoir.

A closed chamber of forced diffusion (EosFD of Eosense) was installed on the floating platform near the dam (P1) to monitor water-air CO_2 flux continuously with a sampling resolution of 30 minutes. Also, a Davis Vantage Pro2 digital weather station was installed on the platform (anemometer at 2.0 m above water surface) to monitor meteorological variables including wind speed, air temperature, relative humidity, atmospheric pressure and solar radiation with a sampling resolution of 30 minutes. Data were also available from a fixed meteorological station (El Roble), located on land 2.7 km from the reservoir at coordinates 06°57'41.9"N, -75°07'55.7"W. The floating station was taken as the main data source for the analysis due to its ideal location in relation to the flux measurements, and missing data were filled after correlation with data from the station El Roble (Table S2 – Chapter 2).

Surface water temperature was monitored with 30-minute resolution using Hobo thermistor located at 0.2 m depth and cloud cover was obtained from ERA 5 reanalysis data with hourly resolution (Hersbach et al., 2020). Air temperature, relative humidity, cloud cover and wind speed were collected for the whole study period, while surface water temperature was missing for the period 13 to 24/Dec/2019.

3.2.3. Data processing

The software Matlab 2021a was used for the data processing. Some time series were resampled at 30 minutes using the function *retime* by the method *linear*. This is the case of the CO_2 flux during the period SP1-WDT which was taken originally at 5 minutes' resolution and cloud cover which was at 1 h of resolution. Then, all variables were time-synchronized with the CO_2 flux time series every 30 minutes along the entire study period.

- Data overview and temporal variability

In order to make observations on the variability of CO_2 flux, time series were plotted, descriptive statistics calculations were performed, and a box-plot analysis was made with different data sets: hourly and monthly where the edges of the box are the 25th and 75th percentiles and the whiskers extend to the most extreme datapoints the algorithm considers to be not outliers (MathWorks Inc., 2021).

Since photosynthetical activity was not sampled in this study, the hourly variability of fluxes was compared graphically only with the variability of wind speed and buoyancy flux under the hypothesis that these two variables are the main drivers of the partially k_{600}-dependent CO_2 flux.

- Relationships between CO_2 flux and meteorological forcings

Relationships between meteorological forcings and CO_2 flux were analyzed from regressions and Pearson correlation coefficients (r), computed for each meteorological variable versus CO_2 flux, using the function *corr* (MathWorks Inc., 2021). Atmospheric pressure was excluded from this analysis because the sensor was not calibrated for the entire study period and, during previous monitoring (Chapter 2), this variable did not show big temporal changes in the study site. Additional to the measured meteorological variables, the friction velocity (u^*) and the buoyancy flux (β) were calculated following Equations (3-2) and (3-3), respectively and the relationships of these two variables to the CO_2 flux were explored individually as was done with the meteorological variables. To test the influence of the wind speed magnitude on the CO_2 flux, Pearson correlations were performed for the data by gradually increasing the lower limit of the wind speeds to be correlated. In the same way and based on the theory that only negative buoyancy flux (β^-), meaning cooling, can influence gas fluxes at the water-atmosphere interface, comparative correlations were performed between all the buoyancy flux data (positive β^+ and negative β^-) and the series including only β^-.

$$\mathrm{u}^* = \left(\frac{\rho_a C_d {U_{10}}^2}{\rho_w}\right)^{0.5} \tag{3-2}$$

$$\beta = (\mathrm{g}\, \alpha\, H)/(c_{pw}\, \rho_w) \tag{3-3}$$

where u^* is the friction velocity computed from shear stress at the air-water interface following (MacIntyre et al., 2002), κ is the von Karman constant (0.41), z is the water depth taken as 0.15 m, ρ_a and ρ_w are the density of air and water, respectively. U_{10} is the wind velocity 10 m above the water surface and C_d is the drag coefficient, g is the gravitational acceleration, α is the thermal expansion coefficient, c_{pw} is the specific heat of water and H is the net surface heat flux entering the reservoir, calculated as follows:

$$H = SW_{net} + LW_{net} + H_{sens} + H_{lat} \tag{3-4}$$

where SW_{net} is the net short wave radiation flux, LW_{net} is the net long wave radiation flux, H_{sens} and H_{lat} are the sensible and latent heat fluxes, respectively. Both H and β were limited to the periods with surface temperature recording with the thermistor. Inlets were taken as positive. Details on the calculations are in Appendix A - Table S4.

NOTE: for practical purposes, flux sign conventions were defined inversely for CO_2 flux (positive from water to atmosphere) and heat fluxes (positive from atmosphere to water).

- Physical processes influence on CO_2 flux

According to Fick's first law, gas flux at the water-atmosphere interface is partially dependent on physical processes that express through the gas transfer velocity. Therefore, in theory, both wind speed and buoyancy (β) flux would influence CO_2 flux to the extent that it affects the gas transfer velocity (k_{600}). To verify this influence, the surface renewal model was used to calculate *k600* on the basis that they probed to work for CH_4 measured *k600* (r^2 >0.6), following Equation (3-5). Since only negative buoyancy flux (β^-) is considered in the *k600* calculation, linear and nonlinear regressions for different wind speed ranges were performed excluding positive values of buoyancy flux.

$$k_{600} = A\ 600^{-n}(\epsilon v)^{1/4} \tag{3-5}$$

where A is the empirical coefficient 0.8 according to the results presented in Chapter 2, κ is the von Karman constant (0.41), z is the water depth taken as 0.50 m following (Esters et al., 2017), ρ_a and ρ_w are the density of air and water, respectively and ϵ is the dissipation rate of the turbulent kinetic energy under cooling (β^-) (Equation (3-6)) or heating (β^+) (Equation (3-7)):

$$\epsilon = c_1(\mathrm{u}{*}^3/(\kappa\, z\,)) + c_2\beta\ ;\ \beta < 0 \tag{3-6}$$

$$\epsilon = c_1(\mathrm{u}{*}^3/(\kappa\, z\,));\ \ \beta > 0 \tag{3-7}$$

where β is the buoyancy flux, c_1 and c_2 were 1.5 and -0.5, respectively (MacIntyre et al., 2010), g is the gravitational acceleration, α is the thermal expansion coefficient, H is the net surface heat flux and c_{pw} is the specific heat of water.

3.3. Results

3.3.1. Data overview and time series

The time series showed diurnal cycles of several variables such us CO_2 flux and wind speed where peaks and valleys are observed. Naturally, there are also diurnal cycles in solar radiation which is reflected in the buoyancy flux (β) cycles (see section 3.3.4). CO_2 pulses observed in the three sampling periods such us the ones from 30/Nov to 02/Dec/2019, 22/Feb to 25/Feb/2020 and 25 to 28/Nov/2021, occurred mostly in the afternoon. However, it is observed that during long periods the average flux increase during the night as clearly observed from 11 to 21/Feb/2020, almost all of Sept and Oct/2021 and from 17 to 21/Nov/2021 (Figure 3-3 to Figure 3-7).

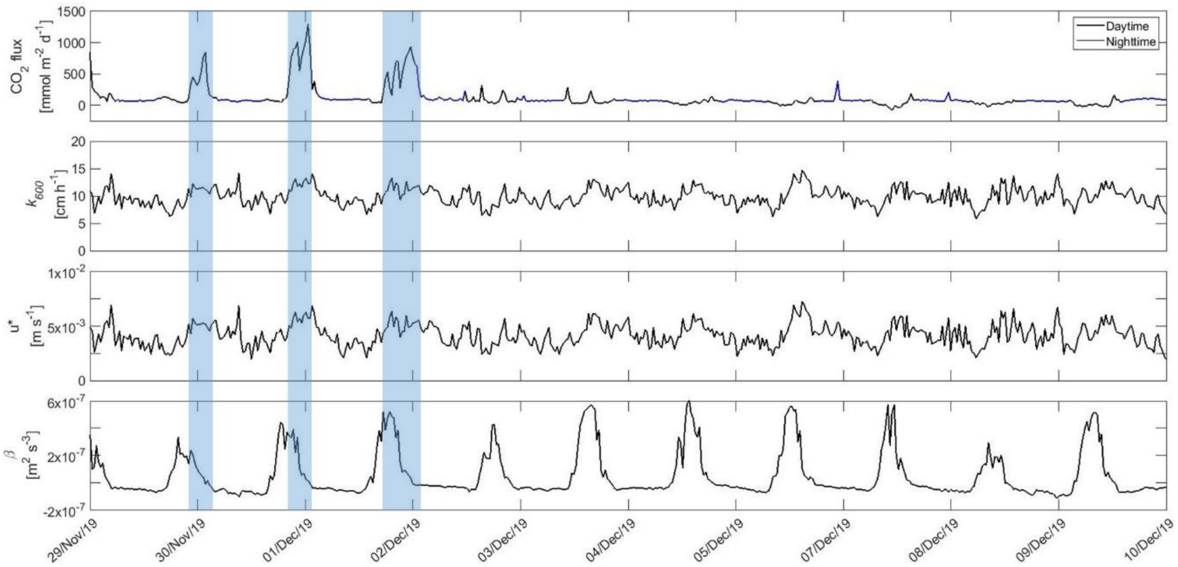

Figure 3-3. Time series of CO_2 flux, k_{600}, friction velocity and buoyancy flux (30 min resolution) during SP1-WDT. Blue shadows highlight observed CO_2 flux pulses.

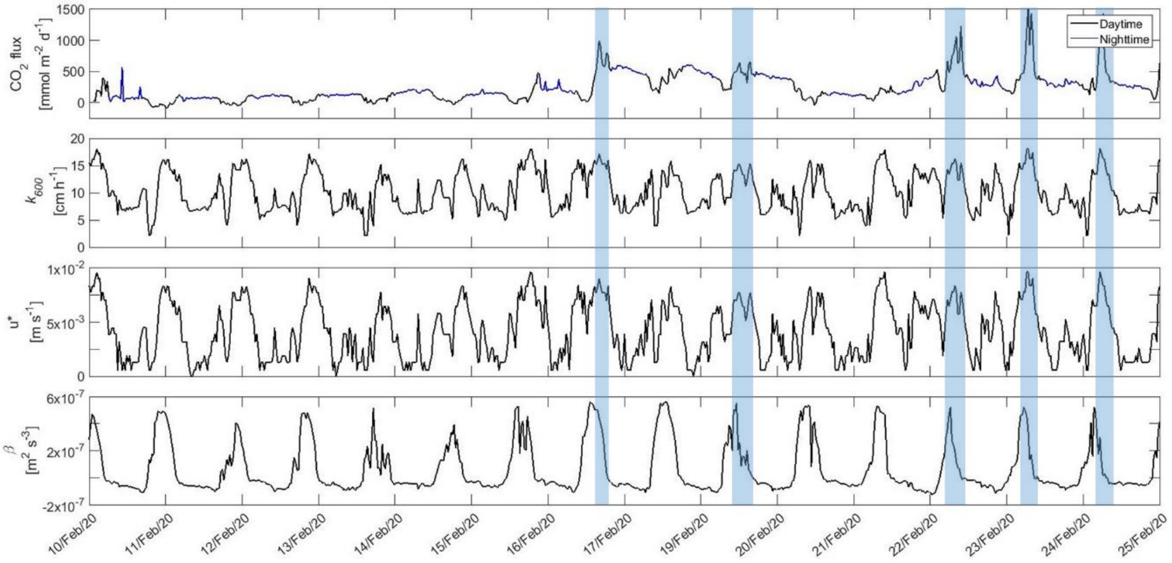

Figure 3-4. Time series of CO_2 flux, k_{600}, friction velocity and buoyancy flux (30 min resolution) during SP2-Dry. Blue shadows highlight observed CO_2 flux pulses.

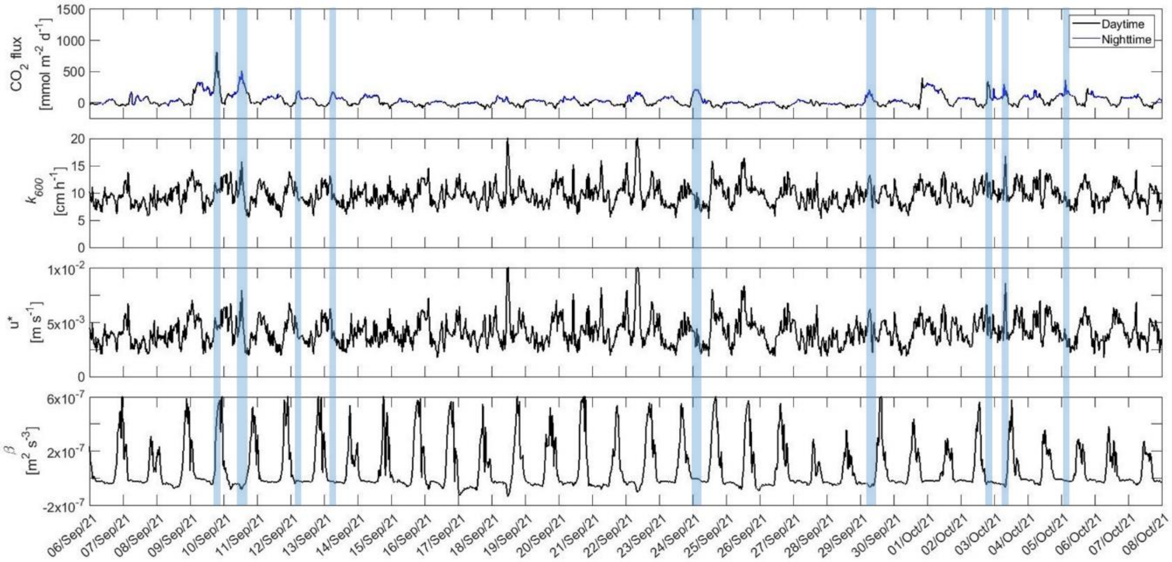

Figure 3-5. Time series of CO_2 flux, k_{600}, friction velocity and buoyancy flux (30 min resolution) during SP3.1-DWT (06 to 30 September*)* and a partial period of SP3.2-Wet (01 to 08/Oct/2021). Blue shadows highlight observed CO_2 flux pulses.

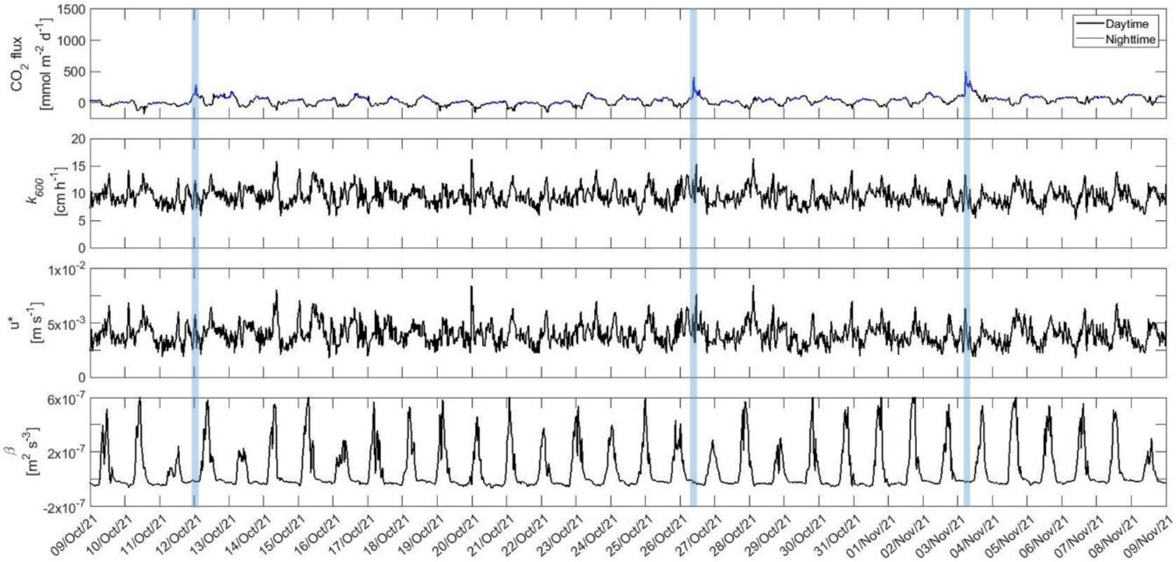

Figure 3-6. Time series of CO_2 flux, k_{600}, friction velocity and buoyancy flux (30 min resolution) during a partial period of SP3.2-Wet (09/October 09/Nov/2021*).* Blue shadows highlight observed CO_2 flux pulses.

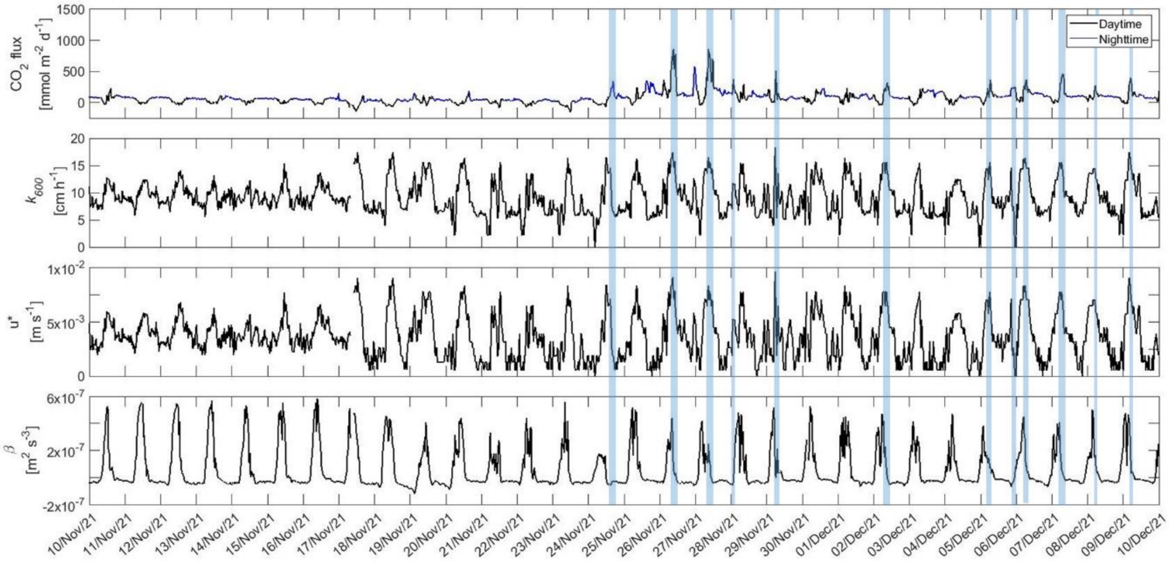

Figure 3-7. Time series of CO_2 flux, *k_{600}*, friction velocity and buoyancy flux (30 min resolution) during a partial period of SP3.2-Wet (10 to 30/Nov/2021*)* and SP3.3-WDT. Blue shadows highlight observed CO_2 flux pulses.

Most of the CO_2 flux were in the range of -100 to 250 mmol m^{-2} d^{-1} (Figure 3-8) (mean ± std: 85.4 ± 152 mmol m^{-2} d^{-1}). These results agree with the flux measured with floating chambers during the period May/2017 to Feb/2019 (Chapter 2) where the flux ranged from -53 to 320 mmol m^{-2} d^{-1} (mean 12 ± 199 mmol m^{-2} d^{-1}). In addition, some peaks up to >1500 mmol m^{-2} d^{-1} as well as low negative values (-174 mmol m^{-2} d^{-1}) were captured with the EosFD that are difficult to capture with discrete methods such as manual floating chambers.

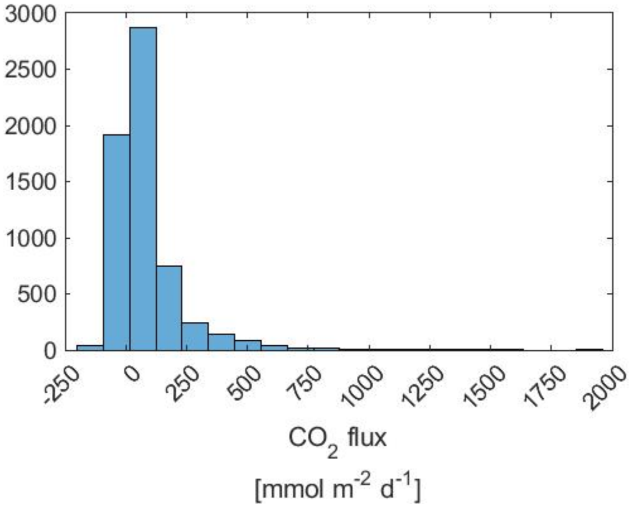

Figure 3-8. Histogram of CO_2 flux measured with the EosFD in Porce III for the entire study period

The average meteorological variables during the study period reflect the typical conditions of the wet tropical forests of the Colombian Andes (Table 3-2): small seasonality in solar radiation, high water and air surface temperatures, both around 25°C, high relative humidity (88% on average) and high cloud cover (80% on average). In particular, during Dec/2019 - Jan/2020 there were strong dry conditions where relative humidity and cloud cover reached very low values of 33% and 0%, respectively, and air temperature went up to 35°C. The maximum wind speed during the study period was 9.3 m s^{-1} in Sep/2021 (mean U_{10} of 3.2 m s^{-1}).

Table 3-2. Meteorological variables during the study period from 19-Nov-2019 to 09-Mar-2020 and 01-Sep-2021 to 10-Dec-2021. Minimum (min), maximum (max) and mean ± standard deviation (std).

Variable	Units	min	max	mean ± std
Surface water temperature	°C	23.1	29.9	25.1 ± 1.0
Air temperature	°C	19.8	34.6	24.6 ± 2.1
Relative humidity	%	33.0	97.0	88.0 ± 8.7
Cloud cover	-----	0.00	1.00	0.79 ± 0.28
Wind speed (U_{10})	m s^{-1}	0.0	9.3	3.2 ± 1.6
Friction velocity (u*)	m s^{-1}	0.0	1.1×10^{-2}	3.9×10^{-3} ± 1.6×10^{-3}
Buoyancy flux (β)	m^2 s^{-3}	-1.4×10^{-7}	6.9×10^{-7}	6.4×10^{-8} ± 1.6×10^{-7}
Net heat flux (H)	W m^{-2}	-230	1057	101 ± 263

3.3.2. Seasonal variability

Some aspects of seasonality were observed when comparing months and sampling periods (Figure 3-9). Although there do not appear to be statistically significant differences (overlapping boxes), there is a pattern that repeats in two periods, in which from a rainy month (November) flux increases towards the wet-dry transition period (December) in both 2019 and 2021. In particular, from the transition period measured in November-December 2019 (SP1-WDT) to February 2020 (dry season) there is an increase in flux and data variability. During SP1-WDT, the mean CO_2 flux was close to 100 mmol m^{-2} d^{-1}, the variability increases since November to December 2019 and Febraury 2020 as well as the mean flux which duplicates by Febraury 2020. During 2021 a constant increasing was showed from September to December ranging from about ~0 to 100 mmol m^{-2} d^{-1}.

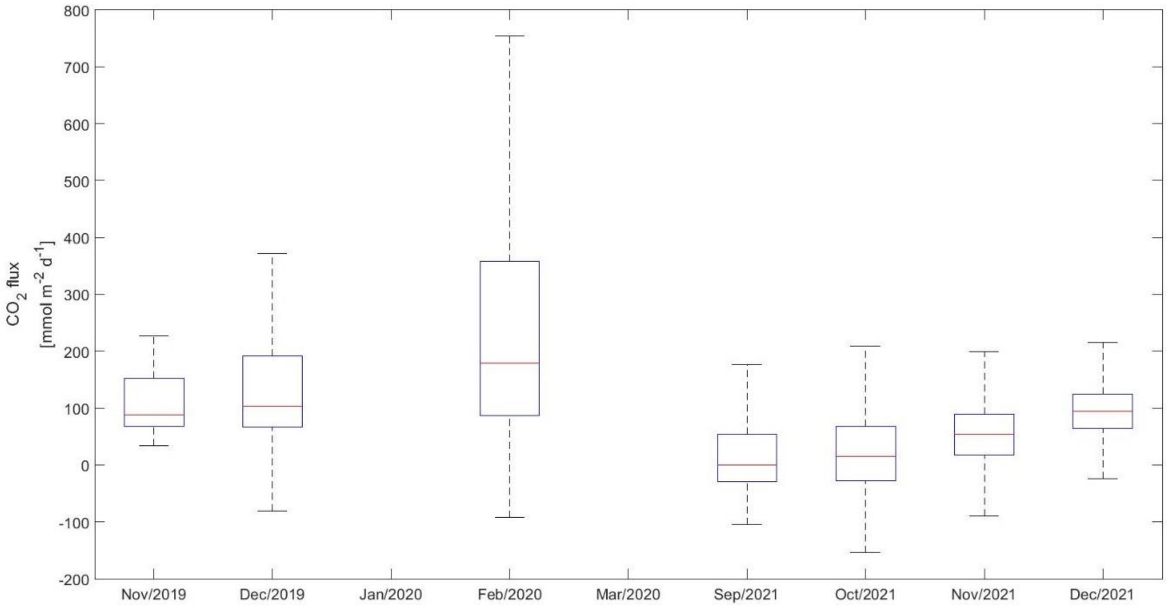

Figure 3-9. Box-plot of CO_2 flux for sampling months.

3.3.3. Diurnal cycle

Observations in the diurnal cycle confirm some of the observations made during the floating chamber measurements for the period May/2017 to February/2019 (Chapter 2), where no negative fluxes were found during nights and alternating between positive and negative during daylight hours. Here it can be clearly seen that, during nights, CO_2 flux are on average positive and during five hours of daytime they are negative in average (from 10:00 to 15:00), but alternating with positive fluxes according (Figure 3-10). The hours of highest variability are around 17:00, suggesting that peaks of CO_2 flux may be produced around this time.

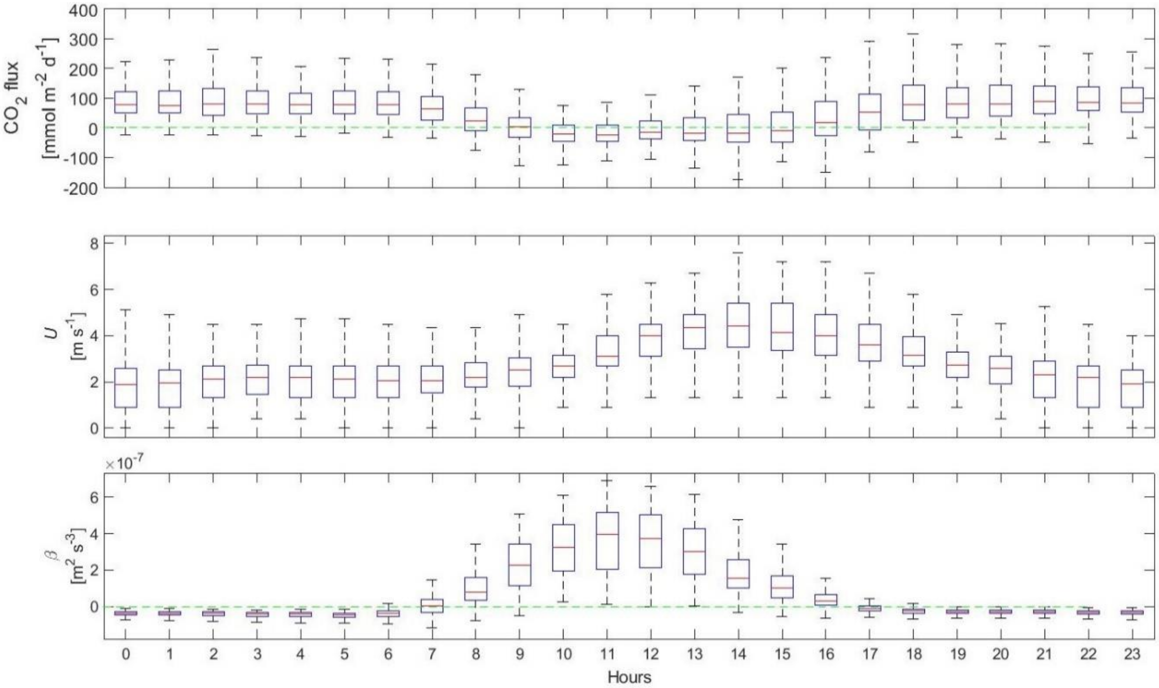

Figure 3-10. Box-plot of CO_2 flux, wind speed (U) and buoyancy flux (β) by hours. Dashed green lines mark the zero in the upper and the lower panels.

Wind speed showed higher values in the afternoon hours in a steady increase between 09:00 and 14:00, while during all night hours, early morning and until 8:00 the average remains around 2 m s^{-1} without much hourly variation.

It can be noted that the hours of higher wind speed coincide with the hours of negative average CO_2 flux and also the opposite. The only way to obtain negative CO_2 flux (from air to water) is for surface CO_2 concentrations to be undersaturated, these results reinforce the idea that the eutrophic state of the reservoir generates surface CO_2 consumption during certain daylight hours (Chapter 2), to the point of decreasing the concentration of the dissolved gas below saturation. The increase in wind speed just at the hours of greatest photosynthetical activity could favor the CO_2 sequestration process by increasing the efficiency in the flux air-water.

On the other hand, the buoyancy flux draws a mirror hourly behavior of CO_2 flux, where during daytime hours (08:00 to 16:00), the buoyancy flux is positive (heat entering the reservoir) and relatively variable and during nighttime hours (17:00 to 06:00) the buoyancy flux is negative (cooling) and with very low variability. At first look, these results would suggest that CO_2 flux are directly related to the behavior of surface heat flux, where cooling causing negative buoyancy fluxes would generate increasing in CO_2 flux to the atmosphere. However, this observation in the time series patterns does not necessarily imply causality, and this statement would only be true if CO_2 concentrations remained oversaturated and with low variability, so the increase in CO_2 flux would depend primarily on the increase in the gas transfer velocity rather than the chemical changes. The relationship between buoyancy flux as a physical forcing and CO_2 flux is explored in more detail in sections 3.3.4 and 3.3.5.

3.3.4. Relationships between CO_2 flux and meteorological variables

Weak correlation ($r < 0.19$) were observed for the linear correlations of CO_2 flux with each of the meteorological variables measured and the calculated buoyancy flux (β), without excluding data ($n = 5857$). Within these poor correlations, the best coefficients were found for cubic friction velocity ($r = 0.21$), buoyancy flux ($r = -0.19$) and solar radiation ($r = -0.18$) (Table 3-3), in agreement with the behavior observed in the diurnal cycle of CO_2 flux and buoyancy frequency (section 3.3.3).

Table 3-3. Pearson correlation coefficients for meteorological variables vs. CO_2 flux ($n = 5857$)

Variable	**Pearson coefficient (*r*)**	**Variable**	**Pearson coefficient (*r*)**
CO_2 flux	1.000	Solar radiation	-0.176
Wind speed (U)	0.092	Water temperature	-0.039
Air temperature	-0.055	Cloud cover	-0.089
Relative humidity	0.076	Cubic friction velocity (u^{*3})	0.214

Variable	Pearson coefficient (*r*)	Variable	Pearson coefficient (*r*)
Total rain	-0.009	Buoyancy flux (β)	-0.187

Scenarios varying ranges of wind speed and buoyancy flux (β) are shown in Figure 3-11. Under scenario 2, the correlation of β versus CO_2 flux improves substantially when only wind speeds <1 m s^{-1} are included, indicating that β has a greater ability to influence CO_2 flux at very low wind speeds. Supporting this result, the correlation between β and CO_2 flux gradually decreases (*r* from 0.19 to 0.02) under scenarios where wind speed increases (scenarios 4 to 8). According to theory, the correlation between CO_2 flux and β would be expected to improve when only negative buoyancy fluxes (β^-) are included. In contrast, when comparing scenarios 2 and 3, a substantial decrease in the correlation coefficient (*r* from 0.26 to 0.16) is observed when only β^- are included, indicating that possibly, β^+ could influence the flux of gases into the atmosphere in the opposite way as β^- does, i.e., by inhibiting the flux of gases at the interface. However, as it was said above this behavior may be the result of the sun driving photosynthesis which leads to uptake CO_2 during the same times that β is positive. Scenarios in which the lower wind speed limit is modified to include only increasingly higher wind speeds (scenario 1, 4 - 8) as well as scenarios where only very low wind speeds are considered (scenarios 2 and 3) show that wind speeds > 4 m s^{-1} influence CO_2 flux more than lower wind speeds (up to r = 0.32), while wind speeds <1 m s^{-1} do not influence CO_2 flux or could even be associated with physical processes inhibiting fluxes causing negative correlations (r -0.09 to -0.1) (Figure 3-11).

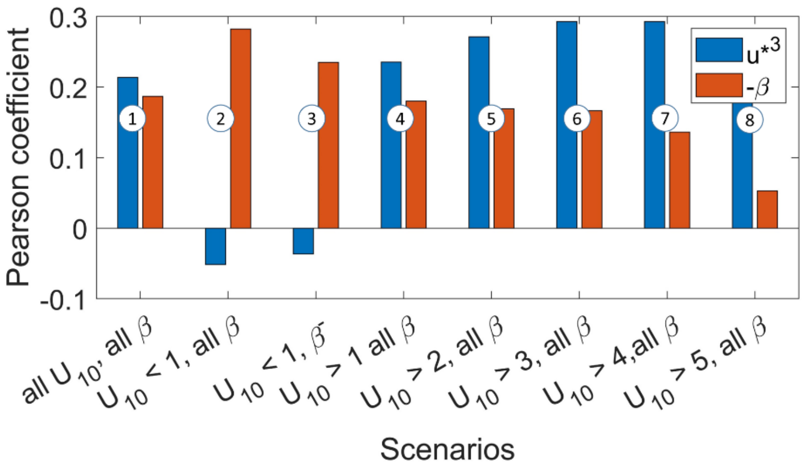

Figure 3-11. Pearson correlation coefficients between cubic friction velocity (u^{*3} in m s^{-1}) (blue bars) and inverse of buoyancy flux (-β) (red bars) and CO_2 flux under different

scenarios. The labels below the bars indicate the data included in the analysis and the circles at the top show an ID number for each scenario.

The results presented so far suggest that β could influence importantly on the dynamics of CO_2 flux at low wind speeds. However, this statement may have a bias related to photosynthetical activity, since both algal activity and buoyancy flux are a function of solar radiation and coincide in their dynamics inversely. During the day, algae consume CO_2 generating negative CO_2 flux (sequestration) and the water surface gain heat producing positive buoyancy flux whereas during the night, the opposite is true.

In the case of Porce III reservoir, the dominant term of the surface heat balance is shortwave radiation (Chapter 2) and the correlation between solar radiation and buoyancy flux is close to 1 (Figure 3-12), indicating that possibly the correlations between buoyancy flux and CO_2 flux are biased by time of day.

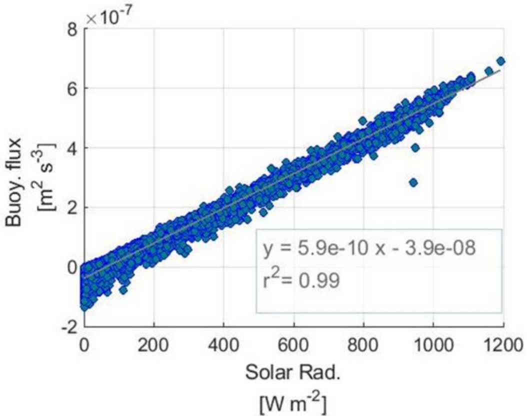

Figure 3-12. Buoyancy flux vs. Solar radiation

3.3.5. Gas transfer velocity

The gas transfer velocity (k_{600}) is closely related to the friction velocity and wind velocity, the time series show almost identical behaviors when wind speed (U), friction velocity (u*) and k_{600} are compared with each other (Figure 3-3 to Figure 3-7). The k_{600} and CO_2 flux series are not identical, but the CO_2 flux peaks coincide in almost all cases with k_{600} peaks caused by high wind speeds (between 4 and 6 m s^{-1}). In many cases, the CO_2 flux peaks occur in periods of few days in a row, followed by periods of several days where the fluxes show the almost sinusoidal behavior caused by daytime-nighttime differences, without peaks, unlike wind speed and k_{600} which do have a cycle that remains constant throughout the study period. This suggests that the peaks of CO_2 flux, although associated with high wind speeds, do not depend exclusively on these, but indicate the simultaneous occurrence of high wind speeds and high CO_2 concentrations at the water surface.

3.4. Discussion

3.4.1. CO_2 flux general behavior

Although the ranges were similar in forced diffusion (FD) and previous results from floating chambers (FC) in Porce III (from -100 to 250 mmol m^{-2} d^{-1} FD versus from -53 to 320 mmol m^{-2} d^{-1} FC), high-intensity measurements of CO_2 flux by FD showed that the mean (85.4 ± 152 mmol m^{-2} d^{-1}) was 7 times higher than previous FC results (12 ± 199 mmol m^{-2} d^{-1}, taking all accepted measurements). This discrepancy could be related to the fact that the high-resolution measurement allows nighttime fluxes and short-duration peaks to be available that are not taken by mainly diurnal discrete sampling with FC.

Diffusive fluxes of CO_2 measured in other tropical reservoirs have variable results presented by previous studies. It should be noted that most of them were probably monitored during the daytime, which is not always reported in the articles since the objective was not to explore diurnal cycles. Lower values were found at Balbina reservoir, 76 ± 46 mmol m^{-2} d^{-1} (Guérin et al., 2006) and, contrary to our results, at Petit Saut (Abril et al., 2005) it was found that undersaturation in CO_2 with respect to the atmosphere was only occasionally observed in the reservoir. However the average CO_2 flux of Petit Saut (Abril et al., 2005) as well as that of Itaparica (Rodriguez & Casper, 2018) were in the same order of magnitude as mean of Porce III (~10^2 mmol m^{-2} d^{-1}). Similarly, Kemenes et al. (2011) found no negative fluxes in the Balbina reservoir (range 28 - 710 mmol m^{-2} d^{-1}) and a high average of 315 mmol m^{-2} d^{-1} indicated heterotrophic dominance in the reservoir. This comparison of results reveals that the trophic status is crucial in determining the average CO_2 flux in a tropical reservoir, thus eutrophic reservoirs with strong primary productivity, i.e. autotrophic systems, are expected to generate lower mean CO_2 emissions than heterotrophic systems.

Periods of several days were observed in which daily peaks were present and periods in which they were not. This is usually attributed to meteorological events promoting a multiplicative effect on the instantaneous atmospheric fluxes (Abril et al., 2005; Liu et al., 2016). Accordingly, we observed peaks that coincide with high wind speed, but we also observed that wind speed peaks do not necessarily generate peaks in fluxes, suggesting that simultaneous to meteorological forcings surface CO_2 accumulation must occur to produce the instantaneous CO_2 flux. (Guérin et al., 2006) also obtained CO_2 flux up to 1834 mmol m^{-2} d^{-1} attributed to meteorological conditions during the survey in Samuel reservoir (December 2005) enhancing the gas transfer velocity, while another sampling period showed a maximum of 169 mmol m^{-2} d^{-1} in the same reservoir (dos Santos et al., 2006).

3.4.2. Temporal variability of CO_2 flux

No significant seasonal differences of CO_2 flux were found at Porce III, but the pattern indicated a greater magnitude and variability in drier seasons. Since CO_2 flux is directly related to gas concentration at the surface, some comparisons with previous results of CO_2 concentrations are made below. According to our results no significant seasonal differences were found in Manso and Funil reservoirs in a Brazilian tropical savannah, but higher values were obtained in the dry seasons for the reservoirs when comparing areas with higher pCO_2 values on a seasonal scale (Roland et al., 2010). Likewise, fluxes at the Petit Saut reservoir showed little seasonal variation (Guérin et al., 2006). These results seem to indicate that seasonal CO_2 fluxes in the tropics are small, in contrast to boreal and temperate lakes and reservoirs, where seasonality has a large effect on CO_2 flux (Huotari et al., 2011; Liu et al., 2016; Shao et al., 2015).

Most of the field data collected for CO_2 evasion estimation have low temporal resolution, such as weekly to quarterly, ignoring the diurnal variation in the CO_2 flux (R. Yang et al., 2022). To our knowledge, this study is the first covering the high-resolution diurnal behavior of the CO_2 flux in a tropical reservoir. This study did not cover a complete hydrological cycle, but it can be considered representative, because of the low variability of the thermal dynamics in the seasonal scale at the study site. In Porce III, the variability of CO_2 flux in the diurnal cycle was clear: the reservoir tends to be a source of CO_2 to the atmosphere during late afternoon, night, and early morning (from 16h to 08h) and a sink during high solar radiation hours (from 10h to 15h). Still, high variability of CO_2 flux was observed, and negative and positive fluxes happen during the diurnal cycle, similar to the results in temperate lakes and reservoirs where eutrophic waters could function interchangeably as a CO_2 source and a CO_2 sink in a span of a day (Liu et al., 2016; Xu et al., 2019). Therefore, to limit the sampling to daytimes is very likely a bias in the results and it is needed to consider the changes in air-water CO_2 flux over the span of a day to limit the factors causing data scatters in higher spatial scales estimations (R. Yang et al., 2022).

The diurnal changes in CO_2 flux, particularly between day and night, may be associated to biological changes as well as thermal processes in the water surface. We did not measure biological activity, but results obtained in a past study strongly suggest that the Porce III reservoir remains eutrophic all the year (see Chapter 2). Graphically, there was coincident behavior when comparing buoyancy flux and CO_2 flux. On the other hand, solar radiation has a strong correlation with buoyancy flux (r^2 = 0.99) as well it does with unmeasured photosynthesis, indicating that the possible relationship between buoyancy flux and CO_2 flux may not be causal, and their coincident behavior is rather provoked by the dependence of both variables on solar radiation. We found that the weak magnitude of the buoyancy flux is unlikely to have a significant effect on the gas transfer velocity and, consequently, to increase mean fluxes during the night. Therefore, we infer that autotrophic metabolism is likely to have caused the increase in the average CO_2 flux at night relative to the daytime, as concluded in previous studies conducted in subtropical eutrophic lakes and reservoirs (Lin et al., 2019; Xu et al., 2019). Many hours per day of the Porce III reservoir is on average a source of CO_2 indicating that heterotrophic activity may play an important role in the variability of surface CO_2 concentrations and CO_2 flux, as (R. Yang et al., 2022) found in a subtropical lake.

Our results were partially in agreement with Liu et al. (2016) who concluded that primary production decrease in pCO_2 in the upper water column during the day, but mainly attributed the increased summer night CO_2 fluxes to physical processes. Their results indicated that heat loss and wind induced processes occurring at night explained a significant portion of the variability in CO_2 efflux (r^2 = 0.31). In contrast, we obtained poor correlation coefficients (*r*) when fulfilling some conditions: *r* of 0.26 ($r^2 = 0.07$) between CO_2 flux and buoyancy flux when wind speed was <1 m s^{-1}, and *r* of 0.32 ($r^2 = 0.10$) between CO_2 flux and wind speed when wind speed was >4 m s^{-1}. This supports the idea that biological factors are the main controllers of the average diurnal variability of the CO_2 flux in Porce III reservoir.

According to the diurnal dynamics showed here, we speculate that many of the published results of CO_2 flux could be underestimated in cases where the samples were taken by discrete methods, during daytime in the presence of photosynthesis and missing instantaneous peaks of flux. This is especially relevant in eutrophic systems, where the primary productivity plays an important role on the CO_2 surface dynamics and the diurnal cycle show big changes to an extend in which the same site passes from being a source to sink in a span of a day (Xu et al., 2019).

3.5. Conclusions

In this study the diurnal cycle of the CO2 flux in Porce III was clearly seen. During daylight hours, there is a high variability and alternation between the reservoir being a sink or source of CO_2 where the biology of the system is alternates the predominance of the photosynthesis (dominates between 10h and 17h) and respiration (dominates the rest of the day). Seasonal dynamics showed slight changes in CO_2 flux, where during drier times the CO_2 flux are higher and more variable than during wetter times. In general, the reservoir was a CO_2 source when averaged over long-term

Meteorological forcings such as wind speed and heat fluxes showed little dominance of the CO_2 flux and, although not measured, it appears that photosynthetical activity would dominate CO_2 flux dynamics in Porce III Reservoir. However, observations indicate that at wind speed > 4 m s^{-1}, peaks of CO2 flux can be generated if high surface CO_2 concentration occurs simultaneously. Although wind speed generally dominates gas transfer velocity, at wind speed < 1 m s^{-1}, negative buoyancy flux would be dominant, causing a possible impact on CO_2 flux, e.g., during the night, where wind speeds are very low, buoyancy flux is negative and surface CO_2 concentrations increase due to algal respiration.

For future work, we recommend long-term measurements to conclude on the complete hydrological cycle and based on a larger number of observations about the seasonal dynamics. We strongly recommend quantifying photosynthetical activity and validate the observations here on the physical processes influencing the CO_2 flux dynamics in Porce III reservoir.

4. Chapter 4: Rainfall as a driver for near-surface turbulence and air-water gas exchange in aquatic systems

4.1. Introduction

Rainfall plays a fundamental role in the biosphere, e.g., in climate, hydrological, and biogeochemical cycles (Schlesinger & Bernhardt, 2013; Winter, 2004). On water surfaces, rainfall also causes physical impacts (Rooney et al., 2018) that affect, among other processes, the gas exchange across the air-water interface in marine (Turk et al., 2010) and in inland waters (Guérin et al., 2007a; Ojala et al., 2011). The air-water gas exchange has important implications for aquatic ecosystems and global biogeochemical cycles of climate-relevant gases (Ho et al., 2018; Raymond et al., 2013), e.g., in regulating the CO_2 uptake of the ocean and the greenhouse gas emissions from inland waters (J. Cole & Caraco, 1998a; Zappa et al., 2009). Currently, the prediction of gas exchange rates and their dependence on variable and dynamic environmental conditions are among the major uncertainties in existing models and the interpretation of empirical data (Harrison & Veron, 2017; Rantakari et al., 2015).

The transport of gases across an air-water interface is commonly described as a diffusive flux that can be parameterized as the product of the gas transfer velocity (k) and the difference between dissolved gas concentration at the water surface and the atmospheric equilibrium concentration. The magnitude of k is related to near-surface turbulence at the water side of the interface (Katul & Liu, 2017; Lamont & Scott, 1970) and controlled by different hydrodynamic forcing mechanisms, most of them hydrometeorological (Guseva et al., 2021; Zappa et al., 2007). Traditionally, k has been estimated as a function of wind speed through empirical models (J. Cole & Caraco, 1998a; Ho et al., 2007; Wanninkhof, 1992), and surface buoyancy flux during convective cooling (Poindexter et al., 2016; Read et al., 2012). Other processes that affect the exchange of gases and near-surface turbulence, such as rainfall, are mostly overlooked, although they may play an important role in gas exchange (Turk et al., 2010).

At the mechanistic level, the eddy cell model for surface renewal proposed by (Lamont & Scott, 1970), referred to as the surface renewal model throughout the manuscript, has provided a scaling relationship for gas transfer velocity based on near-surface turbulence, which led to a universal relationship between the gas transfer velocity and the dissipation rate of turbulent kinetic energy near the water surface (Katul & Liu, 2017; Lorke & Peeters, 2006). The surface renewal model has been validated for a wide range of environmental forcing conditions (Zappa et al., 2007).

Field studies in lakes and reservoirs located at different latitudes have shown that rainfall events can greatly impact the gas transfer velocity (Guérin et al., 2007a; Ojala et al., 2011). Laboratory studies have found that rainfall significantly increases (by a factor of 3 to 40) air-water gas exchange, particularly at low to moderate wind speeds (Banks et al., 1984; Belanger & Korzun, 1990; Harrison et al., 2012; Ho et al., 1997, 2000, 2004, 2007; Zappa et al., 2009). There is a consensus that gas exchange at the water-atmosphere interface is significantly affected by rainfall. Intuitively, turbulence is believed to be responsible for this effect (Banks et al., 1984; Zappa et al., 2009), and growing evidence suggests that rainfall significantly increases near-surface turbulence in marine (Belanger & Korzun, 1990; Ho et al., 2004; Zappa et al., 2009) and freshwater (Harrison et al., 2012) environments. However, the few studies that have investigated this further reported contrasting results. (Belanger & Korzun, 1990) attributed 80% of the reaeration during a rainfall event to turbulence, while (Ho et al., 2000) concluded that turbulence is the main mechanism affecting k during rainfall events without having direct observations of turbulence. Conversely, other studies have found no significant contribution of rainfall to measured dissipation rates of turbulent kinetic energy (Beyá et al., 2011; Peirson et al., 2013). The remaining studies found that rainfall enhances near-surface turbulence, but the turbulence was independent of the rain rate under the investigated experimental conditions (Harrison & Veron, 2017; Zappa et al., 2009). Based on the above results, it has been challenging to establish a consistent relationship between turbulence and rain rate that can be applied in biogeochemical models. Additionally, more emphasis has been given to high rainfall rates (24-190 mm h^{-1}

(Beyá et al., 2011; Harrison et al., 2012; Harrison & Veron, 2017; Peirson et al., 2013; Zappa et al., 2009), overlooking low to moderate rainfall intensities (rainfall rate < 25 mm h^{-1}) which tend to occur more frequently. There is also a bias towards marine environments, in situ or with artificial seawater under laboratory conditions; rain-induced turbulence at the surface of freshwater has rarely been investigated (Harrison et al., 2012).

The influence of rainfall on gas exchange has also been found to become negligible at high wind speeds (Harrison et al., 2012), making assessments of the effect of rainfall in isolation less relevant in regions with high wind speeds. However, in regions where wind speeds are typically low, such as the tropics (Harrison et al., 2012; Turk et al., 2010), or in small lakes and reservoirs, the rainfall can be a more important driver of gas exchange, as almost any rain rate can significantly contribute to the gas exchange under low wind conditions ($U_{10} < 5$ m s^{-1}) (Harrison et al., 2012). When using rain rate as a scaling parameter, a major source of uncertainty comes from the distribution and heterogeneity of raindrop sizes and fall velocities. The assessment of such heterogeneity in both laboratory and environmental conditions requires complex and extensive measurements (Zappa et al., 2009). Depending on drop size, raindrops reach their terminal fall velocity after a free-fall distance of ~20 m (Serio et al., 2019), which challenges laboratory setups. As it was shown that rain-induced air-water gas transfer also correlates with the kinetic energy flux of the rain (Ho et al., 1997, 2000, 2004; Zappa et al., 2009), the uncertainties related to drop sizes and fall velocities might be mitigated by this quantity ((Ho et al., 1997).

Rain-induced turbulence has been typically characterized via high-resolution spatial mapping of turbulent flow velocities near the water surface (Harrison & Veron, 2017; Takagaki & Komori, 2014; Zappa et al., 2009), or single-point velocity observations at a fixed depth (Beyá et al., 2011; Harrison et al., 2012; Takagaki & Komori, 2007; Zappa et al., 2009). Spatially-resolved observations of turbulent flow fields are facilitated by particle image velocimetry (PIV) measurements, which have become an affordable, high-resolution technique in laboratory studies due to the advances in camera technology, computer power and the availability of open-source software for processing (Käufer et al., 2021; Thielicke & Sonntag, 2021). However, this technique has mostly remained unexplored in the study of rain-induced turbulence. (Harrison & Veron, 2017) performed PIV measurements to gain physical understanding of rain-induced turbulence. Their setup, however, focused on high rain rates (40, 100, and 190 mm h^{-1}), and thus did not cover the lower end of the wide range of rain rates that occur under environmental conditions.

In this study, we addressed some limitations still present in the quantitative understanding of the effect of rain rate on near-surface turbulence and on the resulting gas transfer velocity in freshwater. We performed controlled laboratory experiments over a wide range of rain rates (7 to 90 mm h^{-1}) and estimated gas transfer velocities from high-resolution measurements of O_2 concentration, while rain-induced turbulence was characterized based on PIV measurements. Based on these measurements, we elucidate empirical and mechanistic relationships between the gas transfer velocity and near-surface turbulence in dependence on the rain rate and kinetic energy flux. The general applicability of the observed relationship between gas transfer velocity and rain intensity is discussed in the context of surface renewal theory and previous empirical studies.

4.2. Methods

4.2.1. Experimental setup

Our experimental setup consisted of a custom-built rain generator, which was mounted ~20 m above a rain-collecting aquarium (Figure 4-1). To exclude the effects of wind and solar radiation, the experiments were conducted in a closed tower (a hose-drying tower of a local fire brigade, Figure S1) whose height (> 20 m) allowed the raindrops to reach their terminal velocity. Before each experimental series, the dissolved oxygen (O_2) concentration in the aquarium water was reduced to about 50% of its atmospheric equilibrium concentration. During experiments with varying rainfall intensity, we observed the reaeration rate of the water using an oxygen mass balance, as well as the turbulent velocity fields near the water surface (Figure 4-1). Additional measurements included rain rates and the size and fall velocity of raindrops.

The rain generator consisted of a frame (1 × 1 × 0.05 m) with a bottom made of a perforated plexiglass plate (3 mm of thickness). The footprint area of the rain generator exceeded the surface area of the aquarium on all sides, ensuring a homogenous distribution of rain at the water surface. The plate had 580 holes with a diameter of 0.8 mm and with regular spacing. The rain rate was varied by i) controlling the water level above the plate, and ii) changing the number and size of open holes in the plate. The rain generator was manually fed with tap water stored at ambient temperature in an open tank. By varying the water level, we modified the frequency of drop formation at each hole, with a higher level resulting in a higher frequency of droplets and a higher overall rain rate. Some holes were closed with adhesive tape and subsequently reopened by piercing the tape with a needle (0.4 mm diameter) or by removing the tape to revert to the original hole size. Open and closed holes were always homogeneously distributed across the plate (Figure S2). During the experiments, we adjusted the number of open holes to target a range of rain rates between 7 and 90 mm h^{-1}, which correspond to the most frequent rain rates observed at a tropical freshwater reservoir, with many occurring at low wind speeds of < 3 m s^{-1} (Figure S3).

4.2.2. Measurements and experiments

The aquarium that received the rainwater had a volume of 125 L (50 × 50 × 50 cm) and was initially filled to a height of ~42 cm. The instrumental setup inside and outside of the aquarium facilitated estimating the gas transfer velocity, turbulent energy dissipation rates in water, and the rain rate (Figure 4-1).

Each experimental series of measurements consisted of a 15 min period without rain, followed by several 15 min runs with constant rain rates (rain periods). During the runs, we maintained the same configuration (size and number of open holes) but varied the water level in the rainfall generator to vary the rain rate among runs. For the following experimental series, the configuration of the plate was changed, and the procedure was repeated. Rain rates (R in mm h^{-1}) were estimated for each run as the mean rate of change of the water level in the aquarium, which was monitored using a high-resolution pressure probe (Duet, RBR Inc., sampling at 16 Hz with 0.2 mm of depth resolution). Examples of time series of RBR pressures are shown in Figure S4.

For estimating gas transfer velocities, we monitored the dissolved oxygen concentration in water with four fiber-optic sensors (FireStingO2, PyroScience GmbH), distributed vertically at 3, 13, 23 and 33 cm depth from the water surface. The sensors recorded time series at

1 Hz frequency during the 15 min duration of each experimental run. The water temperature and atmospheric pressure (P_{atm}) were measured at the same frequency. As the biological activity may affect the oxygen balance, we used tap water and carefully checked the results of the no-rain periods to discard possible biological activity increasing or decreasing dissolved oxygen. As the oxygen in water was mostly constant during no rain periods, and it only increased when the rain started (Figure S5), it was assumed that biological activity, if present, was low and negligible in the context of our mass balance and the short duration of the experimental runs (see section 2.4). The water temperature varied between experimental series (from 8.4 to 18.5°C) but remained relatively constant during the individual runs (Table 4-1).

To visualize the turbulent flow field, seeding particles (polyamid, 20 µm diameter) were added to the water in the aquarium and illuminated with a continuous-wave laser light sheet. We used a green (532 nm), continuous-wave line laser (450 mW; Inline HP, MediaLas Electronics GmbH) to illuminate a vertical plane in the center of the aquarium. The dynamic distribution of the light scattering seeding particles was observed by recording videos with a consumer-grade camera (GoPro Hero4, GoPro Inc.) located at ~13 cm from the front face of the aquarium, with a frame rate of 30 fps (30 Hz of temporal resolution) and a resolution of 1920 × 1080 pixels. Processing details are given in the section 2.5. The field of view covered an area of 21 × 8 cm below the water surface and a portion of the air side of 3.5 cm height (Figure 4-1 and Figure S6). Videos for Particle Image Velocimetry (PIV) measurements were performed for 3 min during each run. Additional videos were made without rain at the beginning of each experimental series, to characterize background turbulence levels. For metric calibration of the videos, a short (~3 s) video was recorded prior to each series while placing a calibration target (0.5 × 0.5 cm checkerboard pattern) in the laser light sheet. Simultaneously to the PIV videos, single-point measurements of 3-dimensional flow velocities were carried out with an acoustic Doppler velocimeter (ADV; Vector, Nortek A/S) sampling at 32 Hz. The ADV instrument was placed in the aquarium upside-down with the center of the acoustic sampling volume (~ 15 mm diameter and 14 mm length) located at 3 cm depth. The ADV velocity range was set to 0.3 m s^{-1}, ensuring the resolution of vertical and horizontal velocities up to 0.23 and 0.81 m s^{-1}, respectively.

The rain rate and gas transfer velocities were estimated for the 15-minute duration of each experimental run (see section 2.4). However, during the 3-minute videos for the turbulence measurements by PIV, the water level increased by a maximum of 4.5 mm (for 90 mm h^{-1}), which represents only 1% of the water column depth, therefore, the vertical axis was fixed at the initial water level and the water level change was neglected for the dissipation rate estimates.

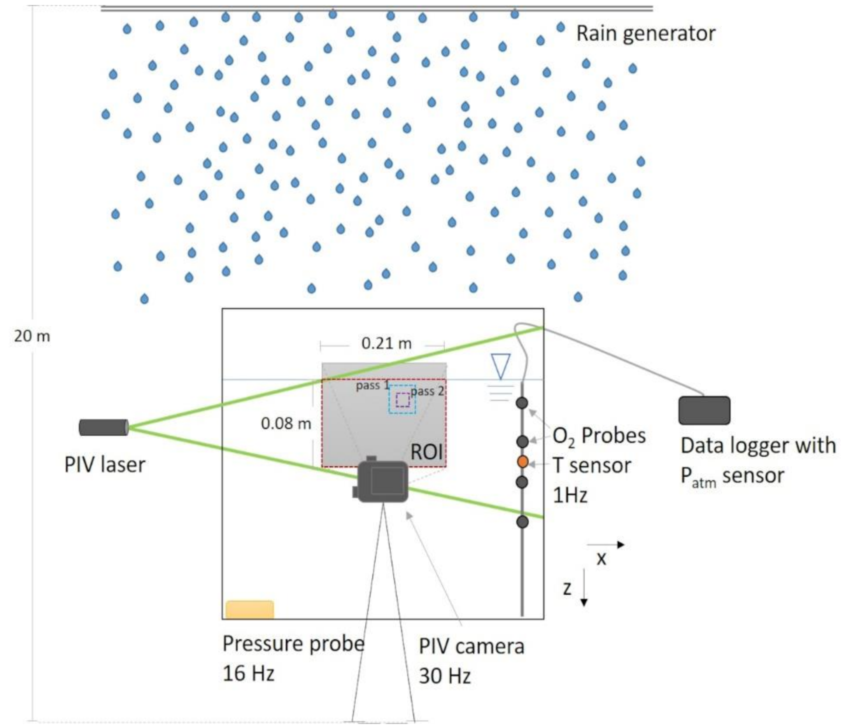

Figure 4-1. Schematic of the set-up and instrumentation used in the experiments (not to scale). The aquarium (0.5 × 0.5 × 0.5 m) was located ~20 m below the rain generator. Particle image velocimetry (PIV) was used to characterize the turbulent flow field in the water. For this, microscopic seeding particles were illuminated from the side using a laser light sheet and observed with a camera through the front window. The field of view of the PIV camera (21 × 12.5 cm on average) is shown as a grey rectangle, the region of interest (ROI) of the PIV measurements (21 × 8 cm on average) is marked by the red dashed line and the size of the interrogation areas is exemplified by blue (pass 1) and purple (pass 2) dashed lines. Four sensors for dissolved oxygen (O_2 probes) were used for establishing an oxygen mass balance in the aquarium to estimate the gas transfer velocity. A pressure sensor located at the bottom of the aquarium was used to estimate the rain rate from the temporal increase in water level. Atmospheric pressure (P_{atm}) was recorded by the oxygen and temperature data logger.

4.2.3. Fall velocity, drop sizes and kinetic energy flux of raindrops

The final fall velocity and sizes of raindrops were estimated by placing a planar light at the location in the aquarium and taking videos of the falling raindrops between the light and the camera (backlight illumination). The videos were recorded with a Sony RX100 IV camera at a frame rate of 1000 fps and a resolution of 1920 × 1080 pixels. A short video of a calibration target was recorded using the same settings. For estimating fall velocity, the recorded videos were first overlaid to the image of the calibration target and the number of consecutive frames in which individual drops could be observed were counted alongside the vertical distance they travelled. Estimates of drop sizes were only performed for a plate configuration with open holes of 0.8 mm. For drops generated using syringe needles (diameters of 0.4 mm), we expected that the resulting drop sizes were comparable to those under the configuration with the pierced tape in the plate (Takagaki & Komori, 2007) (see section 3.4). To validate the observed fall velocities, the measured drop sizes were used to estimate the drop's terminal velocity using the established model by van Boxel (1998).

The kinetic energy flux of the rain (F_{KE}, in J m^{-2} s^{-1}) was calculated according to the expression proposed by (Ho et al., 1997) as follows:

$$F_{KE} = \frac{1}{2}\rho R V^2 \tag{4-1}$$

where ρ is the water density, V is the average fall velocity of the drops and R is rain rate (converted to m s^{-1}).

4.2.4. Gas transfer velocity

Estimates of the gas transfer velocity of oxygen (k_{O_2}) were obtained from dissolved oxygen (O_2) profiles, following a mass balance approach. The total rate of change of dissolved oxygen concentration in the aquarium was equated to the sum of the diffusive flux at the water surface (F_{dif}) and the oxygen flux from rain (F_{rain}). Solving for the diffusive flux as follows:

$$F_{dif} = F_{total} - F_{rain} \tag{4-2}$$

We assumed a horizontally homogeneous distribution of oxygen in the receiving tank, since the only significant forcing present during the experiments was the rain. The total flux (F_{total}, in mmol m^2 d^{-1}) was calculated for each run from the depth-integrated rate of change of O_2 concentration observed by the four probes as follows:

$$F_{total} = \sum_{i=1}^{4} \frac{dC_i}{dt} \Delta h_i \tag{4-3}$$

where $\frac{dC_i}{dt}$ is the mean rate of change of dissolved O_2 concentration measured by each O_2 probe (in µmol L^{-1} d^{-1}) and Δh_i is the representative layer thickness for each sampling depth (in m). The oxygen probes were fixed with respect to the bottom of the aquarium and the inflow of rainwater raised the thickness of the upper layer. Therefore, Δh_i was constant for all the probes, except the upper one, for which Δh_i changed with time according to the rainfall rate.

We assumed that the rainwater is saturated with oxygen at the same temperature as the aquarium water after being at rest for several hours and open to the atmosphere, then the oxygen flux associated with rain (F_{rain}, in mmol m^2 d^{-1}) in the aquarium was as follows:

$$F_{rain} = RC_{eq} \tag{4-4}$$

where C_{eq} is the O_2 concentration in equilibrium with the atmosphere at given water temperature (in mmol L^{-1}) (Chapra, 1997), and R was converted to volumetric units (mm h^{-1} = L h^{-1}).

The gas transfer velocity of oxygen at in-situ temperature (k_{O_2}, in m d^{-1}) was estimated using Fick’s first Law as follows:

$$k_{O_2} = \frac{F_{dif}}{(C_w - C_{eq})} \qquad (4\text{-}5)$$

where C_w is the temporarily averaged O_2 concentration measured by the uppermost sensor (in mmol L^{-1}). k_{O_2} was normalized to k_{600}, the gas transfer velocity of CO_2 at 20°C as follows:

$$k_{600} = k_{O_2}\left(\frac{600}{Sc_{O_2,T}}\right)^{-\mathrm{n}} \qquad (4\text{-}6)$$

where Sc_{O_2} is the temperature-dependent Schmidt number of oxygen (calculated following (Raymond et al., 2012) ($Sc_{O_2} = v/D_{O2}$, with v being the viscosity of water and D_{O2} the diffusion coefficient of oxygen in water). We used the recommended exponent for wavy surfaces ($n = 0.5$) (Jähne et al., 1987).

4.2.5. Particle image velocimetry

We extracted frame sequences (in bitmap format) from each video that were subsequently converted to greyscale images. The pre-processing of the image sequences and PIV analyses were performed using the open source program PIVlab (v. 2.50) (Thielicke & Sonntag, 2021; Thielicke & Stamhuis, 2014). The imported images were first preprocessed to increase and to homogenize the contrast and sharpness of the laser-illuminated seeding particles, and to remove the image background. The region of interest (ROI) for PIV analysis was selected just below the craters formed by the rain drops to the maximum resolved depth (Figure 4-1Figure 4-1 and Figure S6). One frame of the calibration video was used for conversion from pixels to metric units, with pixel size varying between 0.11 and 0.13 mm among experimental series. The images were corrected for lens distortion and calibrated in Matlab 2019a using the Single Camera Calibrator App (reprojection error between 0.47 and 0.98 px). Discrete Fourier Transform correlation with multiple passes and deforming windows was used for PIV processing and two passes with 50% step size were applied, starting with an interrogation area of 128 × 128 pixels and decreased to 64 × 64 pixels. Subpixel estimation was done using a Gaussian 2.3-point fit. The final spatial resolution of velocity vectors was 3.9 ± 0.2 mm.

Based on the results obtained by (Thielicke, 2014) and to be conservative, we consider 0.1 pixel accuracy (1.3×10^{-5} m) in accordance with (Harrison & Veron, 2017), which translated into velocities of 4×10^{-7} m s^{-1} for a temporal resolution of 30 s^{-1} and 1 pixel being 0.00012 m (see details of the estimated accuracy of the PIV measurements in SI).

We used a standard deviation filter with a threshold of a factor of eight, as well as a local median filter with a threshold of 3 for removing velocity outliers and interpolated missing data after filtering. PIVlab uses a boundary value solver for interpolation, which was originally developed for reconstructing images with missing information. The approach provides an interpolation that is generally smooth, and over larger regions with missing data, it will tend towards the average of the boundary velocities, which prevents overshooting (D'Errico, 2012).

The PIV analysis provided two-dimensional velocity distributions with 3.9 mm spacing for *n* ~5400-time steps (corresponding to the total number of frames in each video of ~3 min duration and recorded at 30 fps). The two resolved velocity components (horizontal velocity u and vertical w) were despiked using a modified phase-space method (Goring & Nikora, 2002). Mean values of the velocity components ($\bar{u}$ and $\bar{w}$) were calculated as the time-average for each cell of the velocity fields (in m s^{-1}). Turbulent velocity fluctuations were calculated based on Reynolds decomposition by subtracting the mean velocities from the instantaneous flow velocities as follows:

$$u' = u - \bar{u} \tag{4-7}$$

$$w' = w - \bar{w} \tag{4-8}$$

4.2.6. Dissipation rates of turbulent kinetic energy

Viscous dissipation rates of turbulent kinetic energy (ϵ) result from velocity gradients along all three spatial dimensions. We used a “direct” estimate of the dissipation rates (“PIV_dir”) from the four components of the velocity gradients that are resolved in two-dimensional PIV measurements. According to the expression in (Doron et al., 2001), turbulent dissipation rates were calculated (in W kg^{-1} or m^2 s^{-3}) as follows:

$$\epsilon = 3v\left[\left(\frac{\partial u'}{\partial x}\right)^2 + \left(\frac{\partial w'}{\partial z}\right)^2 + \left(\frac{\partial u'}{\partial z}\right)^2 + \left(\frac{\partial w'}{\partial x}\right)^2 + 2\left(\frac{\partial u'}{\partial z}\frac{\partial w'}{\partial x}\right) + \frac{2}{3}\left(\frac{\partial u'}{\partial x}\frac{\partial w'}{\partial z}\right)\right] \quad (4\text{-}9)$$

where *x* and *y* denote horizontal (*u*) and vertical (*w*) coordinates, respectively. Kinematic viscosity (v) was in m^2 s^{-1}. Time-average values of the two-dimensional distributions of dissipation rates (ϵ_{t_avg}) were calculated as averages of log-transformed values (Baker & Gibson, 1987) for all rain experiments. Finally, dissipation rates were log-averaged horizontally to obtain a mean vertical profile of the turbulent dissipation rate (ϵ_z) for each run.

Turbulent energy dissipation rates were additionally estimated by the inertial subrange method (ϵ_{spec}) using velocity time series measured by PIV (“PIV_spec”) and by the ADV. The approach is based on the assumptions of isotropy and fully developed turbulence, for which the wavenumber spectrum of the turbulent velocity fluctuations follows a universal form (Bluteau et al., 2011):

$$S = \alpha\ \frac{18}{55}\epsilon_{spec}{}^{2/3}\kappa^{-5/3} \quad (4\text{-}10)$$

where S (in (m s^{-1})^2 (rad m^{-1})$^{-1}$) is the one-dimensional wavenumber spectrum of the turbulent velocity fluctuations, α is taken to be 1.5 × 4/3 (factor for the vertical direction), and κ is the wavenumber (frequency divided by mean velocity). The wavenumber spectra (PIV_spec) were estimated for each run at 3 cm depth to be consistent with ADV results.

4.2.1. Scaling of rain-induced gas transfer

As near-surface dissipation rate from wind shear stress have been shown to follow a universal power-law decline with increasing depth (Wüest & Lorke, 2003), we tested a power-law approach for describing the vertical attenuation of rain-generated turbulence:

$$\epsilon_z = a\,(R) z^{-b} \tag{4-11}$$

where ϵ_z can be estimated for any water depth z below the viscous sublayer at the water surface. For all runs, dissipation rate profiles were fitted to equation (4-11) to obtain a common exponent b, and a function that describes the dependence of the coefficient a on the rain rate (R). Thus, an empirical function $\epsilon_{Rain} = f(z, R)$ was obtained with ϵ_{Rain} in W kg^{-1}, z in m and R in mm h^{-1}.

In order to explore a mechanistic approach for modeling the gas transfer velocity (k, in m s^{-1}) in response to rain-induced turbulence, the above scaling of the turbulent dissipation rate as a function of the rain rate was combined with the surface renewal model (equation (4-12); (Lamont & Scott, 1970) as follows:

$$k = A\,Sc^{-\mathrm{n}}(\epsilon v)^{0.25} \tag{4-12}$$

To estimate the dimensionless empirical coefficient A, linear regressions were made between the estimated values of k_{600} and the expression $600^{-\mathrm{n}}(\epsilon v)^{0.25}$. The regressions were made for dissipation rates measured at the same depth, which we obtained by interpolation of the mean vertical profiles (ϵ_z) between 0.5 to 7.5 cm depth and with a vertical resolution of 0.5 cm. Interpolated profiles were computed for the rain periods and the dissipation rates resulting from rain (ϵ_{Rain}) were estimated. Then, we analyzed the dependence of the gas transfer velocity on rain rate (R) and obtained 15 linear regressions corresponding to different depths at which dissipation rates were measured (z_1 = 0.5 cm, z_2 = 1.0 cm,… z_{15} = 7.5 cm). The quality of the correlations was assessed using the coefficient of determination (r^2), and the best correlation was selected for the final model (k_{600_mod}) by replacing ϵ in equation (4-12) by the function $\epsilon_{Rain} = f(z, R)$.

4.3. Results

4.3.1. Overview

The different configurations of the rain generator resulted in rain rates between 6.9 and 88.9 mm h^{-1}, (Table 4-1). Both k_{600} and dissipation rates obtained at a rain rate of 16.0 mm h^{-1} presented outliers in all subsequent analyses (Table 4-1). This run was excluded from the following analyses of dissipation rates and from k_{600} analysis.

Table 4-1. Summary of experimental results. R is the rain rate, T is the water temperature and Sc_{O_2} is the Schmidt number of oxygen at temperature T. ϵ_{Rain} is the rain-induced turbulent dissipation rate from the PIV estimated at 7.5 cm depth. k_{600} and k_{600_mod} are the estimated (Eq. (4-6)) and modelled (Eq. (4-14)) gas transfer velocities, respectively. F_{KE} is the estimated kinetic energy flux of rain.

Run	R [mm h^{-1}]	T [°C]	Sc_{O_2}	ϵ_{Rain} [W kg^{-1}]	k_{600} [cm h^{-1}]	k_{600_mod} [cm h^{-1}]	F_{KE} [W m^{-2}]
1	6.90	16.9 ± 0.054	623	3.10×10^{-8}	2.44	11.6	0.0779
2	8.05	17.1 ± 0.055	615	3.76×10^{-8}	6.43	12.4	0.0905
3	10.3	9.48 ± 0.030	927	3.09×10^{-8}	4.69	14.6	0.116
4	13.5	9.35 ± 0.027	933	9.74×10^{-8}	16.2	16.4	0.152
5	16.0	9.13 ± 0.737	945	1.62×10^{-7}*	52.7	17.8	0.180
6	16.2	8.59 ± 0.020	973	1.21×10^{-7}	25.2	20.2	0.237
7	21.1	8.36 ± 0.016	979	9.97×10^{-8}	17.5	17.9	0.182
8	19.8	8.49 ± 0.021	986	9.74×10^{-8}	17.9	19.7	0.222
9	25.0	16.8 ± 0.062	624	9.68×10^{-8}	15.5	20.6	0.281
10	26.0	11.0 ± 0.010	852	1.36×10^{-7}	20.8	21.8	0.293
11	28.8	17.4 ± 0.087	607	9.62×10^{-8}	28.8	21.8	0.323
12	39.4	11.1 ± 0.013	849	3.14×10^{-7}	30.1	26.2	0.443
13	48.9	17.8 ± 0.146	593	2.62×10^{-7}	25.3	27.6	0.550
14	88.9	18.5 ± 0.220	572	3.42×10^{-7}	41.8	35.9	0.999

* marks an outlier that caused the run with 16 mm h^{-1} to be excluded from the subsequent analysis

In the absence of rain, the oxygen concentration in the aquarium did not change significantly and, while significant increases in oxygen concentration were observed with time in the presence of rain (Figure S5). Gas transfer velocities were estimated using equation (4-6) for rain periods (Table 4-1). During all experiments with rain, the dissolved oxygen concentrations increased nearly linearly with time ($r^2 > 0.90$ for most of the measurements, $p<0.0001$), with similar rates at all sampling depths and with increasing slopes for increasing rain rates (Figure S5). The in-situ gas transfer velocity k_{O_2} was strongly correlated with the rain rate ($r^2 = 0.87$) (Figure 4-2a). In contrast, the normalized gas transfer velocity (k_{600}), which ranged from 3.0 to 46.5 cm h^{-1} (Table 4-1), showed a slightly weaker correlation with the rain rate when all data were included ($r^2 = 0.76$) (Figure 4-2b).

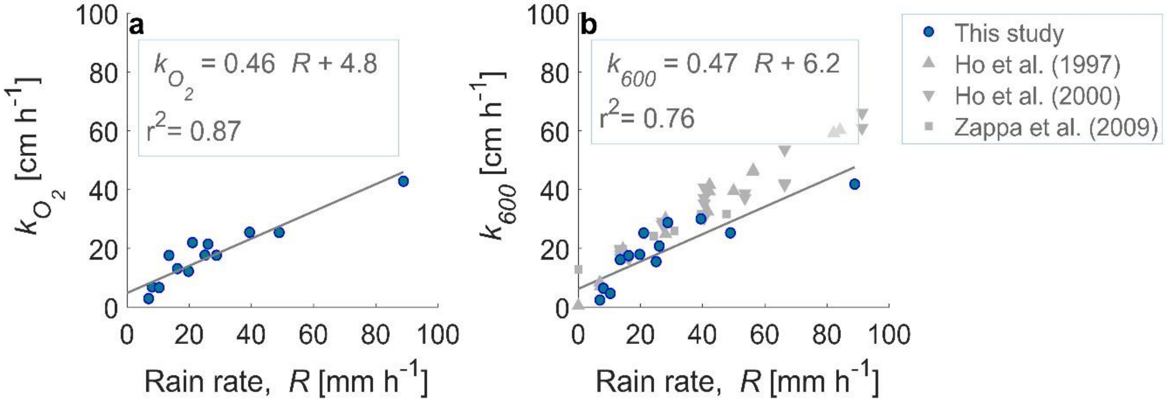

Figure 4-2. Gas transfer velocity versus rain rate (R) with linear regressions (solid lines) and the resulting equations shown as legends. **a**) Gas transfer velocity for oxygen at in situ temperature (k_{O_2}), **b**) Normalized gas transfer velocity (k_{600}) and comparison to previous studies (Ho et al., 1997, 2000; Zappa et al., 2009). The data from (Zappa et al., 2009) were taken from their Figure 9 and fitted with a linear regression to obtain the expression $k_{600} = 0.42R + 13.3$ ($r^2 = 0.97$).

4.3.2. Energy dissipation rates

Time-averaged turbulent dissipation rates (ϵ_{t_avg}) were homogeneously distributed along the horizontal direction but showed strong vertical gradients (Figure S7). They were largest near the water surface and decreased by about two orders of magnitude toward the lower part of the field of view at ~7 cm depth. Higher rain rates were associated with higher energy dissipation rates. Thus, ϵ_{t_avg} varied vertically between ~10^{-5} and ~10^{-7} W kg^{-1} for rain rates $R \leq 25$ mm h^{-1}, and from ~10^{-4} to ~10^{-6} W kg^{-1} for $R > 25$ mm h^{-1} (Figure S8).

The depth dependence of mean turbulent dissipation rates (ϵ_{Rain}) could be well described by power-law functions for all investigated rain rates ($r^2 \geq 0.98$, Figure S8). The exponent b

(equation (4-11)) was relatively constant for all rain rates (*b* = 1.99 ± 0.33 mean ± std.). The coefficient *a* in equation (4-11) was related to the rain rate (R) by a power-law function with an exponent of 1.8 (r^2 = 0.80, Figure 4-3a). Combining both relationships resulted in the following empirical scaling of the dissipation rate (ϵ_{model} in W kg^{-1}) as a function of the rain rate (R in mm h^{-1}) and depth (z in m):

$$\epsilon_{model}(R,z) = 2.28 \times 10^{-12} R^{1.8} z^{-2.0} \tag{4-13}$$

In general, modeled and measured dissipation rates were in good agreement (Figure 4-3b). Particularly the decline of dissipation rates by two orders of magnitude over the top most 7 cm of the water column was consistent and well described by the model. The overall model showed best agreement for moderate rain rates around 30 - 40 mm h^{-1}, while the magnitude of dissipation rates tended to be underestimated for the lowest rain rates (Figure 4-3b).

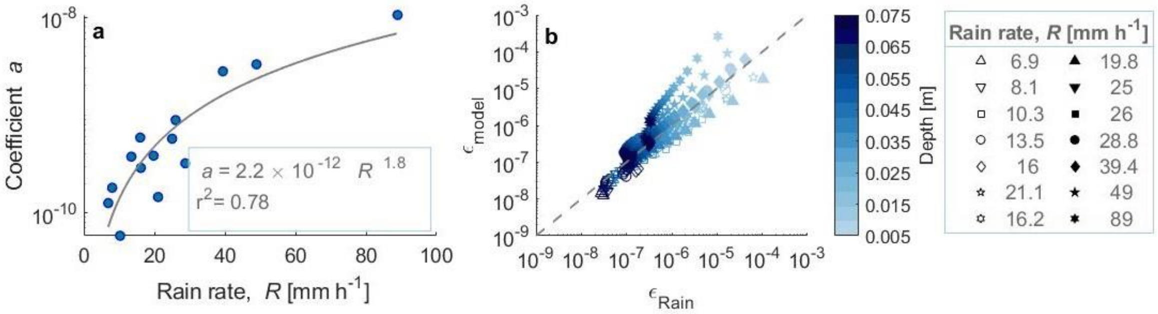

Figure 4-3. Details of the dissipation rate modeling process **a**) Power-law relationship between the coefficient *a* (equation (4-11)) and the rain rate (R) (solid line). **b**) Modeled versus measured dissipation rates for all evaluated rain rates (R) (symbols) and at all evaluated sampling depths (colorbar). The dashed line shows a 1:1 relationship.

The inertial subrange method using the data from the ADV was used to validate the PIV results from the direct method ("PIV_dir") from equation **¡Error! No se encuentra el origen de la referencia.**. ADV dissipation rates (ϵ_{ADV}) ranged from 1.2 × 10^{-8} to 5.2 × 10^{-6}), showing a general consistency with the magnitude of the PIV-based estimates in the rain rate range between 7 and 21 mm h^{-1}. For higher rain rates, the ADV results were about one order of magnitude larger than the ones from the PIV. We additionally estimated the dissipation rates by the inertial subrange method using the PIV results (“PIV_spec”) and the results from both methods (PIV_dir and PIV_spec) were comparable to each other (Table S1).

4.3.3. Scaling of the gas transfer velocity

We compared the normalized gas transfer velocities (k_{600}) observed at different rain rates (n = 14) against those predicted from turbulent dissipation rates by the surface renewal model (equation (4-12)). The empirical coefficient A in the surface renewal model was estimated separately for all sampling depth of dissipation rates by linear regression (Figure S7). The correlations were systematically weaker near the water surface (r^2 ~0.50), and became stronger toward ≥6 cm depth. The best correlation with measured gas transfer velocities were obtained from dissipation rates measured at 7.5 cm depth ($r^2 = 0.52$), with an estimated value of A = 2.43 (Figure 4-4), such that equation (4-14) becomes as follows:

$$k_{600\_mod}[\mathrm{m\ s^{-1}}] = 2.31 \cdot 600^{-0.5}(\epsilon_{model}\nu)^{0.25} \qquad (4\text{-}14)$$

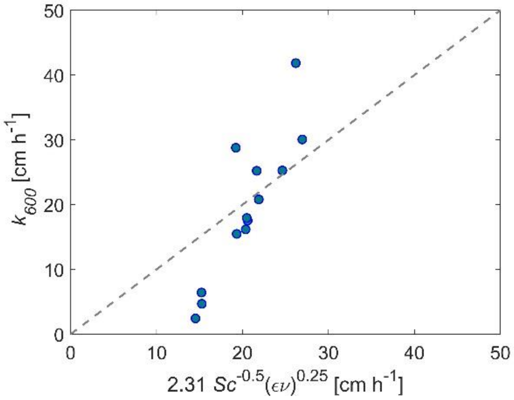

Figure 4-4. Normalized gas transfer velocities k_{600} versus surface renewal model (Equation (13)) for energy dissipation rates sampled at z = 7.5 cm depth. At this depth, we estimated the value of the coefficient A as 2.31, Sc is the Schmidt number (here equal to 600). The dashed line shows a 1:1 relationship.

To relate the gas transfer velocity to rain rate (R), we replaced the measured dissipation rate in the surface renewal model by the function $\epsilon(R,z)$ given in equation (4-13), to obtain a model of k_{600} (in cm $\mathrm{h^{-1}}$) as a function of the rain rate (R in mm $\mathrm{h^{-1}}$) and kinematic viscosity (ν in $\mathrm{m^2\ s^{-1}}$) at 7.5 cm depth as follows:

$$k_{600\_mod}\ [\mathrm{cm\ h^{-1}}] = 152\ R^{0.45} v^{0.25} \qquad (4\text{-}15)$$

Gas transfer velocities modeled from rain rates varied from 11.6 to 35.9 cm h^{-1} (Table 4-1). Good agreement was found when the model (k_{600_mod}) was linearly correlated with all accepted data of the measured k_{600} (Figure 4-5) ($r^2 = 0.85$, $n = 13$, $p < 0.0001$).

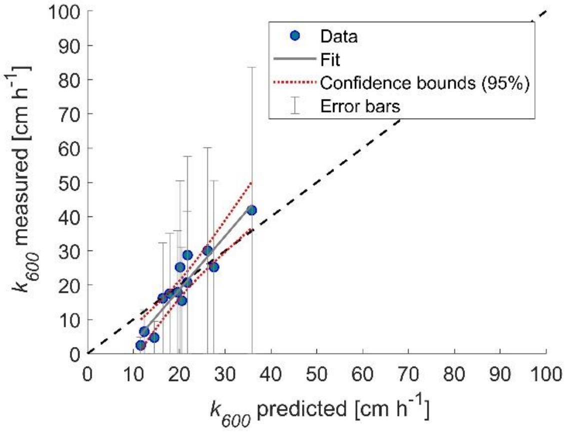

Figure 4-5. Measured (k_{600}) versus predicted (k_{600_mod}) gas transfer velocities (symbols) and a 1:1 plot (dashed line). The slope of a linear regression (grey line) was 1.6 ± 0.18 ($r^2 = 0.85$, $n = 13$, $p < 0.0001$). Error bars represent the uncertainty of factor of 2 in the measured dissipation rates.

4.3.4. Kinetic energy flux

The drop size was estimated to be 5.7 ± 1.1 mm ($n = 103$). Since the drop sizes were only estimated from the configuration with the largest open holes (0.8 mm), it is assumed that according to the needle and droplet diameters measured by (Takagaki & Komori, 2007), droplets of ~2.1 mm diameter were produced all the time by at least 50% of the holes according to the configurations we used in the rain generator. The fall velocity of the raindrops above the water surface was estimated from observations of 6 individual drops to be 8.3 ± 2.5 m s^{-1} (mean ± std.). This velocity was found to be consisted with the model of (van Boxel, 1998). The resulting F_{KE} ranged from 0.078 to 0.999 W m^{-2} from the lowest to the highest rain rate (Table 4-1). For comparison with previous studies, we analyzed the relationship between the normalized gas transfer velocity and the kinetic energy flux by fitting a second order polynomial function to k_{600} as a function of F_{KE} (in W m^{-2}) (Figure 4-6), resulting in:

$$k_{600}\,[\mathrm{cm\ h^{-1}}] = -\,60.4{F_{KE}}^{2} + 98.3F_{KE} + 4.0 \qquad \text{(4-16)}$$

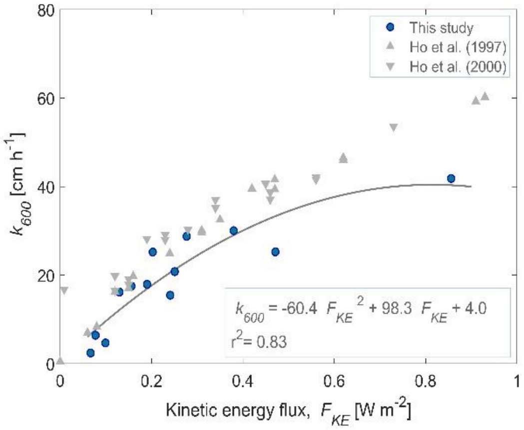

Figure 4-6. Observed gas transfer velocity (k_{600}) versus kinetic energy flux of rain (F_{KE}). The solid line shows a second-order polynomial fit according to the equation provided in the legend. Results from (Ho et al., 1997, 2000). The data from Ho et al. (1997) were taken from their Table 1 and fitted to a polynomial curve to get the expression $k_{600} = -30.6{F_{KE}}^{2} + 91.7F_{KE} + 3.47$ (r^2 = 0.99) (Figure S10). The data from Ho (2000) were taken from Figure 8 in Zappa et al. (2009) and the polynomial curve was fitted to get the expression $k_{600} = -26.9{F_{KE}}^{2} + 84.7F_{KE} + 5.91$ (Figure S11).

4.4. Discussion

4.4.1. Rain-induced near-surface turbulence

Controlled laboratory experiments were performed to characterize rain-induced turbulence in freshwater over a wide range of rain rates. We found a systematic increase in dissipation rates (ϵ_{Rain}) with rain rate (equation (4-13)) that was not previously reported (Beyá et al., 2011; Harrison et al., 2012; Zappa et al., 2009). Our study expanded the range rain rates considered in previous studies, which were mostly limited to testing fewer and mostly high rain rates: 108 and 141 mm h^{-1} (Beyá et al., 2011); 0, 30 and 60 mm h^{-1} (Harrison et al., 2012); 24, 30, 40 and 48 mm h^{-1} (Zappa et al., 2009) to include low to moderate rain (< 25 mm h^{-1}) and a larger amount of observations (14 runs). Those conditions allowed us to obtain a consistent power-law relationship between dissipation rates and rain rate (equation (4-13)).

Turbulent dissipation rates (ϵ) ranged from 3.1 × 10^{-8} to 3.4 × 10^{-7} W kg^{-1} at 7.5 cm depth for rain rates between 7 and 89 mm h^{-1}. In general, these values are three orders of magnitude lower than those reported by Zappa et al. (2009) and one order of magnitude lower than those from (Harrison & Veron, 2017), all being measured within a few centimeters (~ 5 to 8 cm) from the surface and at similar rain rates. In contrast, at 1 cm depth (Harrison & Veron, 2017) observed dissipation rates for a rain rate of 39.4 mm h^{-1} that were in close agreement with our measurements (~ 3 × 10^{-5} W kg^{-1} versus ~1 × 10^{-5} W kg^{-1}, Figure 4-6). At greater depth, our estimates were up to one order of magnitude lower. This comparison with previous measurements may suggest that the dissipation rates were underestimated in our study. One possible reason could be an insufficient resolution of the current shear at the smallest scales of motion by our PIV setup. (Tennekes & Lumley, 1972) showed that almost the entire dissipation takes place at wavenumbers κ for which $\kappa\eta$ < 5, where η is the Kolmogorov microscale of turbulence ($\eta = (\nu^3/\epsilon)^{1/4}$). Given rain-driven dissipations rates between ~ 10^{-8} and ~10^{-6} W kg^{-1}, covering the ranges of the PIV and ADV results, the η varied between 1 and 3 mm. The smallest spatial scale resolved in our measurements was 3.9 mm yielding a wavenumber (κ) of 1611 rad m^{-1}, so the values of $\kappa\eta$ range from 1.6 to 4.8. Following (Siddiqui & Loewen, 2007), we estimated that we resolved about 75% of the total dissipation rate under these conditions. Although this represents a systematic bias of our dissipation estimates, it is small compared to the order of magnitude differences in comparison to previous studies. On the other hand, by applying the inertial subrange method, which has also been used in previous rain studies to determine ϵ (Zappa et al., 2009), we found the dissipation rates from both ADV and PIV-based velocity measurements to be largely comparable (Table S1, Figure 7). ADV-based dissipation estimates were larger for the highest rain rates. These discrepancies are expected because methodological and sampling limitations cause dissipation rates to be generally associated with relatively large uncertainties, and comparisons among different methods often result in agreement within a factor of two (Kocsis et al., 1999). It should be noted that the application of the inertial subrange method to the single-point ADV velocity measurements in our experiment is rather questionable, because of the general lack a uniform mean flow, which is required for converting frequency to wavenumber spectra (Bluteau et al., 2011).

As a most likely reason for the comparably low dissipation rates generated by rain in our study, we note that earlier studies were carried out in the presence of other turbulence sources such as currents and artificially generated waves, which might become dominant over rain-generated turbulence, whereas we studied the effect of rain in isolation. We therefore consider the resulting relationship between dissipation rate and rain rate as being applicable under rainy and low wind conditions.

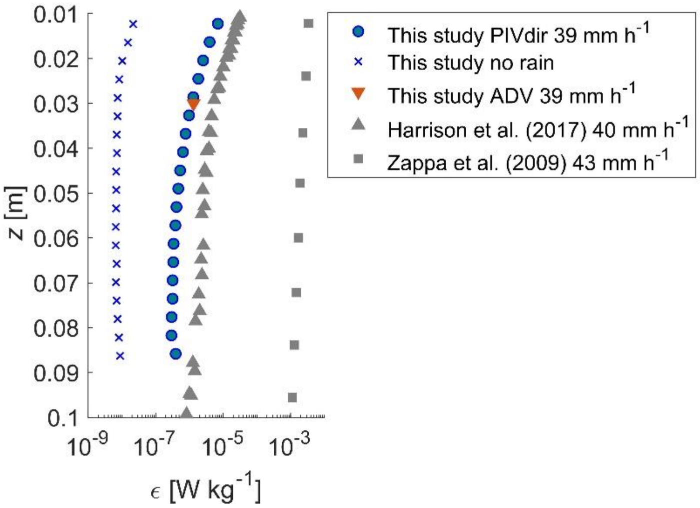

Figure 7. Comparison of dissipation rate profiles estimated by different methods in the present study, and estimated in other studies for similar rain rates: PIV-based dissipation rates (Equation 9) for R=39 mm h^{-1} (blue circles) and in the absence of rain (blue crosses); the single-point dissipation obtained from the ADV data (red triangle); profiles of the first 10 cm obtained by Harrison et al. (2017) at 40 mm h^{-1} (grey triangles) and data from Zappa et al (2009) measured at 43 mm h^{-1} (grey squares).

4.4.2. Scaling of rain-induced gas transfer

Our results clearly show that rainfall enhances the gas transfer velocity, which is in agreement with previous observations (Banks et al., 1984; Harrison et al., 2012; Ho et al., 1997, 2004; Takagaki & Komori, 2007; Zappa et al., 2009). The resulting normalized gas transfer velocities (k_{600}) during rain were mostly within the range reported in previous freshwater studies, which tested rain in isolation from other significant sources of turbulence (Harrison et al., 2012; Ho et al., 1997, 2000). Our data were in the upper range of the transfer velocities obtained by Harrison et al. (2012), which could be related to different fall velocities of the raindrops. The drops generated at 20 m above the aquarium in our study are expected to have reached their terminal velocity (Jones et al., 2010), whereas in (Harrison et al., 2012) the height of the rain simulator above the flume was only 2.6 m, leading to smaller fall velocities around 3.13 m s^{-1}.

Linear regressions of k_{600} and rain rate R showed strong correlations (r^2 = 0.76). However, the oxygen gas transfer velocity (k_{O_2}) correlated better with R than k_{600} (r^2 = 0.87), suggesting additional uncertainty being related to the temperature correction (Schmidt number scaling) of the transfer velocities.

The kinetic energy flux (F_{KE}) proposed by (Ho et al., 1997) as a suitable parameter to explain gas exchange, and that has been used in many subsequent studies (Harrison et al., 2012; Ho et al., 2000, 2004; Zappa et al., 2009), was well correlated with the rain-induced gas transfer velocity. The resulting magnitude of the F_{KE} was similar to the values reported by (Ho et al., 1997) and by (Zappa et al., 2009) (Figure 4-6). Similar to the k_{600} - R correlation results, the polynomial expression found in this study for k_{600} as a function of F_{KE} was strong (r^2 = 0.83), and the data were in agreement with the empirical fits reported in previous studies (Ho et al., 1997, 2000; Zappa et al., 2009) for k_{600} < 30 cm h^{-1} (Figure 4-6).

Mechanistic models of greenhouse gas dynamics and fluxes in aquatic environments are typically based on mass balances, where gas transfer velocities are either obtained from a few solitary measurements, or described as a function of mean wind speed (Donis et al., 2017; Günthel et al., 2019; Santoso et al., 2020). In this study, we present a mechanistic method for describing the rain-induced gas transfer.

In line with (Zappa et al., 2009), we found good agreement between observed gas transfer velocities and predictions by the surface renewal model (Figure 4-4), contributing to the idea of this model as a possibly unified relationship for the air-water interfacial fluxes in response to a range of environmental forcing conditions. However, the large difference between our dissipation rates and values observed by Zappa et al. (2009), result in larger values of the empirical coefficient in the surface renewal model (A), with A = 2.43 (equation (4-12)) being six times larger than the value reported by (Zappa et al., 2007, 2009) (A = 0.42). In a broader evaluation of the coefficient for different wind and density-driven flows, (Esters et al., 2017) reports values between 0.18 and 1.5. Therefore, based on the above values of A, our results appear to be rather high. It is important to consider that despite our robust assessment of the reliability of the range of dissipation rates obtained in this study (see section 4.1), there are still large uncertainties associated with estimates of dissipation rates. Assuming a underestimate by a factor of 2 (Kocsis et al., 1999) in the dissipation rate by the direct method, we found the coefficient A to become ~1.94. An important factor that may also cause a discrepancy in the value of this coefficient throughout the comparison of different studies is the depth at which the dissipation rate is measured. However, this is not likely to be the reason for the discrepancy between the coefficient of (Zappa et al., 2007, 2009) and ours, as the coefficient A = 0.42 was obtained from dissipation measurements made within a few cm of the surface (Zappa et al., 2007) as were we (z = 7.5 cm).

Although the surface renewal model (equation (4-12)) is indicated for the water surface, it is difficult to quantify rain-generated dissipation near the air-water interface, where waves, drop-generated bubbles and other processes interplay (Harrison & Veron, 2017; Zappa et al., 2007). According to (Harrison & Veron, 2017), at the depth of the cavities (z ~ 1 cm), waves may contribute up to 80% of the fluctuating velocity, while the contribution would decrease to less than 20% at z ~ 3 cm. In agreement with those findings, our results showed the best correlation between the dissipation rates and the surface renewal model at 7.5 cm depth instead of closer to the air-water interface.

There are several empirical expressions in the literature for the normalized gas transfer velocity (k_{600}) as a function of the rain rate (R). Some studies proposed the use of the kinetic energy flux (F_{KE}) as the parameter to relate k_{600} with R (Figure 4-6) (Ho et al., 1997). Our results showed that the surface renewal model predicted more of the variability in the rain-generated gas transfer velocity than the kinetic energy flux (r^2 = 0.87 versus r^2= 0.83), in agreement with (Zappa et al., 2009). Other studies have proposed direct relationships between k_{600} and R. For instance, (Ho et al., 2000) found a second-order polynomial fitting and (Guérin et al., 2007a) suggested a linear relationship based on field data. A parametrization of the laboratory data of (Ho et al., 1997, 2000) has been refitted in (Ho et al., 2018) yielding a potential relationship where $k_{600} \propto R^{0.704}$, similar to our mechanistic scaling ($k_{600} \propto R^{0.45}$) based on testing 14 rain rates in the wide range between 7 and 89 mm h^{-1}.

For practical applications, it is a common assumption that the effects of wind and rain at the interface are linearly independent and additive at low wind speeds (Turk et al., 2010). The sum of these contributions can be used as a first-order approximation of the 'total dissipation rate', or it can be used to decide the most suitable scaling relationship (Guseva et al., 2021). Our scaling expands the available tools, by enabling estimates of turbulence and gas exchange in low-wind environments.

4.5. Conclusions

For the first time, our experimental results revealed a positive and systematic relationship between rain rate and turbulence at the air-water interface. Rain-induced dissipation rates of turbulent kinetic energy showed a consistent decrease with increasing sampling depth and a parabolic relationship with rain rate (equation (4-13)). We used this empirical model to derive a relationship quantifying the gas transfer velocity as a function of rain rate. In combination, the observed relationships showed good agreement with the surface renewal model (equation (4-14)), but with a higher value for the associated empirical constant, than those that have been found in former experiments and for other generation mechanisms of near-surface turbulence, including wind.

The application of the obtained scaling relationships for the interpretation of flux measurements and their implementations in numerical models has the potential to further improve the understanding of the importance of rain on the magnitude and dynamics of gas exchange and greenhouse gas emissions from aquatic ecosystems. Our proposed scaling relationships can be used to assess the importance of short-term drivers, such as rain events, on gas dynamics and biogeochemical cycling in marine and inland waters. With readily available data on rainfall as the only additional boundary condition required, future studies can apply the scaling relationships in coupled hydrodynamic and biogeochemical models for a broad range of different aquatic ecosystems and climatic boundary conditions.

An improved understanding of the effect of rainfall on gas exchange is relevant for assessing the role of aquatic ecosystems in greenhouse gas dynamics, such as the emissions of methane, carbon dioxide and nitrous oxide from reservoirs, wetlands and natural lakes. The effect of rain on air-water gas exchange is probably most important in inland waters, especially in wind-sheltered systems, where wind is no longer the dominant driver of near-surface turbulence. Particularly, in the tropics, the rain intensity is the main aspect of seasonal weather changes and low wind speed and high rain intensity and frequency are conditions typically found. Therefore, the consideration of the effect of rain on the gas exchange can have major implications for greenhouse gas budgets, not only in terms of short-term dynamics during rain events but also for explaining seasonal variability of air-water gas exchange in tropical inland waters. We encourage further studies that include other forcing mechanisms besides rainfall, in order to broaden the topic to more conditions occurring in nature.

5. Conclusions and recommendations

Within the framework of this research work, a review was made of the basic concepts surrounding the dynamics of two important greenhouse gases, CO_2 and CH_4, at the surface of lakes and reservoirs. The review included studies carried out from the 1990s to the present, where theories about the origin of GHG emissions in lakes and reservoirs, variables related to the spatial and temporal dynamics of these emissions are discussed.
In principle, the surface dynamics of GHG in reservoirs is given by the interaction of physical and biological variables, which are dynamic in space and time at different scales and are subject to high complexities often related to location. The complexity of the processes and their high variability have made regional and global quantifications, as well as the prediction of emissions from inland waters still have high levels of uncertainty.

It has been widely recognized in the scientific community that tropical reservoirs have a greater potential to emit gases, since biological activity is favored throughout the year by high temperatures. However, studies that have contributed to the understanding of GHG variability in reservoirs have been focused especially on high latitudes such as temperate and boreal zones, and those conducted in tropical zones have mainly covered plain areas in the Brazilian Amazon and savannah. This work focused on contributing to the understanding of GHG surface dynamics in a eutrophic tropical reservoir (Porce III), located in an area of high hydroelectric development in the Colombian Andes, where climatic conditions and seasonality may diverge widely from conditions in previously studied areas.

Data collected in six field campaigns in the Porce III reservoir between May 2017 and February 2019, allowed us to have a broad look at the spatial, seasonal and diurnal dynamics of surface GHGs. Obtaining overestimated results of surface CO_2 concentrations led to limit the analysis, to some extent, to CH_4 dynamics. Spatial patterns showed that the stronger eutrophicated areas of the reservoir may have higher methane emission potential and are microbiologically more active. The results suggested that part of this microbiological activity corresponded to the occurrence of oxic methane production (OMP) at the surface, which is currently under discussion, given the widely dispersed idea that methane is only produced under anaerobic conditions. The reservoir surface showed alternation between surface CH_4 production and consumption during the day, which shows the high complexity that can arise from the interactions between CH_4 drivers and inhibitors under conditions of strong eutrophication. It is recommended that future studies include the measurement of surface methane consumption and production rates, as well as direct measurements of primary production.

In the field campaigns, it was observed that the hydrological condition expressed in the reservoir water level can also be determinant and significant changes were observed, where emissions and surface concentrations of CH_4 were higher at low water levels. In addition to the field campaigns, the seasonal dynamics of surface GHGs in Porce III reservoir was studied through continuous CO_2 monitoring at a fixed point in the reservoir, in several periods of several weeks between 2019 and 2021, near the dam. Although data were not collected for a complete hydrological cycle continuously, seasonal patterns were observed in three different periods of the hydrological cycle: wet-dry transition, dry season, and dry-wet transition. The results showed that, although there were no statistically significant differences, the seasonal pattern showed that, in drier periods, emissions are higher and more variable than in wetter periods. Similar to what was observed for CH_4 in the 2017-2019 field campaigns.

Diurnal dynamics were slightly addressed in the 2017-2019 field campaigns, showing that negative CO_2 flux (from atmosphere to water) are frequently found in the daytime and not at night, indicating that there is a diurnal cycle in CO_2 fluxes highly related to processes with diurnal cycles such as algal photosynthesis-respiration, which makes sense in a eutrophic reservoir, where surface algal content is high in response to nutrient enrichment. However, not all daytime flux results were negative, indicating that bacterial respiration processes, which do not have diurnal cycles, are in constant interaction with the processes of autotrophic organisms and that such interaction results in the alternation of the predominance of photosynthesis or respiration over the course of the day. All these dynamics were observed in detail during the continuous monitoring of CO_2 between 2019-2021, where the diurnal cycle was clearly observed. The diurnal cycle of CO_2 flux showed high variability throughout the day, but the average fluxes showed conclusively that the reservoir tends to be a source of CO_2 most of the time, between 14h and 08h and a sink of CO_2 in the hours of highest solar radiation between 10h and 15h. A coincident diurnal cycle was observed for the buoyancy flux, where cooling consistently occurred at the hours of positive CO_2 flux and viceversa.

Based on the principle that gas exchange at the water-atmosphere interface is the result of the interaction between physical and biochemical factors, and that physical factors translate into the magnitude of turbulence, the possible incidence of two factors widely recognized to affect surface gas transfer were tested: wind speed and buoyancy flux. The magnitude of primary production was not measured, but there is strong evidence from other variables measured in the 2017-2019 field campaigns that Porce III Reservoir remains eutrophic all year. Different buoyancy flux and wind speed conditions were tested to verify their influence on the variability of CO_2 fluxes. However, no scenario showed strong correlations between CO_2 fluxes and buoyant flux or between CO_2 fluxes and wind speed. This allowed inferring that the main factor in the diurnal dynamics of CO_2 fluxes is biological, most likely associated with primary production. However, graphically it was observed that pulses of CO_2 flux coincide with high wind speeds during the afternoon and that the occurrence of these pulses must require the accumulation of CO_2 at the water surface.

Mass balances were calculated to test the origin of the temporal variations (few hours) of CH_4 at the reservoir surface. In this analysis, reactions were also dominant along with CH_4 evasion in the surface CH_4 balance. Importantly, CH_4 showed greater changes during the day than at night, which raises interest about the diurnal cycle of CH_4 and continue to explore the possible relationship of this gas with primary production.

As a highly relevant aspect in studies of GHG emissions from aquatic systems, the gas transfer rate (k_{600}) was evaluated from different perspectives in this research. Direct turbulence measurements with a microstructure profiler and the measurement with floating chambers of CH_4 fluxes at the water-atmosphere interface, as well as surface concentrations of the gas, allowed validating the surface renewal model as a mechanistic model suitable for the Porce III reservoir and determining that, semi-empirical models widely used to estimate k_{600} underestimate the fluxes in the reservoir. Interestingly, it was determined that the obtained empirical proportionality constant A (~1) is larger than typical values reported in the literature. This model may be used by obtaining easily measured variables such as water and air temperature and wind speed, thereby determining the friction velocity, estimating the rate of dissipation of turbulent kinetic energy at 50 cm depth and calculating k_{600} from the surface renewal. The model must be carefully applied in conditions similar to those in which it was obtained: no rain conditions, wind speed (U_{10}) between 0.5 and 7.8 m s^{-1} and at night, in places where convection is weak.

One of the research hypotheses was formulated around rainfall as a factor little studied, but of possible great importance in tropical areas, where rainfall characteristics (frequency and intensity) dominate the seasonal changes of the climatic regime. Relating rainfall to gas exchange in the field is not easy, as flux measurements are typically made under weather conditions that are safe for the team. Laboratory experiments were conducted leading to understanding the influence of rainfall intensity on gas exchange at the water-atmosphere interface. The results revealed, for the first time, a positive systematic relationship between rainfall rate and near-surface turbulence. Again, the surface renewal model was shown to represent the phenomenon well and, consequently, an expression was obtained to relate the gas transfer velocity (k_{600}) to the rain-generated turbulence, expressed in terms of the rain rate. It is highly recommended to verify the experimental results with field data.

This work contributes extensively to the understanding of the surface dynamics of CO_2 and CH_4 in eutrophic tropical reservoirs, as evidence was obtained of the spatial and temporal behavior at seasonal and diurnal scales of GHGs and the use of mechanistic-based gas transfer rate models is proposed.

Appendix A: Supplementary information on Chapter 2

Table S1. Porce river inflow characteristics during the study period: surface temperature (T), electrical conductivity (EC), dissolved oxygen (DO), pH, Ammonia (NH_3^-), nitrites NO_2^-, nitrates (NO_3^-), phosphates PO_4^3 and sulfates (SO_4^-).

Date	*T* [°C]	*EC* [µS cm^{-1}]	*DO* [% sat]	*pH*	NH_3^- [mg L^{-1}]	NO_2^- [mg L^{-1}]	NO_3^- [mg L^{-1}]	PO_4^{3-} [mg L^{-1}]	SO_4^{2-} [mg L^{-1}]
11-May-2017	21.0	300	ND	ND	ND	ND	ND	ND	ND
10-May-2018	22.8	153	54.2	7.3	1.12	0.01	1.44	0.001	283
31-Jul-2018	22.7	137	55.7	7.3	1.68	0.07	2.20	0.085	10.40
18-Sep-2018	22.6	123	56.5	7.4	1.12	0.041	2.709	0.064	848
13-Nov-2018	21.2	84	64.1	7.3	1.12	0.079	2.620	0.106	17.5
26-Feb-2019	25.5	70	107.2	6.9	0.84	0.018	7.92	0.021	6.23

Table S2. Correlations of several variables between Floating (F) versus Dam (D) and Floating (F) versus El Roble (R) weather stations, represented in the subscripts

	Floating (F) vs Dam (D)	Floating (F) vs El Roble (R)
Air temperature, T_{air} (°C)	$T_{air\_F} = 0.868T_{air\_D} + 3.24$ $r^2 = 0.972$	$T_{air\_F} = 0.630T_{air\_R} + 11.1$ $r^2 = 0.760$
Wind speed, U (m s^{-1})	$U_F = 0.401U_D + 1.11$ $r^2 = 0.763$	$U_F = 1.53U_R + 1.22$ $r^2 = 0.314$
Relative humidity, H (%)	$H_F = 32.7H_D^{0.243}$ $r^2 = 0.928$	$H_F = 0.756H_R + 20.8$ $r^2 = 0.798$

Table S3. Wind-based models tested

Model k600 [cm h^{-1}]	**Reference**
$k_{600\_C98} = 2.07 + 0.215{U_{10}}^{1.7}$	(J. Cole & Caraco, 1998a)
$k_{600\_M10} = 0.16 + 2.25U_{10}$	(MacIntyre et al., 2010)
$k_{600\_W14} = 0.251{U_{10}}^2 \times (600/660)$	(Wanninkhof, 2014)

Table S4. Detailed terms of the surface net heat flux calculation

Term	Equations	Details
Net short wave radiation flux	$SW_{net} = SW_{in}(1 - \text{Albedo})$	SW_{in} is the incoming short wave radiation or solar radiation (W m^{-2}), Albedo was assumed to be 0.06, a typical value for water bodies at low latitudes.
Net long wave radiation flux	$LW_{net} = LW_{in} - LW_{out}$ $LW_{in} = Rb_a \sigma E_{air} T_{air}{}^4$ $LW_{out} = \sigma E_w T_w{}^4$ $E_{air} = 0.937 \times 10^{-5}(1 + 0.17C^2)\, T_{air}{}^2$	LW_{in} is the incoming long wave radiation emitted by the atmosphere (W m^{-2}), LW_{out} is the outgoing long wave radiation emitted by the water surface (W m^{-2}), Rb_a is the atmospheric reflection (0.97), σ is the Stefan-Boltzmann coefficient (5.67 x 10^{-8} W K^{-4} m^{-2}), E_{air} is the air emissivity, T_{air} is the air temperature (K), E_w is the water emissivity (0.97), T_w is the water temperature (K) and C is the cloud cover fraction.
Sensible heat flux	$H_{sens} = \rho_{air} C_{air} C_H U (T_w - T_{air})$	ρ_{air} is density of air (kg m^{-3}), C_H is the heat transfer coefficient for sensible heat following the algorithm of (Verburg & Antenucci, 2010) , C_{air} is the specific heat of air (1012 J kg^{-1} K^{-1}), U is the wind velocity (m s^{-1}).
Latent heat flux	$H_{lat} = \rho_{air} L_t C_E U (e_s - e_{air})$ $L_t = 1000\ (2499 - 2.36T_w)$	ρ_{air} is density of air (kg m^{-3}), L_t is the latent heat of vaporization (J kg^{-1}), e_s is the saturation vapor pressure at the water surface, e_{air} vapor pressure in the overlying air, C_E is the transfer coefficient for latent heat following the algorithm of (Verburg & Antenucci, 2010), U is the wind velocity (m s^{-1}).

Table S5. Mean dissipation rates of turbulent kinetic energy (ϵ) and turbulent diffusivity (K_z) for different layers: surface mixed layer (SML), Thermocline (Therm.), Over-plume layer (OPL), river plume (Plume) and Bottom. and for each campaign and sampling point. *Unsuccessful measurements, then K_z was estimated from the average of the successful measurements (same station and layer) or repeated from the last measurement (few hours of difference) (**)

Station	**Layer**	**C2-H-Wet**		**C3-L-Dry**		**C4-L-DWT**		**C5-M-Wet**		**C6-M-Dry**	
		ϵ	K_z	ϵ	K_z	ϵ	K_z	ϵ	K_z	ϵ	K_z
P3	SML	6.5×10^{-8}	4.5×10^{-5}	1.9×10^{-8}	1.3×10^{-5}	3.3×10^{-6}	3.5×10^{-4}	1.3×10^{-7}	4.9×10^{-5}		
	Therm.	1.9×10^{-7}	9.6×10^{-5}	3.5×10^{-8}	2.8×10^{-5}	2.0×10^{-6}	2.6×10^{-4}	1.3×10^{-7}	4.9×10^{-5}		4.9×10^{-5}
	OPL			8.5×10^{-8}	8.1×10^{-5}			9.1×10^{-7}	5.8×10^{-4}		
	Plume	2.5×10^{-7}	1.7×10^{-4}	1.8×10^{-7}	2.1×10^{-4}			3.9×10^{-7}	1.7×10^{-4}		
	Bottom										
P2	SML	2.3×10^{-7}	1.2×10^{-4}	7.3×10^{-7}	9.6×10^{-5}	4.2×10^{-8}	8.1×10^{-5}				
	Therm.	1.7×10^{-8}	3.8×10^{-5}	2.6×10^{-8}	2.6×10^{-5}	2.4×10^{-9}	4.8×10^{-7}	2.3×10^{-8}	1.1×10^{-4}		1.1×10^{-4}
	OPL	9.3×10^{-9}	3.1×10^{-5}	1.8×10^{-9}	2.8×10^{-6}	2.2×10^{-9}	4.8×10^{-6}	1.4×10^{-9}	3.2×10^{-6}		

	Plume			7.8×10^{-9}	1.5×10^{-5}	8.5×10^{-9}	4.8×10^{-5}	3.9×10^{-9}	1.8×10^{-5}		
	Bottom										
P1 - M	SML	1.0×10^{-8}	4.1×10^{-5}	5.2×10^{-9}	1.3×10^{-5}	1.1×10^{-9}	2.9×10^{-6}				
	Therm.	1.2×10^{-9}	1.6×10^{-6}	3.1×10^{-9}	2.2×10^{-6}	5.3×10^{-10}	1.5×10^{-6}		1.6×10^{-6}*		1.6×10^{-6}*
	OPL	9.6×10^{-10}	4.2×10^{-6}	7.7×10^{-10}	2.7×10^{-6}	6.1×10^{-10}	3.8×10^{-6}				
	Plume	1.5×10^{-9}	2.2×10^{-5}	7.9E-10	4.5×10^{-6}	2.2×10^{-9}	1.1×10^{-5}				
	Bottom					3.8×10^{-10}	4.5×10^{-6}				
P1 - T	SML	2.2×10^{-7}	1.4×10^{-4}	4.1×10-8	1.1×10^{-4}	9.7×10^{-8}	1.5×10^{-4}				
	Therm.	2.2×10^{-9}	7.4×10^{-6}	4.6×10-8	1.4×10^{-4}	5.9×10^{-8}	1.2×10^{-4}		5.0×10^{-5}*		5.0×10^{-5}*
	OPL	1.2×10^{-9}	1.3×10^{-5}	6.8×10^{-10}	2.0×10^{-6}	7.5×10^{-10}	2.3×10^{-6}				
	Plume	3.4×10-9	5.1×10-5	8.1×10^{-10}	5.8×10^{-6}	2.2×10^{-9}	1.1×10^{-5}				
	Bottom					3.6×10^{-10}	2.5×10^{-6}				
P1 - N	SML	1.4×10-8	1.3×10-5	2.4×10^{-8}	8.4×10-5	4.0×10^{-8}	1.5×10^{-4}	1.2×10^{-7}	1.3×10^{-4}		
	Therm.	1.0×10-9	2.5×10-6	7.9×10^{-9}	5.7×10-5	1.9×10^{-8}	1.6×10^{-5}	1.1×10^{-7}	4.5×10^{-5}		4.5×10^{-5}
	OPL	9.9×10^{-10}	8.9×10-6	7.6×10^{-10}	2.6×10-6	6.7×10^{-10}	2.4×10^{-6}	4.9×10^{-10}	1.9×10^{-6}		
	Plume	2.9×10-9	4.0×10-5	6.0×10^{-10}	3.9×10-6	2.2×10^{-9}	1.5×10^{-5}	3.9×10^{-10}	4.7×10^{-6}		
	Bottom					4.7×10^{-10}	5.3×10^{-6}				

Table S6. Mean atmospheric fluxes of CO2 (F_{co_2}) and CH4 (F_{cH_4}) observed during chamber measurements and estimated gas transfer velocities during all campaigns and sampling stations: Water surface temperature during chamber deployments (T), fluxes of gases (F), water surface concentrations (C_{w_g}), gas transfer velocity estimated from chambers ($k_{600\_CH_4}$) and resulting from the final model in eq. (10) (k_{600_model}) . N.A. are not accepted data after quality control. *Dissolved CO2 concentrations are potentially overestimated.

	Time	Station	T [°C]	F_{CO_2} [mmol m^{-2} d^{-1}]	$C_{w\_CO_2}$* [µmol L^{-1}]	F_{CH_4} [mmol m^{-2} d^{-1}]	$C_{w_{CH_4}}$ [µmol L^{-1}]	$k_{600\_CH_4}$ [cm h^{-1}]	k_{600_model} [cm h^{-1}]
C1-Wet-HW	15:13	P1	25.0	11.1	469	0.20	0.20	3.67	9.50
	10:05	P2	27.1	45.0	410	0.26	0.26	3.51	9.99
	11:22	P3	24.8	N.A.	312	N.A.	0.23	N.A.	9.53
	14:30	P1	24.0	-12.8	119	0.05	0.26	0.68	13.33
	16:07	P2	25.6	-33.9	337	N.A.	0.34	N.A.	11.45
	8:05	P1	24.2	N.A.	444	0.16	0.24	2.49	7.67
C2-Wet-HW	14:53	P3	26.4	-53.0	757	N.A.	0.17	N.A.	16.09
	12:15	P2	26.2	N.A.	342	N.A.	0.37	N.A.	11.18
	17:10	P1	25.2	15.1	407	1.37	0.32	16.05	13.59
	11:05	P1	25.1	-25.7	519	0.19	2.42	0.28	3.12
	19:50	P1	24.4	37.0	1006	1.00	336.83	0.01	7.61
	2:48	P1	24.6	145.8	670	0.45	0.27	6.10	10.29
C3-Dry-DW	10:29	P3	25.3	-15.2	259	N.A.	0.74	N.A.	7.67
	10:46	P2	26.1	-26.5	44	N.A.	2.64	N.A.	7.58
	12:06	P2	25.5	-36.1	44	N.A.	2.64	N.A.	17.70
	8:13	P1	24.6	8.8	118	2.01	0.86	8.59	7.68
	17:04	P1	24.6	36.3	277	2.36	0.33	27.51	21.45
	22:05	P1	23.6	320.6	369	0.50	0.35	5.52	13.27
C4-DWT-DW	11:18	P3	28.1	N.A.	282	N.A.	1.63	N.A.	6.65
	13:05	P3	25.4	-9.8	249	N.A.	2.43	N.A.	18.59
	10:10	P2	26.7	-27.6	251	N.A.	1.02	N.A.	13.68
	17:00	P1	26.5	-4.8	47	0.80	0.25	11.71	18.26
	9:28	P1	25.3	67.8	365	2.10	0.42	18.71	18.08
	10:33	P1	25.3	26.7	168	2.31	0.42	20.61	13.57
	0:25	P1	25.1	76.6	515	N.A.	0.42	N.A.	11.29
C5-Wet-RW	11:59	P3	26.6	-18.3	277	N.A.	3.02	N.A.	17.54
	14:07	P3	26.3	-25.9	516	N.A.	0.07	N.A.	8.08
	9:33	P2	26.3	8.3	538	N.A.	0.04	N.A.	10.06
	11:35	P2	26.3	-29.0	412	N.A.	0.04	N.A.	12.00
	2:42	P1	24.6	ND	573	N.A.	0.04	N.A.	7.99
	11:02	P1	25.3	-30.2	569	0.81	0.15	20.22	14.99
	15:11	P1	25.2	-15.8	619	0.69	0.14	18.03	13.49
C6-Dry-LW	10:35	P2	26.4	-32.4	240	N.A.	0.58	N.A.	14.89
	16:26	P2	26.0	-16.7	228	N.A.	0.09	N.A.	13.34
	22:49	P1	26.0	26.9	257	0.44	0.09	16.98	9.23
	16:28	P3	25.0	-40.0	956	0.80	369.74	0.01	2.92

10:55	P1	27.8	N.A.	217	0.73	69.27	0.03	1.50
16:20	P1	25.3	N.A.	229	0.91	0.13	27.68	21.86

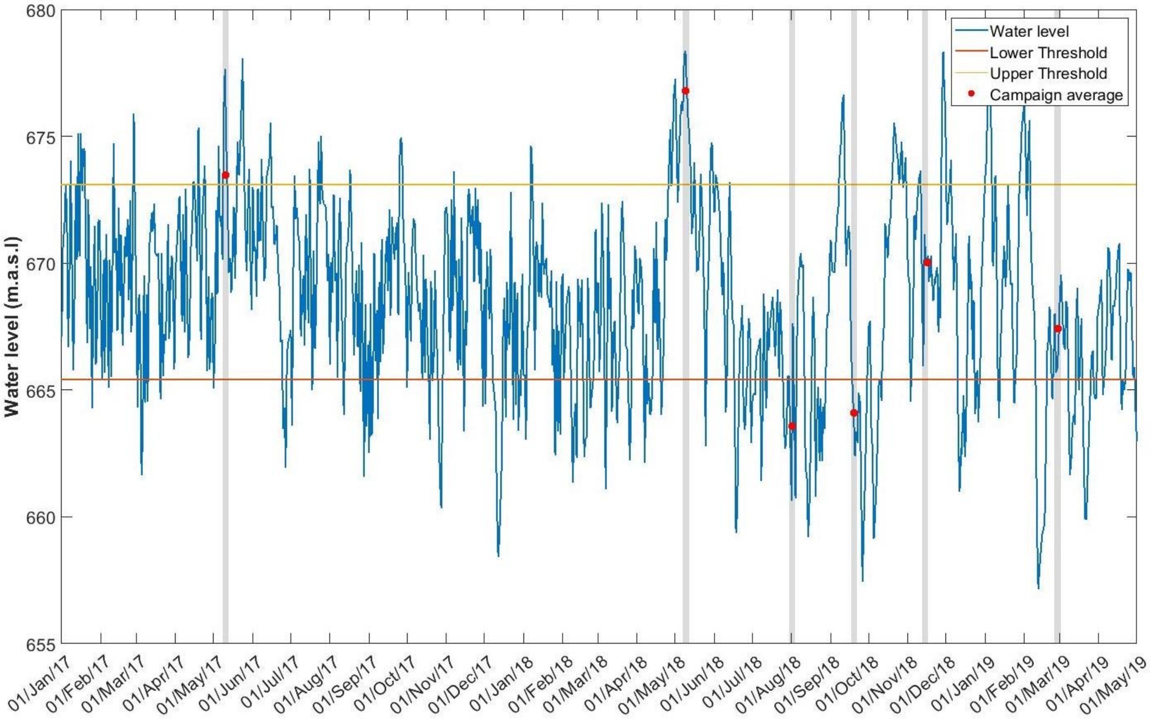

Figure S1. Time series of the water level (1h resolution). Grey shadows represent the field campaigns. Campaigns conducted at a mean water level above the upper threshold (673.1 m.a.s.l., red horizontal line), below the lower threshold (665.4 m.a.s.l., blue horizontal line) or between both thresholds were classified as high level (H), low level (L) or medium level (M), respectively.

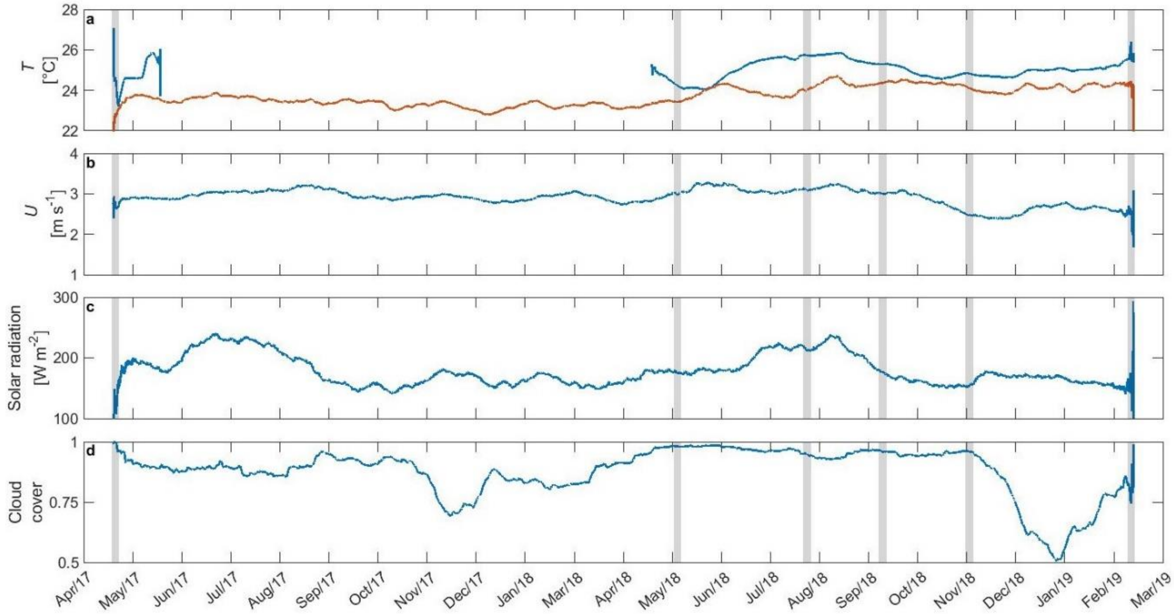

Figure S2. Time series of selected meteorological variables during the study period (moving average over 30 days at 1 hour resolution). **a**. Surface (blue) and air (red) temperature, **b**. wind speed, **c**. solar radiation and **d**. cloud cover fraction

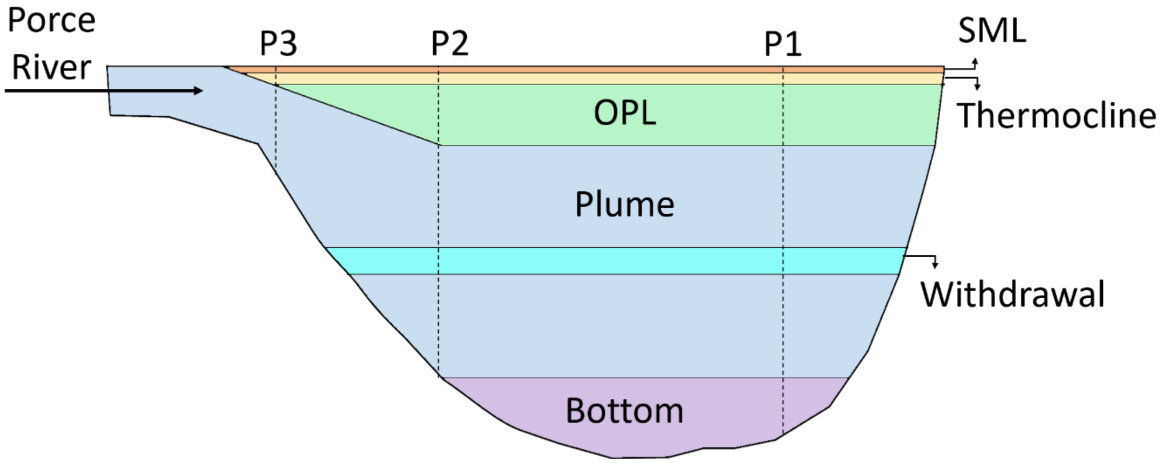

Figure S3. Scheme of a typical vertical structure along a longitudinal cross section of Porce III reservoir, where SML is the surface mixed layer and the OPL is the over-plume layer. Different colors and labels mark layers with distinct physical and physicochemical characteristics. The location of the river inflow, the withdrawal depth at the dam, and of the three sampling sites (P1-P3) are marked by labels. The vertical extent of the different layers during the samplings campaigns is marked in Fig. S5 – S15 and S22 – S25.

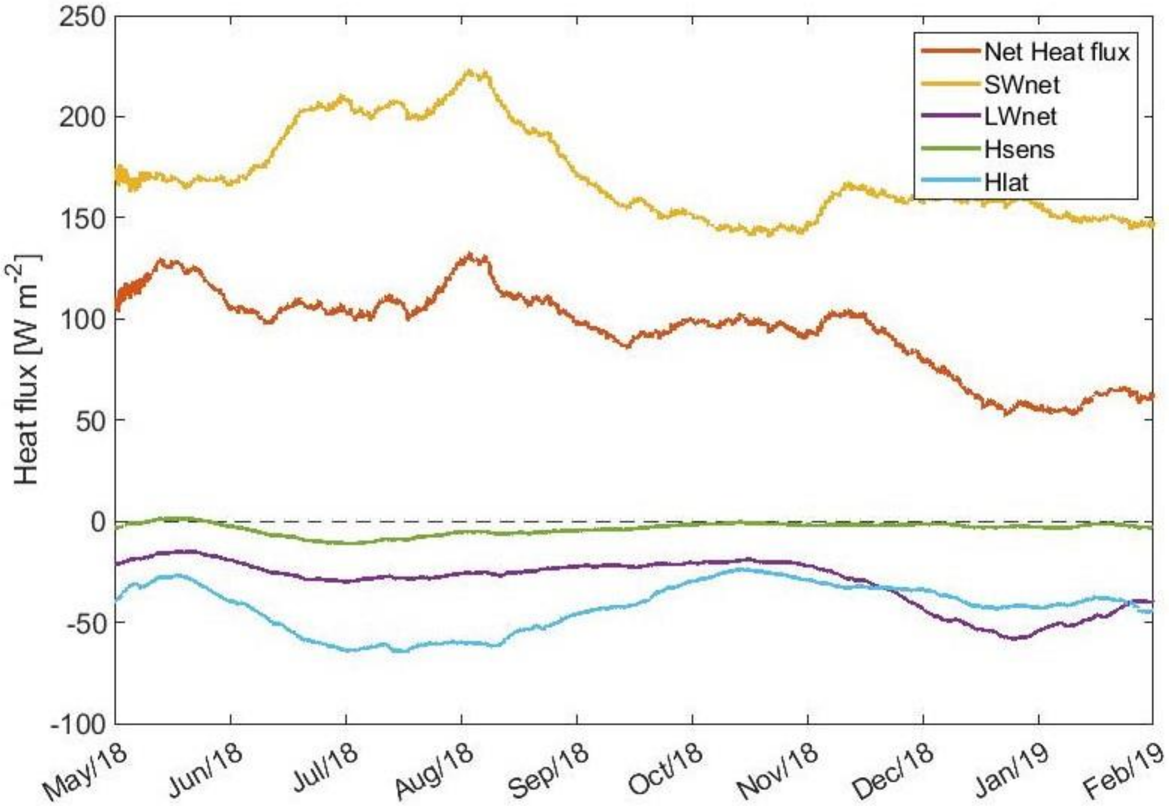

Figure S4. 30-day-moving average of the heat flux components at the water surface (1 h of resolution). The net surface heat flux (red solid line) represents the sum of the net short wave (SWnet) and net long wave (LWnet) radiation fluxes, sensible heat flux (Hsens), and latent heat flux (Hlat). The dashed line mark the zero.

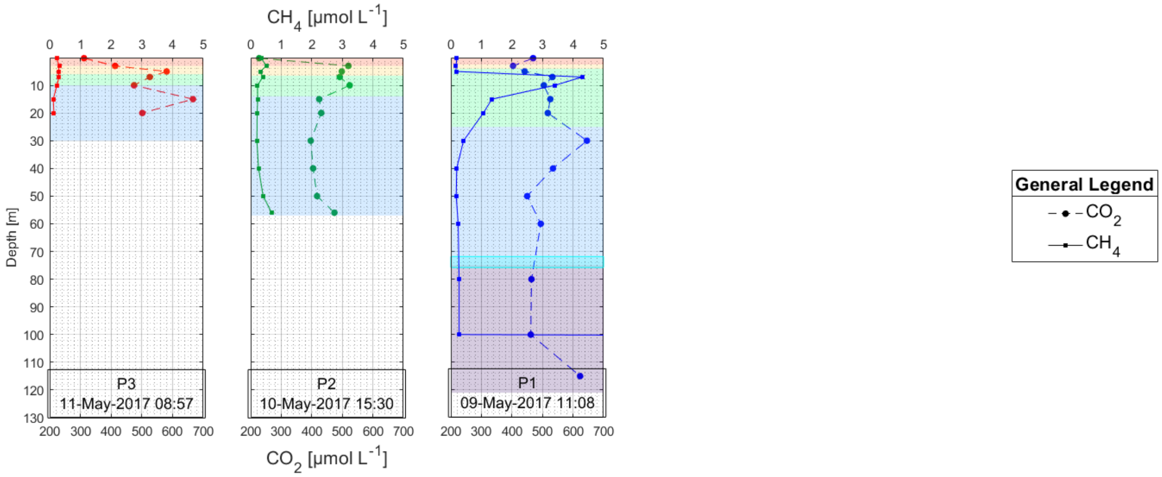

Figure S5. Dissolved CO_2 and CH_4 profiles during C1-H-Wet. The background color represents the layers according to the previously defined conventions (Figure S3). Hidden values: right panel 399 µmol L^{-1} at 115 m depth.

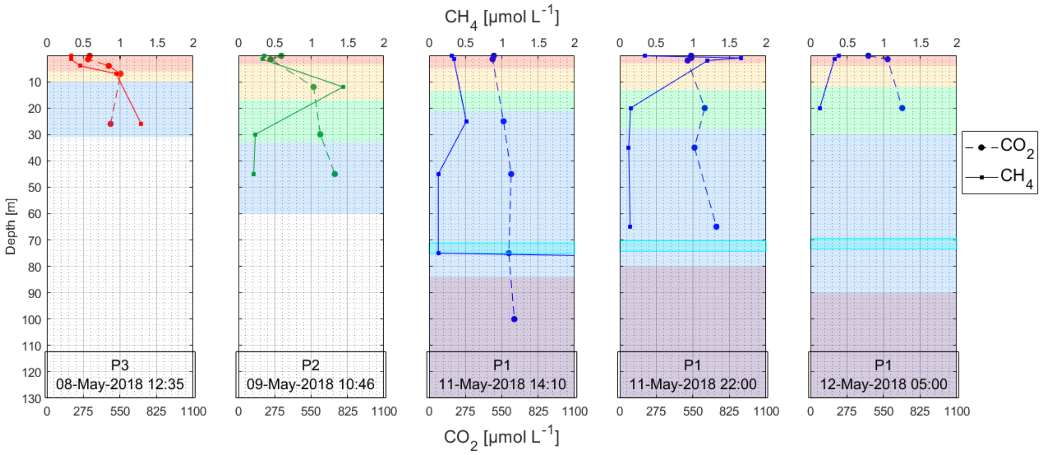

Figure S6. Dissolved CO_2 and CH_4 profiles during C2-H-Wet. The background color represents the layers according to the previously defined conventions (Figure S3). Hidden values: third panel 53.3 µmol L^{-1} at 100 m depth.

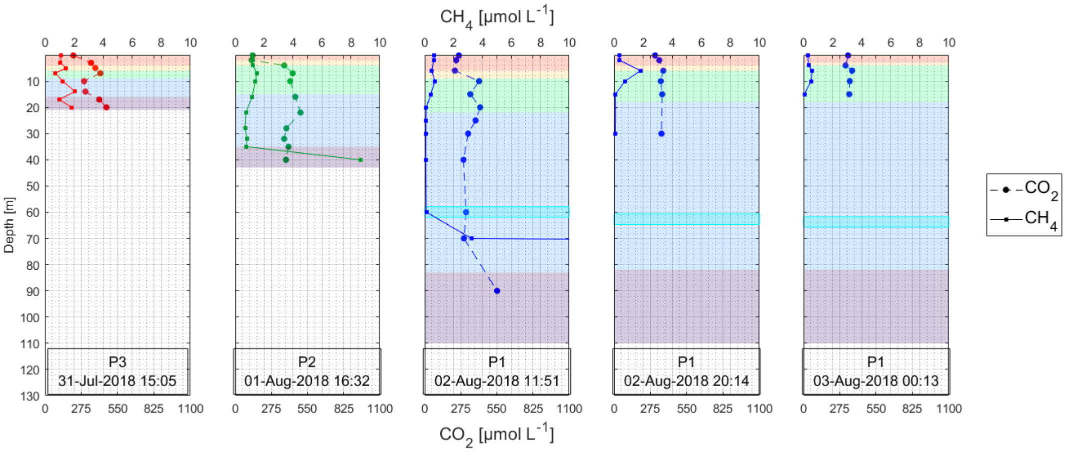

Figure S7. Dissolved CO_2 and CH_4 profiles during C3-L-Dry. The background color represents the layers according to the previously defined conventions (Figure S3). Hidden values: third panel 474 µmol L^{-1} at 90 m depth.

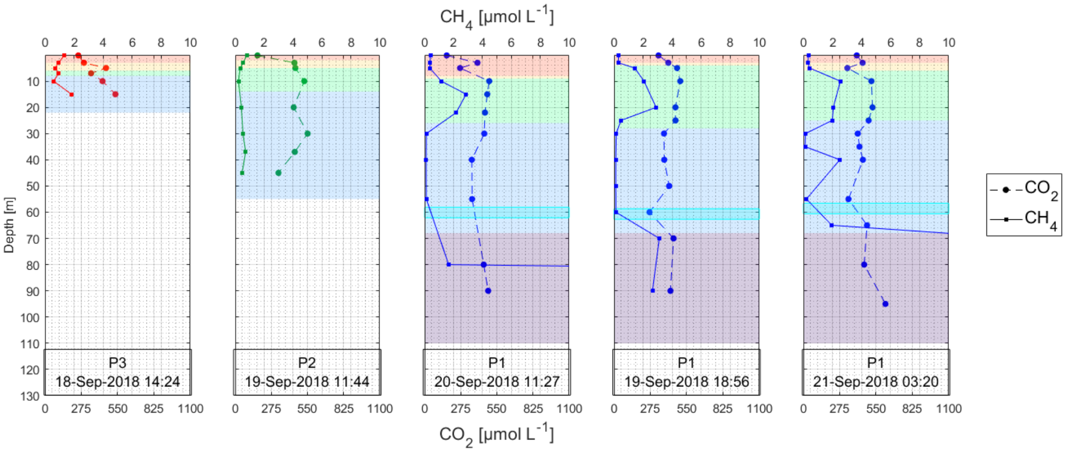

Figure S8. Dissolved CO_2 and CH_4 profiles during C4-L-DWT. The background color represents the layers according to the previously defined conventions (Figure S3). Hidden values: third panel 145 µmol L^{-1} at 90 m depth, right panel 41.4 and 441 µmol L^{-1} at 95 m and 80 m depth, respectively.

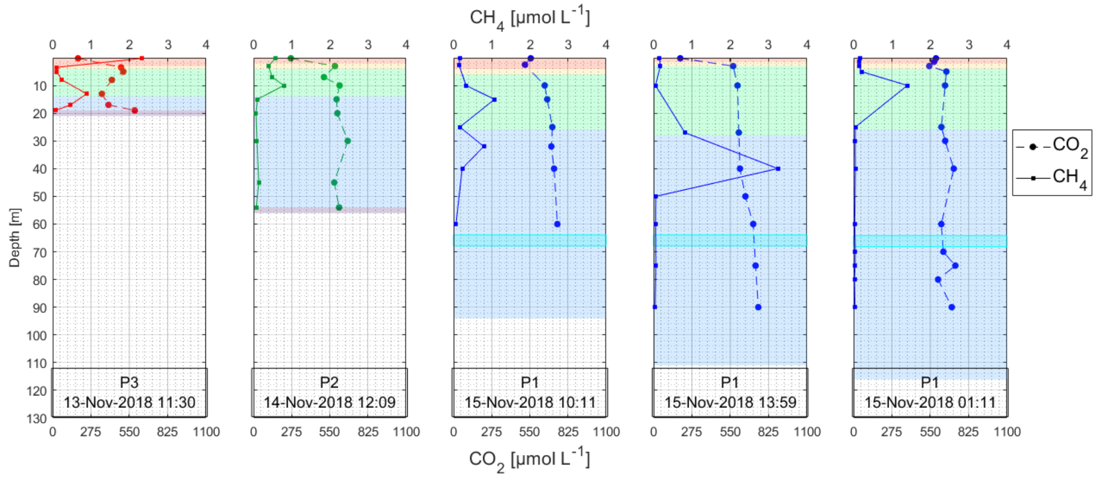

Figure S9. Dissolved CO_2 and CH_4 profiles during C5-M-Wet. The background color represents the layers according to the previously defined conventions (Figure S3).

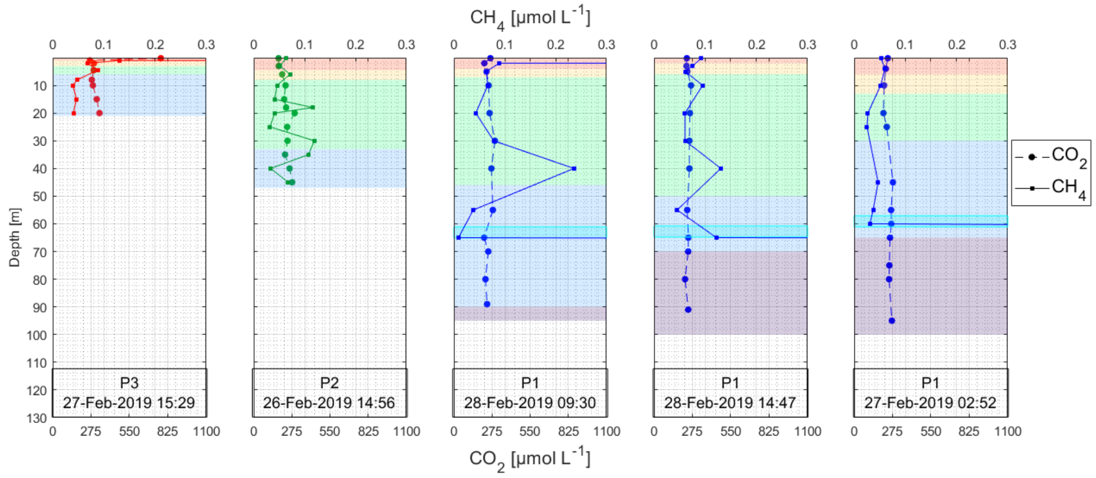

Figure S10. Dissolved CO_2 and CH_4 profiles during C6-M-Dry. The background color represents the layers according to the previously defined conventions (Figure S3). Hidden values: third panel 10.5, 6.73 and 3.384 µmol L^{-1} at 70, 80 and 89 m depth, respectively; forth panel 20.8, 31.2 and 49.8 µmol L^{-1} at 70, 80 and 91 m depth; right panel 20.5 and 20.8 µmol L^{-1} at 80 and 95 m depth, respectively

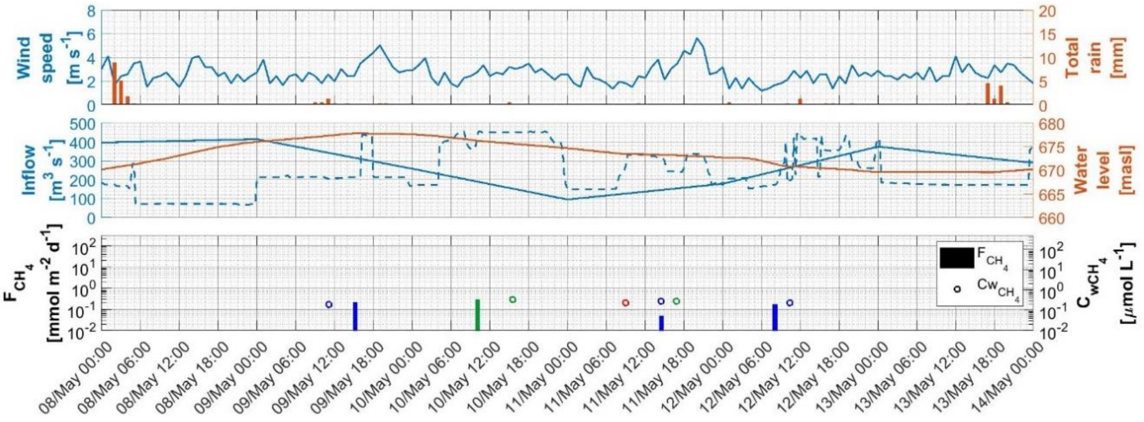

Figure S11. All measured surface concentration of CH_4 and diffusive fluxes during C1-H-Wet and the time series of several forcings. In the panel (b) total inflow in solid line (1 day of resolution) and the sum of the discharges of the upstream reservoirs Porce II and Troneras (1 hour of resolution) and the water level.

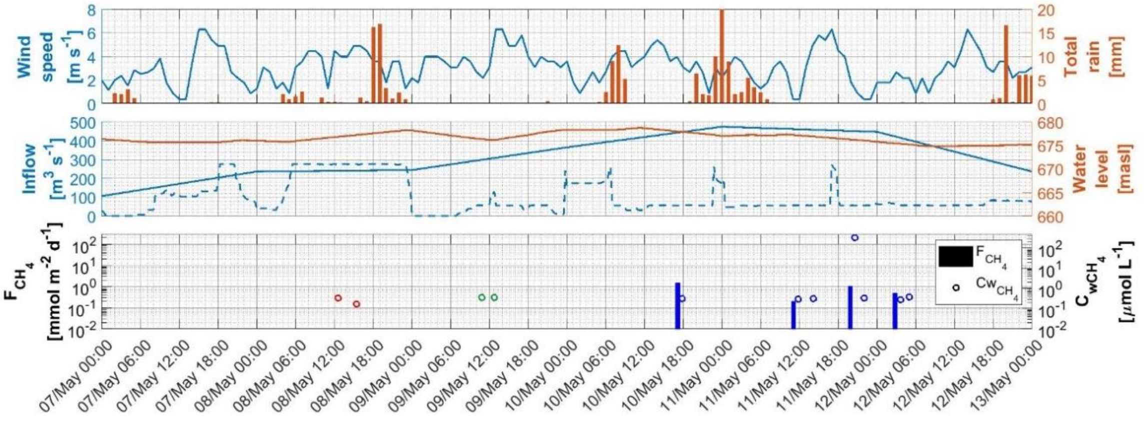

Figure S12. All measured surface concentration of CH_4 and diffusive fluxes during C2-H-Wet and the time series of several forcings. In the panel (b) total inflow in solid line (1 day of resolution) and the sum of the discharges of the upstream reservoirs Porce II and Troneras (1 hour of resolution) and the water level.

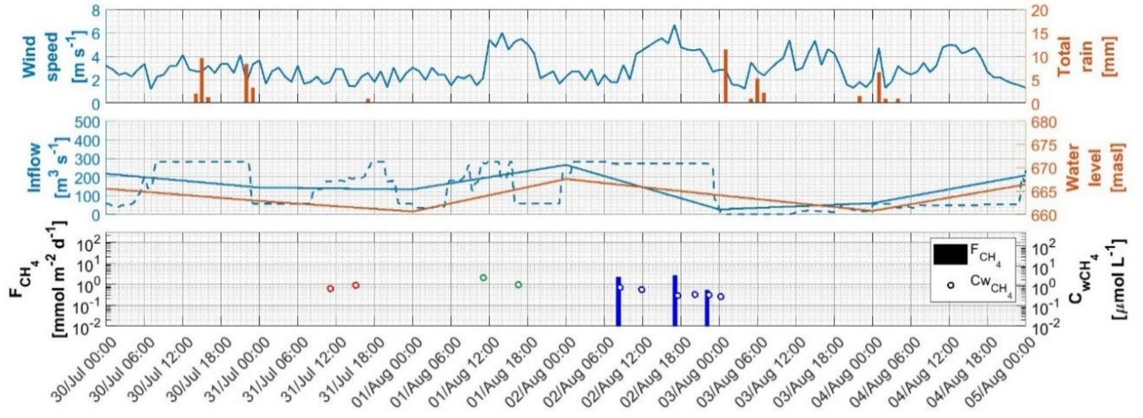

Figure S13. All measured surface concentration of CH_4 and diffusive fluxes during C3-L-Dry and the time series of several forcings. In the panel (b) total inflow in solid line (1 day of resolution) and the sum of the discharges of the upstream reservoirs Porce II and Troneras (1 hour of resolution) and the water level.

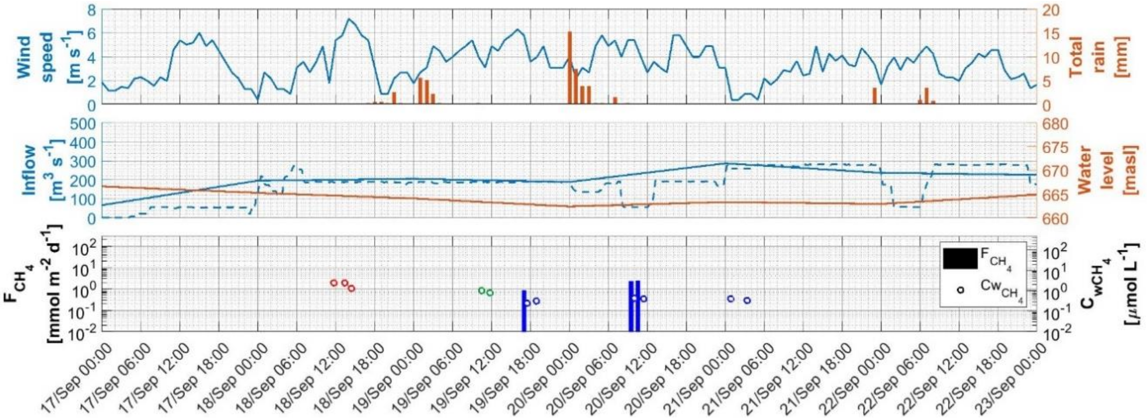

Figure S14. All measured surface concentration of CH_4 and diffusive fluxes during C4-L-DWT and the time series of several forcings. In the panel (b) total inflow in solid line (1 day of resolution) and the sum of the discharges of the upstream reservoirs Porce II and Troneras (1 hour of resolution) and the water level.

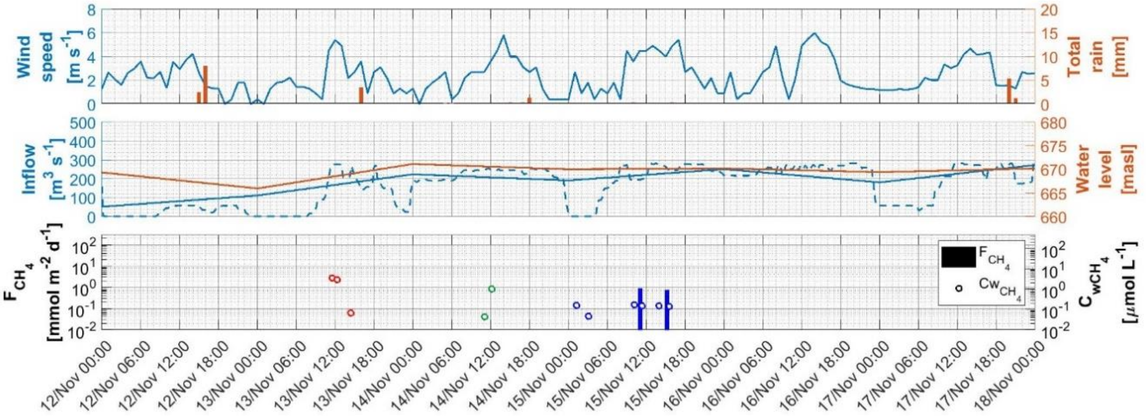

Figure S15. All measured surface concentration of CH_4 and diffusive fluxes during C5-M-Wet and the time series of several forcings. In the panel (b) total inflow in solid line (1 day of resolution) and the sum of the discharges of the upstream reservoirs Porce II and Troneras (1 hour of resolution) and the water level.

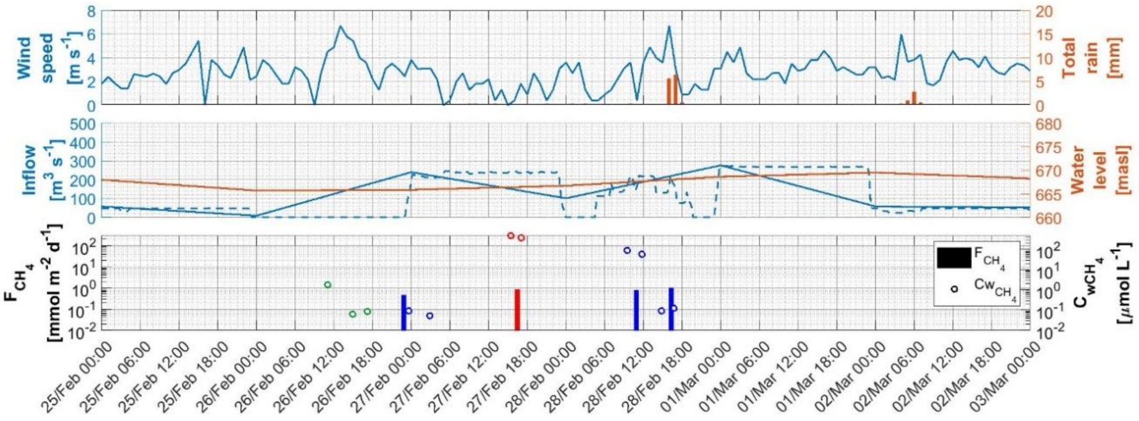

Figure S16. All measured surface concentration of CH$_4$ and diffusive fluxes during C5-M-Wet and the time series of several forcings. In the panel (b) total inflow in solid line (1 day of resolution) and the sum of the discharges of the upstream reservoirs Porce II and Troneras (1 hour of resolution) and the water level.

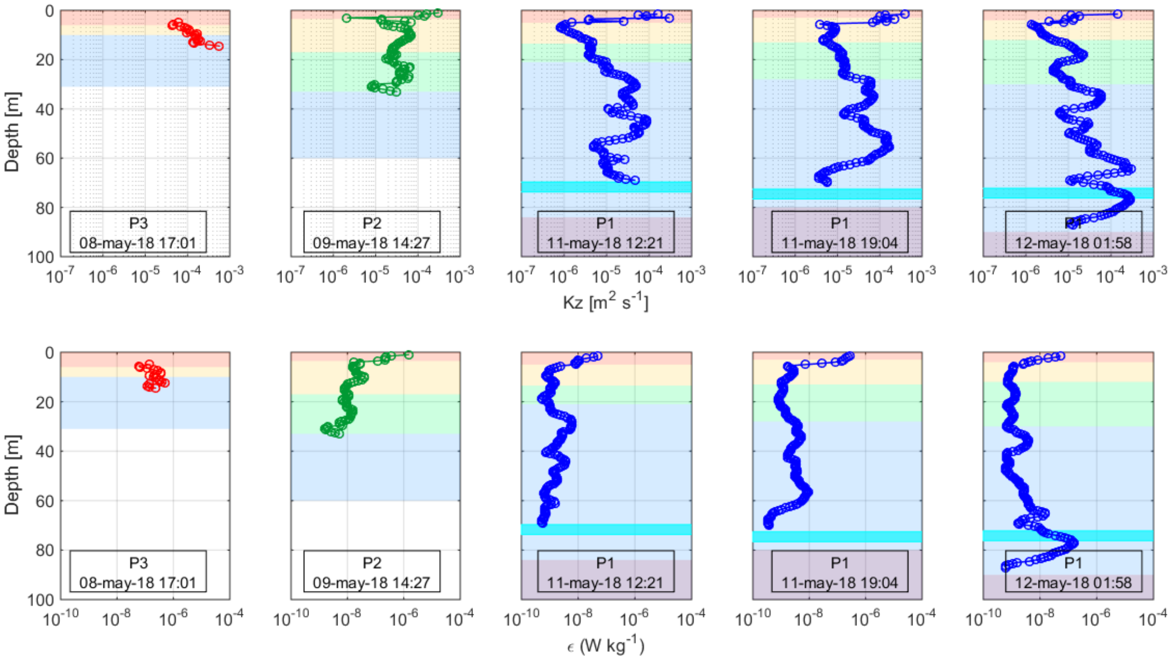

Figure S17. ϵ_m and K_z profiles during C2-H-Wet. The background color represents the layers according to the previously defined conventions (Figure S3)

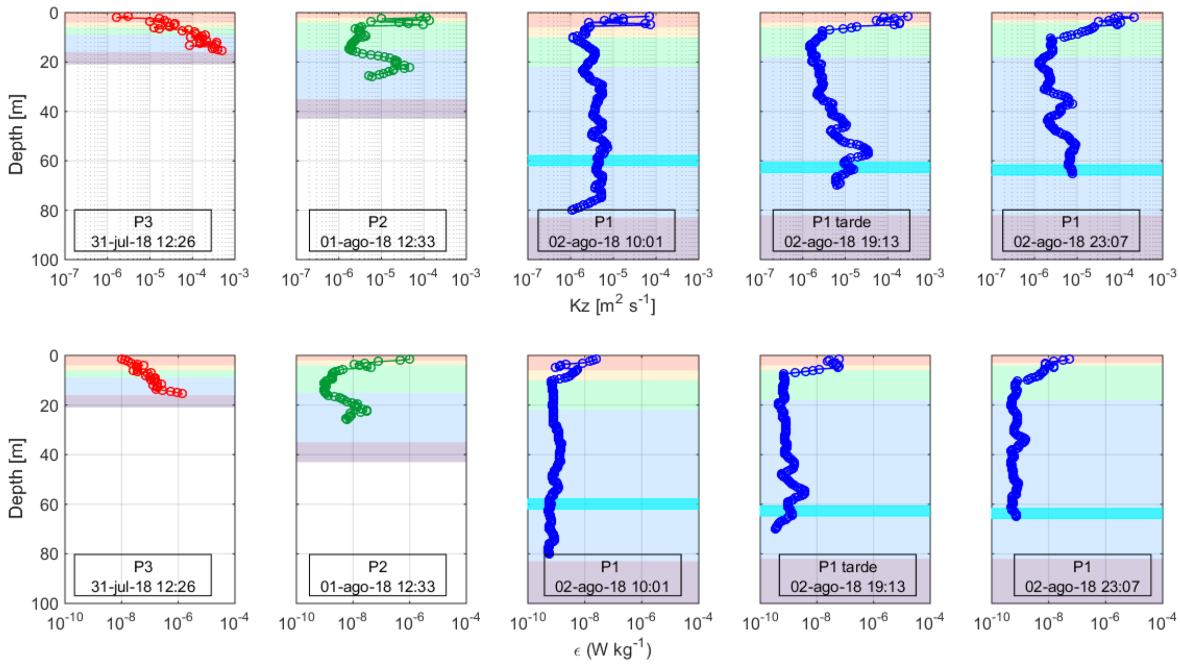

Figure S18. ϵ_m and K_z profiles during C3-L-Dry. The background color represents the layers according to the previously defined conventions (Figure S3).

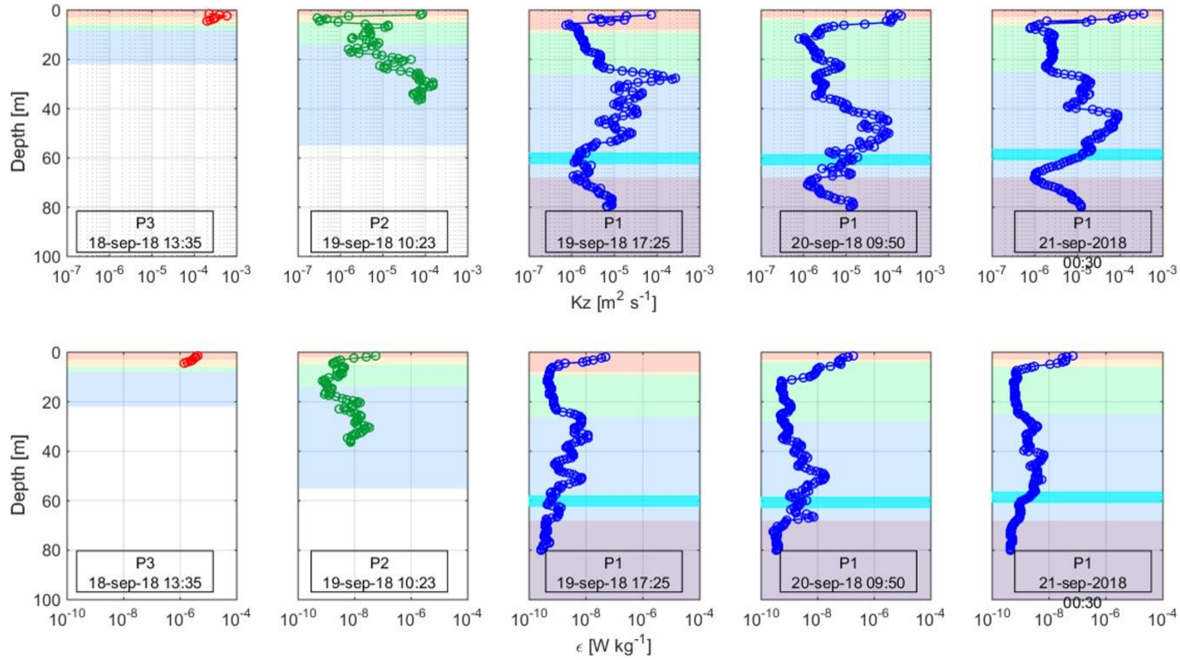

Figure S19. ϵ_m and K_z profiles during C4-L-DWT. The background color represents the layers according to the previously defined conventions (Figure S3).

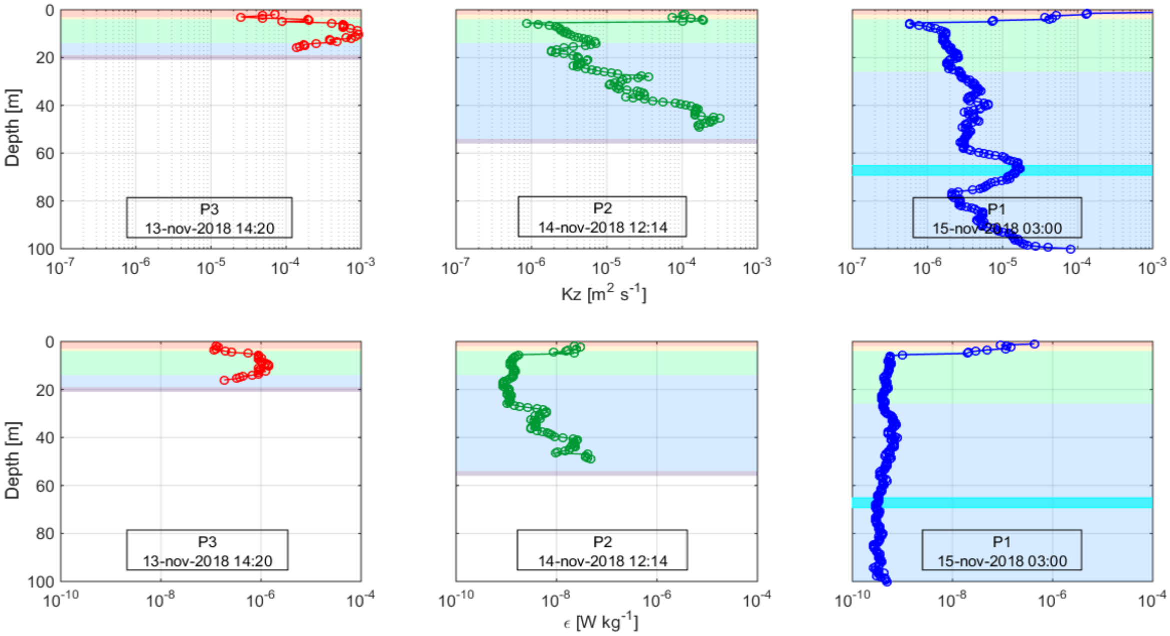

Figure S20. ϵ_m and K_z profiles during C5-M-Wet. The background color represents the layers according to the previously defined conventions (Figure S3).

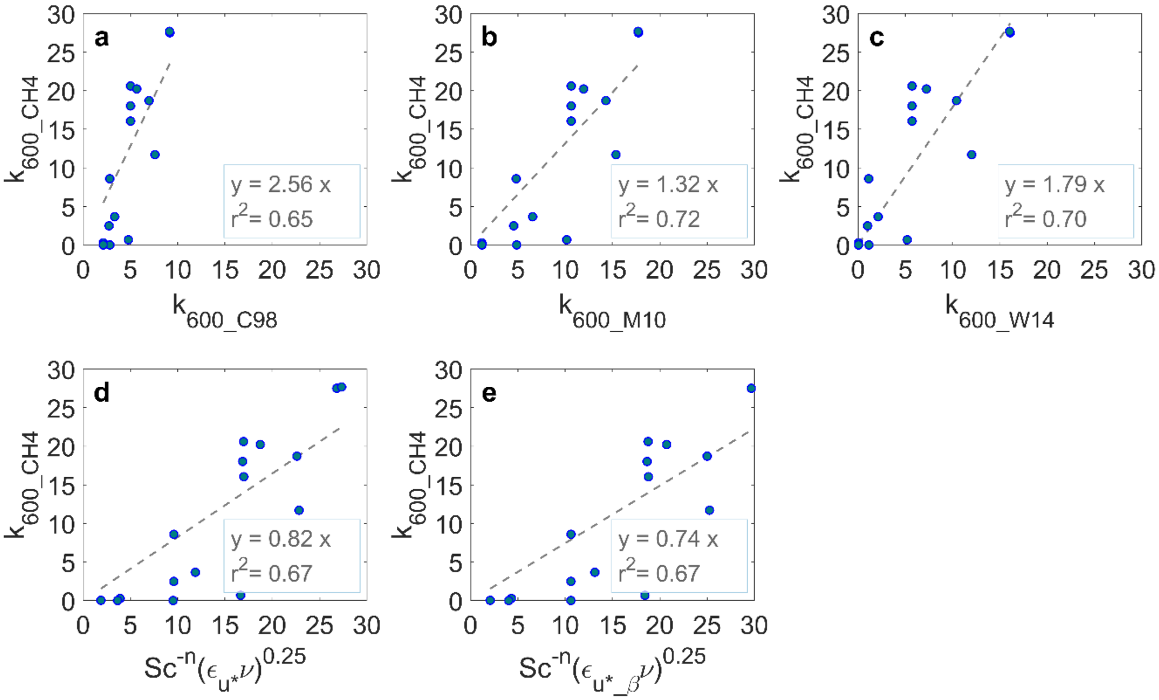

Figure S21. Gas exchange velocities estimated from CH4 fluxes ($k_{600\_CH_4}$) vs models of k_{600} only day hours (n =11): **a**. Cole & Caraco (1998), **b**. MacIntyre (2010), **c**. Wanninkhof (2014) and **d**. SRM_u* and **e**. SRM_u*_β. Circles show measurements and lines through the origin (dashed lines) and not forced through the origin (solid lines) according to the equations presented in the legends

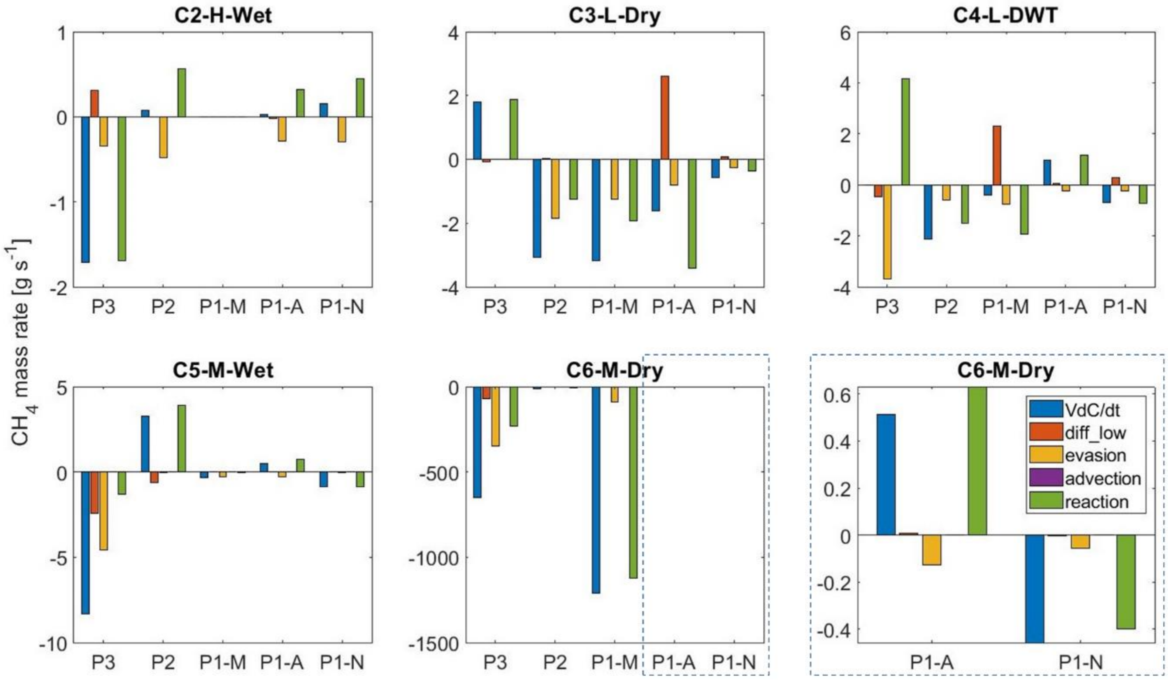

Figure S22. Mass balances of CH4 extrapolated to the three different zones of the reservoir. The components *VdC/dt* and *evasion* were multiplied by the surface areas of the respective zone, the component *diff_low* was multiplied by the surface area at the bottom of the SML (thermocline) and the *advection* was multiplied by the transversal area of the SML. All of them taking representative areas of each sampling point as explained in the manuscript. The *reaction* term was solved from the equation (2-8)

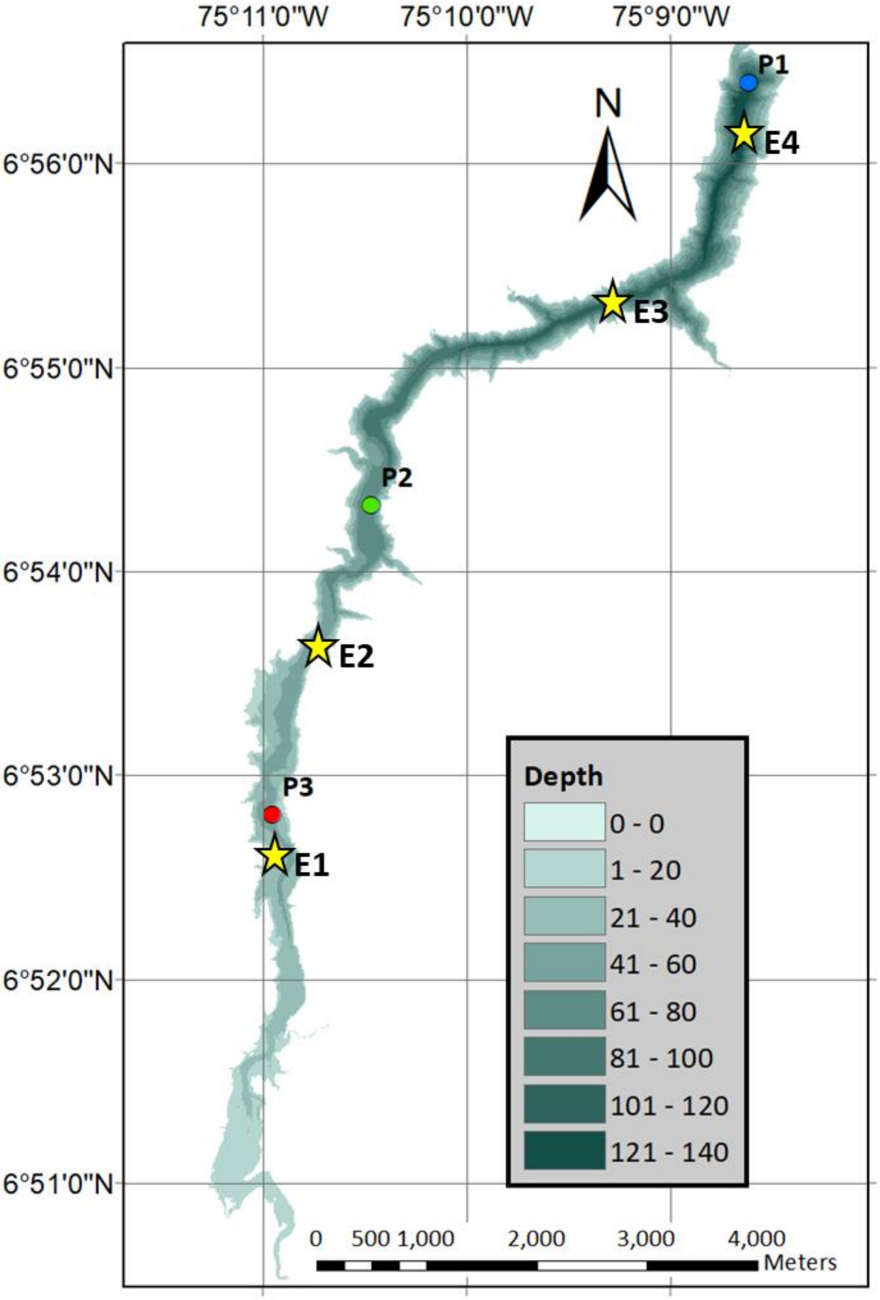

Figure S23. Sampling stations in Porce III reservoir: This study (colored circles and nomenclature denoted by the letter P) and quality monitoring stations of the reservoir operator (yellow stars and nomenclature denoted by the letter E)

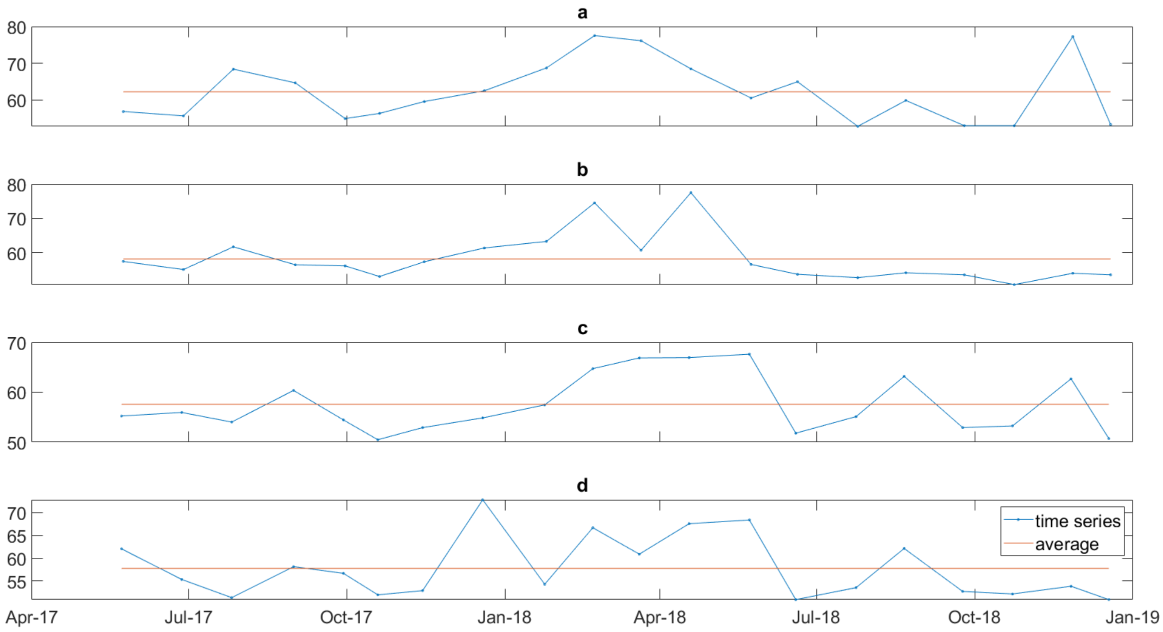

Figure S24. TSI for four monitoring stations. Source: EPM. **a**, **b**, **c** and **d** are the data for four stations along Porce III from the riverine zone towards the dam.

Appendix B: Supplementary information on chapter 4

Text S1. Estimate of the accuracy of the PIV System

According to Thielicke (2014), the accuracy of the PIV velocity estimates depends mainly on the cross-correlation algorithm and the choice of the peak-finding technique. By using the DFT plus deformation window approach and running several passes, the error sources, such as loss of information and background noise in the correlation matrix, are significantly mitigated. The Gaussian 2.3 –point fit for the peak finding in the cross correlation refines the results to a subpixel precision, but normally some complications in the detection of the intensity peak can occur due to non-uniform particle motion inside the interrogation area, which broadens the intensity peak. The use of the deformation window reduces shear and rotation within the interrogation area. The particle diameters and particle density in the interrogation area also influence the accuracy of the velocity measurements. Thielicke (2014) recommends diameters larger than 3 pixels and particle densities up to 20 particles per interrogation area (IA) (at the final pass). Under these conditions and the use of DFT plus deformation window algorithm, and the Gaussian 2.3-point fit for the peak finding, this author found bias errors <0.005 pixels and random errors <0.02 pixels. In our experiment, we used the recommended algorithm and peak-finding settings, the last pass of the deformation area was at 64 × 64 of the IA and we obtained a final particle median particle diameter of 3.9 pixels and a particle density of 12.6 particles per IA (n = 4503).

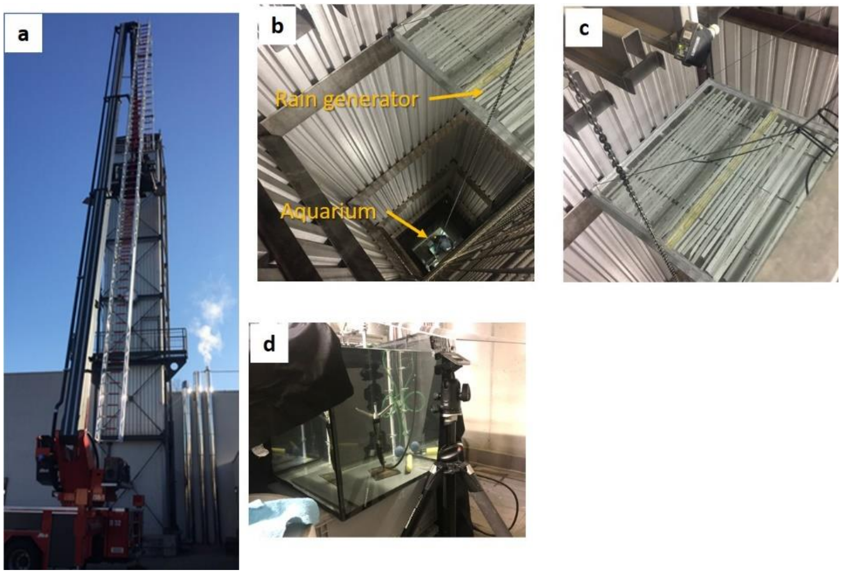

Figure S1. Pictures of the experimental setup: a) Hose-drying tower (approximately 20 m tall) of the municipal fire brigade in Landau, Germany, in which experiments were conducted. b) Inside view showing the rain generator in the top and the aquarium at the base of the tower. c)detailed view of the rain generator (cf. Fig. 1). d) Aquarium with sensors and camera mounting frame.

Figure S2. Picture of the rain generator: The outer aluminum frame (1 x 1 x 0.05 m) was filled with water and raindrops formed at regularly arranged holes in the transparent bottom plate. The rainfall rate was varied by closing or opening a varying number of holes using adhesive tape (visible as black and silver tape stripes in the picture).

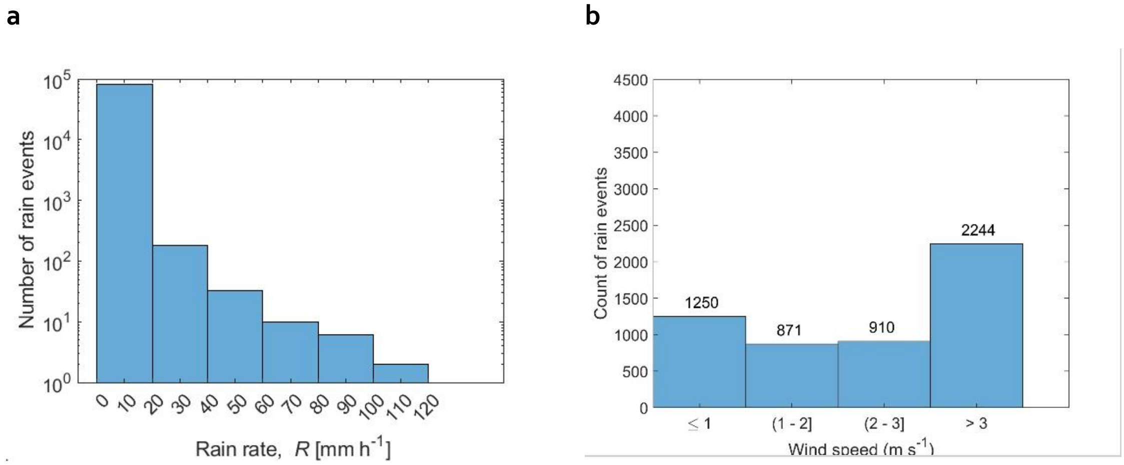

Figure S3. Histogram of rain events collected by a meteorological station located on the water surface of Porce III reservoir, Colombia (6°54'12.6"N, 75°10'16.1"W). Data were obtained from measurements with 1h resolution for the periods from 19-Nov-2019 to 09-Mar-2020 and from 01-Sep-2021 to 10-Dec-2021 (n = 81601). a. Rainfall rate frequencies, b. Rain events frequencies at different wind speed.

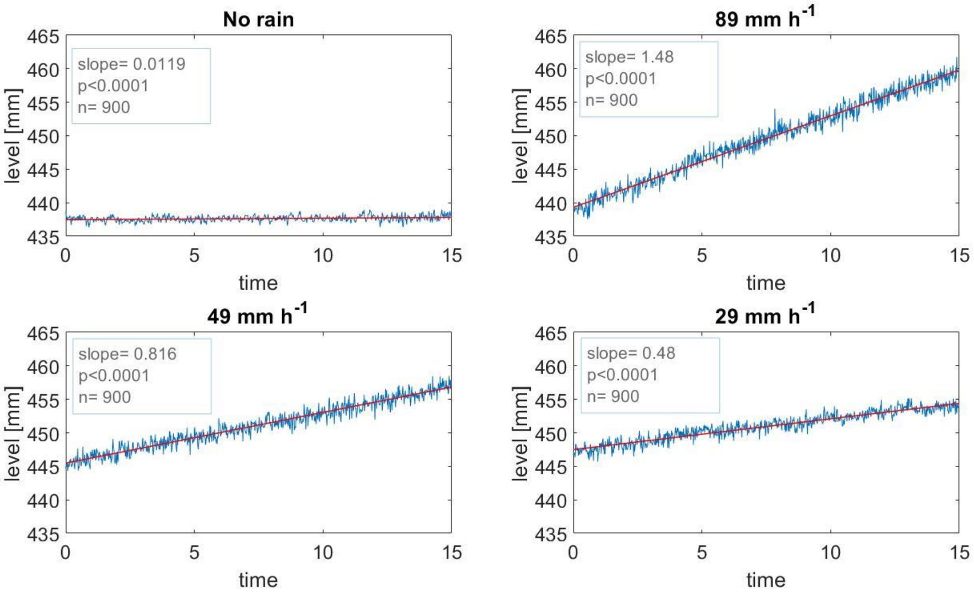

Figure S4. Time series of pressure measured with the RBR sensor during an experimental series: without rain and for three different rain rates (see panel headings). The slopes (in mm min^{-1}) and regression statistics (the p-value is the significance of the slope applying the t-test, and *n* is the number of points used for the fit and t-test) reported in the text boxes are for the linear regressions (red solid lines) using all data (15 min of measurements).

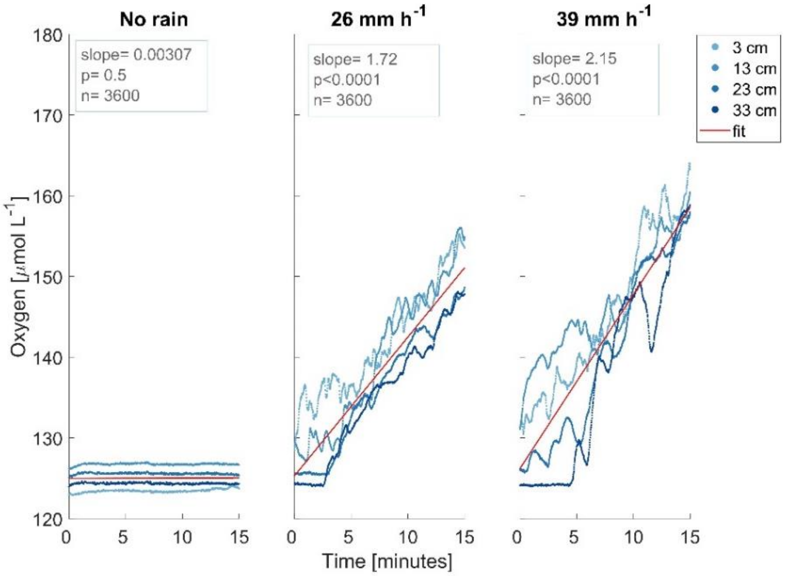

Figure S5. Time series of dissolved oxygen concentration at different sampling depth in the aquarium (line color, see legend) observed without rain and for two different rain rates (see panel headings). Red solid lines show linear regressions that were used for estimating the gas transfer velocity according to Eq. (3). The slopes (in µmol L^{-1} min^{-1}) in the text boxes are those of linear regressions using all data, the p-value is the significance of the slope applying the t-test, and n is the number of points used for the fit.

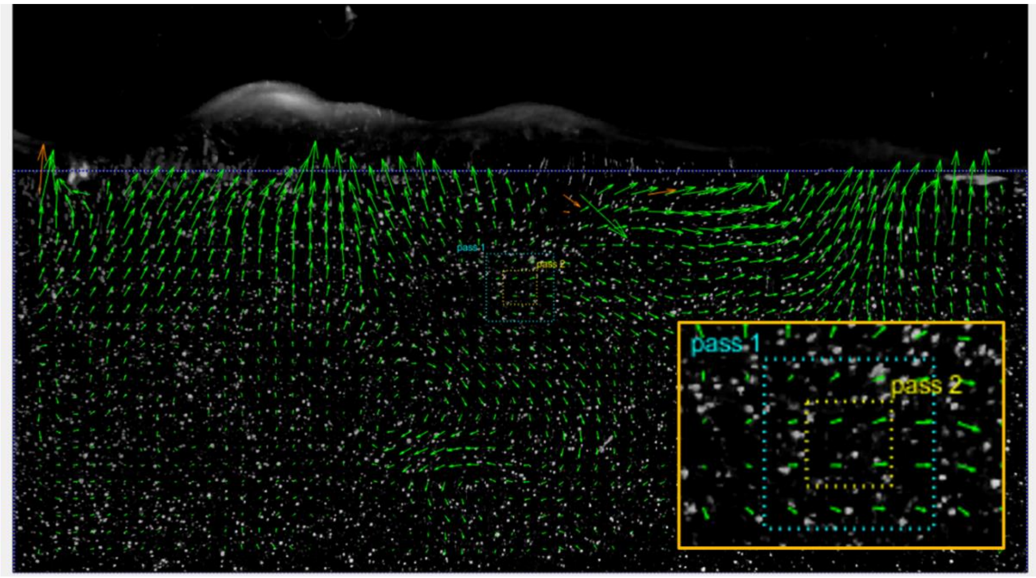

Figure S6. Example of the analysis results in PIVlab of a pair pre-processed images: Region of interest (dark blue dashed line) extracted from the field of view; fluorescent particles in water (white points); the velocity vectors resulting from the analysis of a pair images (green arrows) and the interrogation areas from the two passes used in the data analysis (zoom at left-bottom in the yellow square).

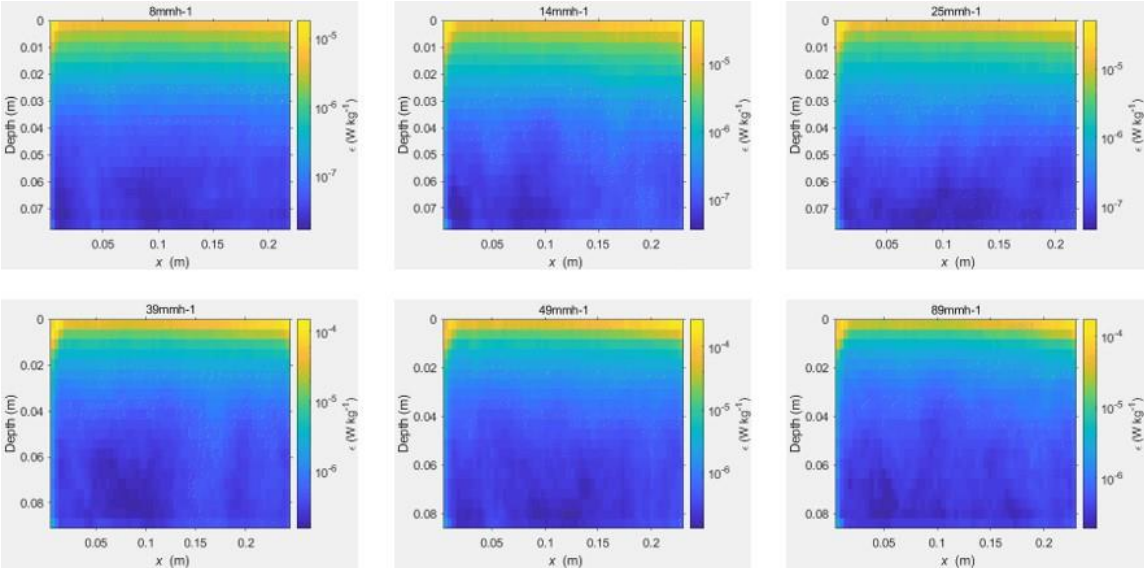

Figure S7. Spatial distribution of the time-averaged turbulent dissipation rates (ϵ_{t_avg}) for six different rain rates (see panel titles).

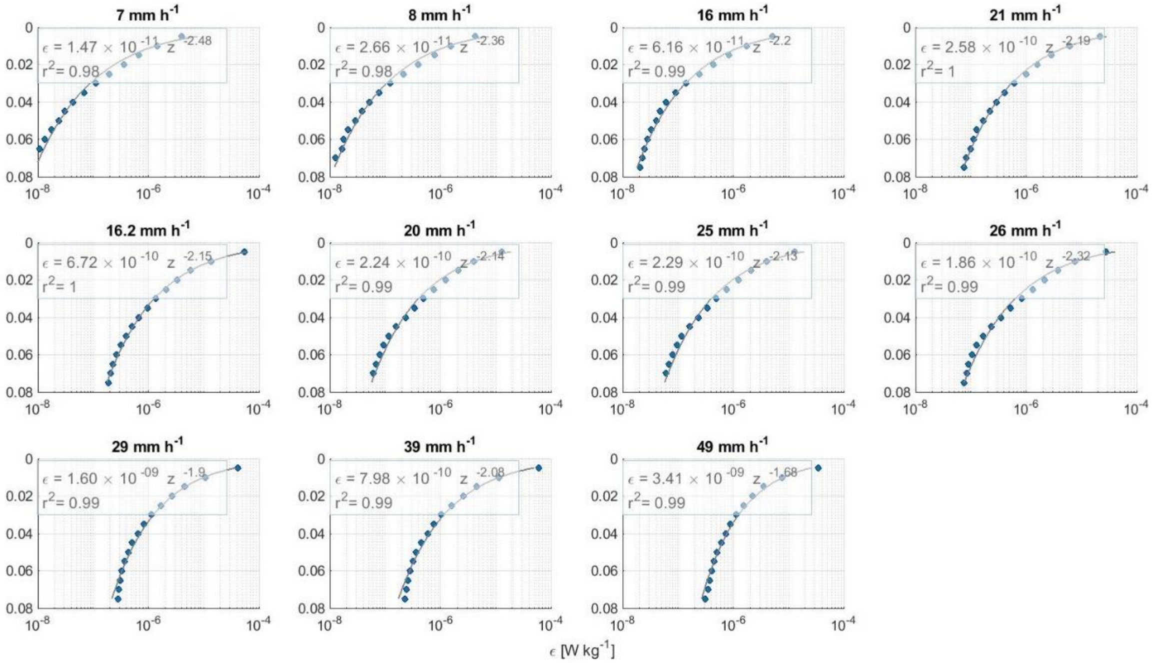

Figure S8. Mean vertical profiles of dissipation rates of turbulent kinetic energy for all measured rain rates (filled symbols). The solid lines show power-law fits according to the function shown in each legend.

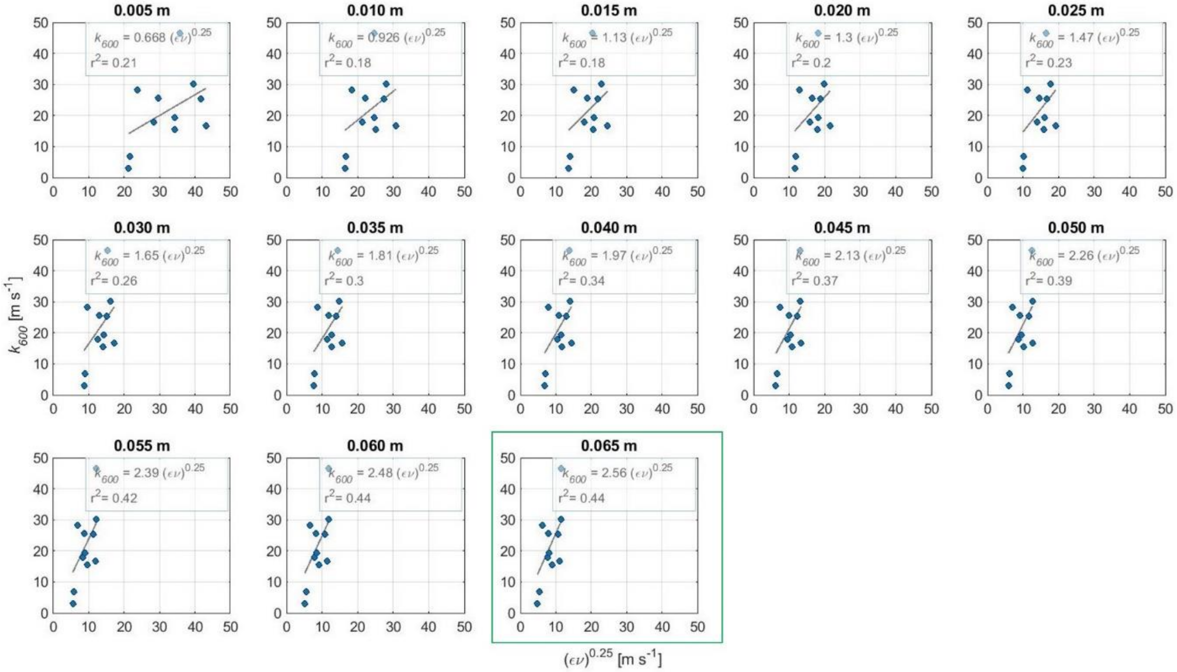

Figure S9. Normalized gas transfer velocities k600 versus the surface renewal model (Eq. (13)) for different water depth at which dissipation rates (ϵ) were measured. Solid lines show linear regressions according to the equation shown in the legends. The best fit, which was chosen to estimate the empirical coefficient A is highlighted by the green bounding box.

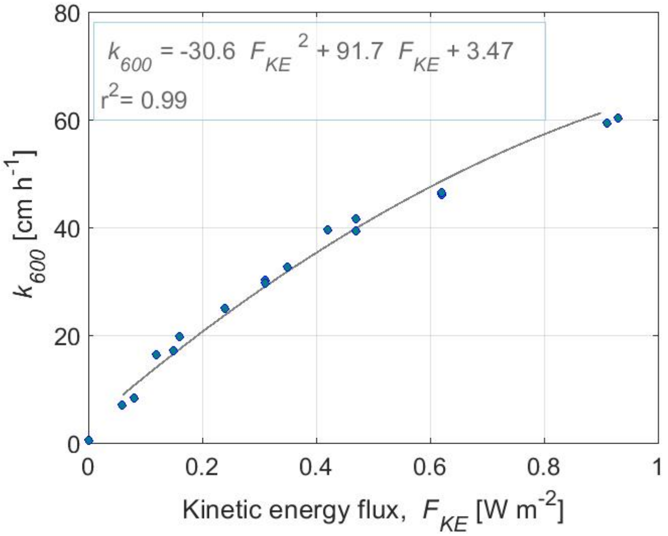

Figure S10. Normalized gas transfer velocity k600 as a function of the kinetic energy flux of rain reported in (Ho et al., 1997) (their Table 1). The solid line shows a polynomial fit according the equation shown in the legend.

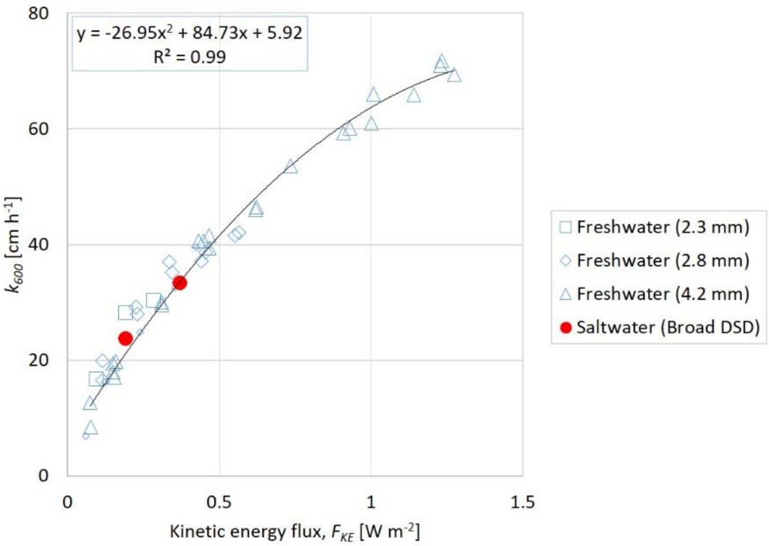

Figure S11. Normalized gas transfer velocity k600 as a function of the kinetic energy flux of rain reported in (Ho et al., 2000) and (Zappa et al., 2009) (taken from Figure 8 in (Zappa et al., 2009)). The solid line shows a polynomial fit according the equation shown in the legend. In the legend, the values in parenthesis report the averaged drop size for freshwater experiments corresponding to the results of (Ho et al., 2000) and saltwater experiments correspond to the results of (Zappa et al., 2009), in which there was a broad drop size distribution (DSD).

Table S1. Comparison of turbulent dissipation rates from PIV_dir (equation (9)), PIV_spec and ADV (equation (10)) for all runs at the ADV sampling point location (10 cm depth).

R [mm h^{-1}]	ϵ_{PIV_dir} [W/kg]	ϵ_{PIV_spec} [W/kg]	ϵ_{ADV} [W/kg]
6.9	4.82×10^{-8}	1.42×10^{-8}	1.20×10^{-8}
8.1	4.85×10^{-8}	1.29×10^{-8}	1.10×10^{-8}
10.3	9.52×10^{-8}	4.03×10^{-8}	7.50×10^{-8}
13.5	1.61×10^{-7}	8.03×10^{-8}	4.29×10^{-6}
16.0	1.69×10^{-7}	3.06×10^{-8}	2.29×10^{-7}
21.1	3.55×10^{-8}	5.31×10^{-9}	4.99×10^{-7}
16.2	2.59×10^{-7}	1.52×10^{-7}	6.74×10^{-7}
19.8	3.16×10^{-7}	1.13×10^{-6}	1.47×10^{-7}
25.0	9.09×10^{-8}	1.71×10^{-7}	5.77×10^{-7}
26.0	1.88×10^{-7}	1.15×10^{-7}	3.28×10^{-6}
28.8	1.77×10^{-7}	8.36×10^{-7}	4.16×10^{-6}
39.4	3.66×10^{-7}	1.05×10^{-7}	1.33×10^{-6}
49.0	3.03×10^{-7}	1.27×10^{-7}	5.23×10^{-6}
89.0	4.20×10^{-7}	3.06×10^{-7}	2.48×10^{-6}

References

Abe, D. S., Adams, D. D., Sidagis Galli, C. V., Sikar, E., & Tundisi, J. G. (2005). Sediment greenhouse gases (methane and carbon dioxide) in the Lobo-Broa Reservoir, São Paulo State, Brazil: Concentrations and diffuse emission fluxes for carbon budget considerations. *Lakes and Reservoirs: Research and Management*, *10*(4), 201–209. https://doi.org/10.1111/j.1440-1770.2005.00277.x

Abril, G., Bouillon, S., Darchambeau, F., Teodoru, C. R., Marwick, T. R., Tamooh, F., Ochieng Omengo, F., Geeraert, N., Deirmendjian, L., Polsenaere, P., & Borges, A. V. (2015). Technical note: Large overestimation of pCO2 calculated from pH and alkalinity in acidic, organic-rich freshwaters. *Biogeosciences*, *12*(1), 67–78. https://doi.org/10.5194/bg-12-67-2015

Abril, G., Guérin, F., Richard, S., Delmas, R., Galy-Lacaux, C., Gosse, P., Tremblay, A., Varfalvy, L., Dos Santos, M. A., & Matvienko, B. (2005). Carbon dioxide and methane emissions and the carbon budget of a 10-year old tropical reservoir (Petit Saut, French Guiana). *Global Biogeochemical Cycles*, *19*(4), 1–16. https://doi.org/10.1029/2005GB002457

Anthony, K. W., & MacIntyre, S. (2016). Nocturnal escape route for marsh gas. *Nature*, *535*(7612), 363–365. https://doi.org/10.1038/535363a

Baker, M. A., & Gibson, C. H. (1987). Sampling turbulence in the stratified ocean: statistical consequences of strong intermittency. In *J. Phys. Oceanogr.* (Vol. 17, Issues 10, Oct. 1987, pp. 1817–1836). https://doi.org/10.1175/1520-0485(1987)017<1817:stitso>2.0.co;2

Banks, R. B., Wickramanayake, B., & Lohani, B. N. (1984). Effect of Wind and Rain on Surface Reaeration. *Journal of the Environmental Engineering*, *110*, 1–14. https://doi.org/10.1061/(ASCE)0733-9372(1984)110:1(1)

Barbosa, P. M., Melack, J. M., Amaral, J. H. F., MacIntyre, S., Kasper, D., Cortés, A., Farjalla, V. F., & Forsberg, B. R. (2020). Dissolved methane concentrations and fluxes to the atmosphere from a tropical floodplain lake. *Biogeochemistry*, *148*(2), 129–151. https://doi.org/10.1007/s10533-020-00650-1

Barros, N., Cole, J. J., Tranvik, L. J., Prairie, Y. T., Bastviken, D., Huszar, V. L. M., del Giorgio, P., & Roland, F. (2011). Carbon emission from hydroelectric reservoirs linked to reservoir age and latitude. *Nature Geoscience*, *4*(9), 593–596. https://doi.org/10.1038/ngeo1211

Bartosiewicz, M., Laurion, I., & MacIntyre, S. (2015). Greenhouse gas emission and storage in a small shallow lake. *Hydrobiologia*, *757*(1), 101–115. https://doi.org/10.1007/s10750-015-2240-2

Bastviken, D., Cole, J. J., Pace, M. L., & Van de-Bogert, M. C. (2008). Fates of methane from different lake habitats: Connecting whole-lake budgets and CH4emissions. *Journal of Geophysical Research: Biogeosciences*, *113*(2). https://doi.org/10.1029/2007JG000608

Bastviken, D., Cole, J., Pace, M., & Tranvik, L. (2004a). Methane emissions from lakes: Dependence of lake characteristics, two regional assessments, and a global estimate. *Global Biogeochemical Cycles*, *18*(4), 1–12. https://doi.org/10.1029/2004GB002238

Bastviken, D., Cole, J., Pace, M., & Tranvik, L. (2004b). Methane emissions from lakes: Dependence of lake characteristics, two regional assessments, and a global estimate. *Global Biogeochemical Cycles*, *18*(4), 1–12. https://doi.org/10.1029/2004GB002238

Bastviken, D., Sundgren, I., Natchimuthu, S., Reyier, H., & Gålfalk, M. (2015). Technical Note: Cost-efficient approaches to measure carbon dioxide fluxes and concentrations in terrestrial and aquatic environments using mini loggers. *Biogeosciences*, *12*(12), 3849–3859. https://doi.org/10.5194/bg-12-3849-2015

Bastviken, D., Tranvik, L. J., Downing, J., Crill, J. a, M, P., & Enrich-prast, A. (2011). Freshwater Methane Emissions Offset the Continental Carbon Sink. *Science*, *331*, 50. https://doi.org/10.1126/science.1196808

Belanger, T. V., & Korzun, E. A. (1990). Rainfall-reaeration effects. *Air-Water Mass Transfer*, *116*(4), 582–587.

Beyá, J., Peirson, W., & Banner, M. (2011). Rainfall-generated, near-surface turbulence. In S. Komori, W. McGillis, & R. Kurose (Eds.), *Gas transfer at water surfaces 2010* (pp. 90–103). Kyoto University Press 2011.

Bižić, M., Klintzsch, T., Ionescu, D., Hindiyeh, M. Y., Günthel, M., Muro-Pastor, A. M., Eckert, W., Urich, T., Keppler, F., & Grossart, H. P. (2020). Aquatic and terrestrial cyanobacteria produce methane. *Science Advances*, *6*(3). https://doi.org/10.1126/sciadv.aax5343

Blees, J., Niemann, H., Erne, M., Zopfi, J., Schubert, C. J., & Lehmann, M. F. (2015). Spatial variations in surface water methane super-saturation and emission in Lake Lugano, southern Switzerland. *Aquatic Sciences*, *77*(4), 535–545. https://doi.org/10.1007/s00027-015-0401-z

Bluteau, C. E., Jones, N. L., & Ivey, G. N. (2011). Estimating turbulent kinetic energy dissipation using the inertial subrange method in environmental flows. *Limnology and Oceanography: Methods*, *9*(JULY), 302–321. https://doi.org/10.4319/lom.2011.9.302

Boehrer, B., & Schultze, M. (2009). Stratification of lakes. *Reviews of Geophysics*, *46*(2), 583–593. https://doi.org/10.1029/2006RG000210

Bogard, M. J., del Giorgio, P. A., Boutet, L., Chaves, M. C. G., Prairie, Y. T., Merante, A., & Derry, A. M. (2014). Oxic water column methanogenesis as a major component of aquatic CH4 fluxes. *Nature Communications*, *5*. https://doi.org/10.1038/ncomms6350

Borges, A. V., Darchambeau, F., Teodoru, C. R., Marwick, T. R., Tamooh, F., Geeraert, N., Omengo, F. O., Guérin, F., Lambert, T., Morana, C., Okuku, E., & Bouillon, S. (2015). Globally significant greenhouse-gas emissions from African inland waters. *Nature Geoscience*, *8*(8), 637–642. https://doi.org/10.1038/ngeo2486

Bouffard, D., & Boegman, L. (2013). Dynamics of Atmospheres and Oceans A diapycnal diffusivity model for stratified environmental flows. *Dynamics of Atmospheres and Oceans*, *61–62*, 14–34. https://doi.org/10.1016/j.dynatmoce.2013.02.002

Bridgham, S. D., Cadillo-Quiroz, H., Keller, J. K., & Zhuang, Q. (2013). Methane emissions from wetlands: Biogeochemical, microbial, and modeling perspectives from local to global scales. *Global Change Biology*, *19*(5), 1325–1346. https://doi.org/10.1111/gcb.12131

Camargo, J. A., & Alonso, A. (2007). Contaminación por nitrógeno inorgánico en los ecosistemas acuáticos : problemas medioambientales, criterios de calidad del agua e implicaciones del cambio climático. *Ecosistemas*, *16*(2), 98–110.

Castro - González, M., & Torres-Valdés, V. (2015). Gases invernadero en aguas con bajo oxígeno en el reservorio eutrófico de Prado (Colombia). *Revista de La Academia*

Colombiana de Ciencias Exactas, Físicas y Naturales, *39*(152), 399. https://doi.org/10.18257/raccefyn.228

Chapra, S. C. (1997). *Surface Water-Quality Modeling* (B. J. Clark, D. A. Damstra, & J. W. Bradley, Eds.). McGraw Hill.

Ciais, P., Sabine, C., Bala, G., Bopp, L., Brovkin, V., Canadell, J., Chhabra, A., DeFries, R., Galloway, J., Heimann, M., Jones, C., Quéré, C. Le, Myneni, R. B., Piao, S., & Thornton, P. (2013). The physical science basis. Contribution of working group I to the fifth assessment report of the intergovernmental panel on climate change. *Change, IPCC Climate*, 465–570. https://doi.org/10.1017/CBO9781107415324.015

Ciarlini, P., Catombé, C., Lucia, R., Nobre, G., Kosten, S., Martins, E., Carvalho, F. De, Sarmento, H., Angelini, R., Terra, I., Gaudêncio, A., Haig, N., Becker, V., Rodrigues, C., Quesado, L., Silva, L., Caliman, A., & Megali, A. (2019). Effects of seasonality, trophic state and landscape properties on CO2 saturation in low-latitude lakes and reservoirs. *Science of the Total Environment*, *664*, 283–295. https://doi.org/10.1016/j.scitotenv.2019.01.273

Cole, J., & Caraco, N. F. (1998a). Atmospheric Exchange of Carbon Dioxide in a Low-Wind Oligotrophic Lake Measured by the Addition of SF6. *Limnology and Oceanography*, *43*(4), 647–656. https://doi.org/10.4319/lo.1998.43.4.0647

Cole, J., & Caraco, N. F. (1998b). Atmospheric exchange of carbon dioxide in a low-wind oligotrophic the addition of SF6. *Limnology and Oceanography*, *43*(4), 647–656.

Cole, J. J., Prairie, Y. T., Caraco, N. F., McDowell, W. H., Tranvik, L. J., Striegl, R. G., Duarte, C. M., Kortelainen, P., Downing, J. A., Middelburg, J. J., & Melack, J. (2007). Plumbing the Global Carbon Cycle: Integrating Inland Waters into the Terrestrial Carbon Budget. *Ecosystems*, *10*, 171–184. https://doi.org/10.1007/s 10021-006-9013-8

Czikowsky, M. J., MacIntyre, S., Tedford, E. W., Vidal, J., & Miller, S. D. (2018). Effects of Wind and Buoyancy on Carbon Dioxide Distribution and Air-Water Flux of a Stratified Temperate Lake. *Journal of Geophysical Research: Biogeosciences*, *123*(8), 2305–2322. https://doi.org/10.1029/2017JG004209

Deemer, B. R., Harrison, J. A., Li, S., Beaulieu, J. J., Delsontro, T., Barros, N., Bezerra-Neto, J. F., Powers, S. M., Santos, M. A. D. O. S., Vonk, J. A., Dos Santos, M. A., &

Vonk, J. A. (2016). Greenhouse gas emissions from reservoir water surfaces: A new global synthesis. *BioScience*, *66*(11), 949–964. https://doi.org/10.1093/biosci/biw117

Delmas, R., & Galy-lacaux, C. (2001). Emissions of greenhouse gases from the tropical hydroelectric reservoir of Petit Saut (French Guiana) compared with emissions of thermal alternatives. *Global Biogeochemical Cycles*, *15*(4), 993–1003.

Delsontro, T., Beaulieu, J. J., & Downing, J. A. (2018). Greenhouse gas emissions from lakes and impoundments: Upscaling in the face of global change. *Limnology and Oceanography Letters*, *March*, 64–75. https://doi.org/10.1002/lol2.10073

Demarty, M., & Bastien, J. (2011). GHG emissions from hydroelectric reservoirs in tropical and equatorial regions: Review of 20 years of CH4 emission measurements. *Energy Policy*, *39*(7), 4197–4206. https://doi.org/10.1016/j.enpol.2011.04.033

D'Errico. (2012). *inpaint_nans*. MATLAB Central File Exchange. https://www.mathworks.com/matlabcentral/fileexchange/4551-inpaint_nans

Deshmukh, C., Guérin, F., Labat, D., Pighini, S., Vongkhamsao, A., Guédant, P., Rode, W., Godon, A., Chanudet, V., Descloux, S., & Serça, D. (2016). Low methane (CH4) emissions downstream of a monomictic subtropical hydroelectric reservoir (Nam Theun 2, Lao PDR). *Biogeosciences*, *13*(6). https://doi.org/10.5194/bg-13-1919-2016

Donis, D., Flury, S., & Spangenberg, J. E. (2017). Full-scale evaluation of methane production under oxic conditions in a mesotrophic lake. *Nature Communications*, *8*(1661), 1–11. https://doi.org/10.1038/s41467-017-01648-4

Doron, P., Bertuccioli, L., Katz, J., & Osborn, T. R. (2001). Turbulence characteristics and dissipation estimates in the coastal ocean bottom boundary layer from PIV data. *Journal of Physical Oceanography*, *31*(8 PART 1), 2108–2134. https://doi.org/10.1175/1520-0485(2001)031<2108:tcadei>2.0.co;2

dos Santos, M. A., Rosa, L. P., Sikar, B., Sikar, E., & dos Santos, E. O. (2006). Gross greenhouse gas fluxes from hydro-power reservoir compared to thermo-power plants. *Energy Policy*, *34*(4), 481–488. https://doi.org/10.1016/j.enpol.2004.06.015

Erkkilä, K. M., Ojala, A., Bastviken, D., Biermann, T., Heiskanen, J., Lindroth, A., Peltola, O., Rantakari, M., Vesala, T., & Mammarella, I. (2018). Methane and carbon dioxide fluxes over a lake: Comparison between eddy covariance, floating chambers and boundary layer method. *Biogeosciences*, *15*(2), 429–445. https://doi.org/10.5194/bg-15-429-2018

Esters, L., Landwehr, S., Sutherland, G., Bell, T. G., Christensen, K. H., Saltzman, E. S., Miller, S. D., & Ward, B. (2017). Parameterizing air-sea gas transfer velocity with dissipation. *Journal of Geophysical Research: Oceans*, *122*(4), 3041–3056. https://doi.org/10.1002/2016JC012088

Eugster, W. (2003). CO 2 exchange between air and water in an Arctic Alaskan and midlatitude Swiss lake: Importance of convective mixing. *Journal of Geophysical Research*, *108*(D12), 4362. https://doi.org/10.1029/2002JD002653

Eugster, W., Kling, G., Jonas, T., McFadden, J. P., Wüest, A., MacIntyre, S., & Stuart, F. C. I. (2003). CO2 exchange between air and water in an Arctic Alaskan and midlatitude Swiss lake: Importance of convective mixing. *Journal of Geophysical Research*, *108*(D12), 4362. https://doi.org/10.1029/2002JD002653

Fearnside, P. M. (2015). Emissions from tropical hydropower and the IPCC. *Environmental Science and Policy*, *50*, 225–239. https://doi.org/10.1016/j.envsci.2015.03.002

Galy-Lacaux, C. (1999). Long-term greenhouse gas emissions from hydroelectric reservoirs in tropical forest regions. *Global Biogeochemical Cycles*, *13*(2), 503–517.

Galy-lacaux, C., Delmas, R., Labroue, L., & Gosse, P. (1997). Gaseous emissions and oxygen consumption in hydroelectric dams: A case study in French Guyana. *Global Biogeochem. Cycles*, *11*(4), 471–483.

Goring, D. G., & Nikora, V. I. (2002). Despiking acoustic doppler velocimeter data. *Journal of Hydraulic Engineering*, *128*(1), 117–126. https://doi.org/10.1061/(ASCE)0733-9429(2002)128:1(117)

Grossart, H. P., Frindte, K., Dziallas, C., Eckert, W., & Tang, K. W. (2011). Microbial methane production in oxygenated water column of an oligotrophic lake. *Proceedings of the National Academy of Sciences of the United States of America*, *108*(49), 19657–19661. https://doi.org/10.1073/pnas.1110716108

Guérin, F., & Abril, G. (2007). Significance of pelagic aerobic methane oxidation in the methane and carbon budget of a tropical reservoir. *Journal of Geophysical Research: Biogeosciences*, *112*(3), 1–14. https://doi.org/10.1029/2006JG000393

Guérin, F., Abril, G., de Junet, A., & Bonnet, M. P. (2008). Anaerobic decomposition of tropical soils and plant material: Implication for the CO2 and CH4 budget of the Petit Saut Reservoir. *Applied Geochemistry*, *23*(8), 2272–2283. https://doi.org/10.1016/j.apgeochem.2008.04.001

Guérin, F., Abril, G., Richard, S., Burban, B., Reynouard, C., Seyler, P., & Delmas, R. (2006). Methane and carbon dioxide emissions from tropical reservoirs: Significance of downstream rivers. *Geophysical Research Letters*, *33*(21), 1–6. https://doi.org/10.1029/2006GL027929

Guérin, F., Abril, G., Serça, D., Delon, C., Richard, S., Delmas, R., Tremblay, A., & Varfalvy, L. (2007a). Gas transfer velocities of CO2 and CH4 in a tropical reservoir and its river downstream. *Journal of Marine Systems*, *66*(1–4), 161–172. https://doi.org/10.1016/j.jmarsys.2006.03.019

Guérin, F., Abril, G., Serça, D., Delon, C., Richard, S., Delmas, R., Tremblay, A., & Varfalvy, L. (2007b). Gas transfer velocities of CO2 and CH4 in a tropical reservoir and its river downstream. *Journal of Marine Systems*, *66*(1–4), 161–172. https://doi.org/10.1016/j.jmarsys.2006.03.019

Günthel, M., Donis, D., Kirillin, G., Ionescu, D., Bizic, M., McGinnis, D. F., Grossart, H. P., & Tang, K. W. (2019). Contribution of oxic methane production to surface methane emission in lakes and its global importance. *Nature Communications*, *10*(1), 1–10. https://doi.org/10.1038/s41467-019-13320-0

Guseva, S., Aurela, M., Cortés, A., Kivi, R., Lotsari, E., MacIntyre, S., Mammarella, I., Ojala, A., Stepanenko, V., Uotila7, P., Vähä7, A., Vesala, T., Wallin, M. B., & A. Lorke. (2021). Variable Physical Drivers of Near-Surface Turbulence in a Regulated River Water Resources Research. *Water Resources Research*, *57*, 1–27. https://doi.org/10.1029/2020WR027939

Harrison, E. L., & Veron, F. (2017). Near-surface turbulence and buoyancy induced by heavy rainfall. *Journal of Fluid Mechanics*, *830*, 602–630. https://doi.org/10.1017/jfm.2017.602

Harrison, E. L., Veron, F., Ho, D. T., Reid, M. C., Orton, P., & McGillis, W. R. (2012). Nonlinear interaction between rain- and wind-induced air-water gas exchange. *Journal of Geophysical Research: Oceans*, *117*(3), 1–16. https://doi.org/10.1029/2011JC007693

Hersbach, H., Bell, B., Berrisford, P., Hirahara, S., Horányi, A., Muñoz-Sabater, J., Nicolas, J., Peubey, C., Radu, R., Schepers, D., Simmons, A., Soci, C., Abdalla, S., Abellan, X., Balsamo, G., Bechtold, P., Biavati, G., Bidlot, J., Bonavita, M., … Thépaut, J.

(2020). The ERA5 global reanalysis. *Quarterly Journal of the Royal Meteorological Society*, *146*(730), 1999–2049. https://doi.org/10.1002/qj.3803

Ho, D. T., Asher, W. E., Bliven, L. F., Schlosser, P., & Gordan, E. L. (2000). On mechanisms of rain-induced air-water gas exchange. *Journal of Geophysical Research: Oceans*, *105*(C10), 24045–24057. https://doi.org/10.1029/1999jc000280

Ho, D. T., Bliven, L. F., Wanninkhof, R., & Schlosser, P. (1997). The effect of rain on air-water gas exchange. *Tellus B: Chemical and Physical Meteorology*, *49*(2), 149–158. https://doi.org/10.3402/tellusb.v49i2.15957

Ho, D. T., Engel, V. C., Ferrón, S., Hickman, B., Choi, J., & Harvey, J. W. (2018). On Factors Influencing Air-Water Gas Exchange in Emergent Wetlands. *Journal of Geophysical Research: Biogeosciences*, *123*(1), 178–192. https://doi.org/10.1002/2017JG004299

Ho, D. T., Veron, F., Harrison, E., Bliven, L. F., Scott, N., & McGillis, W. R. (2007). The combined effect of rain and wind on air-water gas exchange: A feasibility study. *Journal of Marine Systems*, *66*(1–4), 150–160. https://doi.org/10.1016/j.jmarsys.2006.02.012

Ho, D. T., Zappa, C. J., McGillis, W. R., Bliven, L. F., Ward, B., Dacey, J. W. H., Scholosser, P., & Hendricks, M. B. (2004). Influence of rain on air-sea gas exchange: Lessons from a model ocean. *Journal of Geophysical Research C: Oceans*, *109*(8). https://doi.org/10.1029/2003JC001806

Hope, D., Dawson, J. J. C., Cresser, M. S., & Billett, M. F. (1995). A method for measuring free CO2 in upland streamwater using headspace analysis. *Journal of Hydrology*, *166*, 1–14.

Huotari, J., Ojala, A., Peltomaa, E., Nordbo, A., Launiainen, S., Pumpanen, J., Rasilo, T., Hari, P., & Vesala, T. (2011). Long-term direct CO 2 flux measurements over a boreal lake: Five years of eddy covariance data. *Geophysical Research Letters*, *38*(18), n/a-n/a. https://doi.org/10.1029/2011GL048753

Inc, E. (n.d.). *User Manual eosFDCO 2 eosFD Forced Diffusion Chamber and Software, version 2.4* (p. 28).

IPCC. (1990). *Resumen General del IPCC*. 57–70.

IPCC. (2019). *Refinement to the 2006 IPCC Guidelines for National Greenhouse Gas Inventories* (E. Calvo Buendia, K. Tanabe, A. Kranjc, B. Jamsranjav, M. Fukuda, S.

Ngarize, A. Osako, Y. Pyrozhenko, P. Shermanau, & S. Federici, Eds.). IPCC. https://doi.org/10.21513/0207-2564-2019-2-05-13

Jähne, B., Münnich, K. O., Bösinger, R., Dutzi, A., Huber, W., & Libner, P. (1987). On the parameters influencing air-water gas exchange. *Journal of Geophysical Research*, *92*(C2), 1937–1949. https://doi.org/10.1029/JC092iC02p01937

Jones, B. K., Saylor, J. R., & Testik, F. Y. (2010). *Raindrop Morphodynamics*.

Jorgensen, S. E., Loffler, H., RAst, W., & Straskraba, M. (2005). *Lake and Reservoir Management* (1st Editio). Elsevier Science.

Katul, G., & Liu, H. (2017). Multiple mechanisms generate a universal scaling with dissipation for the air-water gas transfer velocity. *Geophysical Research Letters*, *44*, 1–7. https://doi.org/10.1002/2016GL072256

Käufer, T., König, J., & Cierpka, C. (2021). Stereoscopic PIV measurements using low-cost action cameras. *Experiments in Fluids*, *62*(3), 1–16. https://doi.org/10.1007/s00348-020-03110-6

Kemenes, A., Agricultural, B., & Barbara, S. (2016). Downstream emissions of CH4 and CO2 from hydroelectric reservoirs (Tucuruí , Samuel , and Curuá-Una) in the ... *Inland Waters*, *1*(1), 1–10. https://doi.org/10.5268/IW-6.3.980

Kemenes, A., Forsberg, B. R., & Melack, J. M. (2011). CO2 emissions from a tropical hydroelectric reservoir. *Journal of Geophysical Research*, *116*(June 2010), 1–11. https://doi.org/10.1029/2010JG001465

Kocsis, O., Prandke, H., Stips, A., Simon, A., & Wüest, A. (1999). Comparison of dissipation of turbulent kinetic energy determined from shear and temperature microstructure. *Journal of Marine Systems*, *21*(1–4), 67–84. https://doi.org/10.1016/S0924-7963(99)00006-8

Koschorreck, M., Prairie, Y. T., Kim, J., & Marcé, R. (2021). Technical note : CO2 is not like CH4 – limits of and corrections to the headspace method to analyse pCO 2 in fresh water. *Biogeosciences*, *18*, 1619–1627. https://doi.org/10.5194/bg-18-1619-2021

Lamont, J. C., & Scott, D. S. (1970). An Eddy Cell Model of Mass Transfer into the Surface of a Turbulent Liquid. *AIChE Journal*, *16*(4), 513–519. https://doi.org/10.1002/aic.690160403

Le Quéré, C., Andrew, R. M., Friedlingstein, P., Sitch, S., Pongratz, J., Manning, A. C., Korsbakken, J. I., Peters, G. P., Canadell, J. G., Jackson, R. B., Boden, T. A., Tans,

P. P., Andrews, O. D., Arora, V. K., Bakker, D. C. E., Van Der Laan-Luijkx, I. T., Van Der Werf, G. R., Van Heuven, S., Viovy, N., … Zhu, D. (2018). 1. Carbon cycle-Global Carbon Budget 2017. *Earth Syst. Sci. Data Etsushi Kato Markus Kautz Ralph F. Keeling Kees Klein Goldewijk Nathalie Lefèvre Andrew Lenton Danica Lombardozzi Nicolas Metzl Yukihiro Nojiri Antonio Padin Janet Reimer*, *1010333739*(10), 405–448. https://doi.org/10.5194/essd-10-405-2018

Lin, L., Lu, X., Liu, S., Liong, S., & Fu, K. (2019). Physically controlled CO2 effluxes from a reservoir surface in the upper Mekong River Basin: a case study in the Gongguoqiao Reservoir. *Biogeosciences*, *16*, 2205–2219. https://doi.org/10.5194/bg-16-2205-2019

Liu, H., Zhang, Q., Katul, G. G., Cole, J. J., Chapin III, F. S., & MacIntyre, S. (2016). Large CO2 effluxes at night and during synoptic weather events significantly contribute to CO2 emissions from a reservoir. *Environmental Research Letters*, *11*(6), 1–8. https://doi.org/10.1088/1748-9326/11/6/064001

Lorke, A., & Peeters, F. (2006). Toward a Unified Scaling Relation for Interfacial Fluxes. *Journal of Physical Oceanography*, *36*(5), 955–961. https://doi.org/10.1175/JPO2903.1

Lueck, R. (2016). *RSI Technical Note 028. Calculating the Rate of Dissipation of Turbulent Kinetic Energy*. Rockland Scientific Inc.

Lueck, R., Scientific, R., Wolk, F., Scientific, R., & Black, K. (2013). *Measuring Tidal Channel Turbulence with a Vertical Microstructure Profiler (VMP)*. Rockland Scientific Inc.

Ma, X., & Green, S. A. (2004). Photochemical Transformation of Dissolved Organic Carbon in Lake Superior—An In-situ Experiment. *Journal of Great Lakes Research*, *30*, 97–112. https://doi.org/10.1016/S0380-1330(04)70380-9

MacIntyre, S., Jonsson, A., Jansson, M., Aberg, J., Turney, D. E., & Miller, S. D. (2010). Buoyancy flux, turbulence, and the gas transfer coefficient in a stratified lake. *Geophysical Research Letters*, *37*(24), 2–6. https://doi.org/10.1029/2010GL044164

MacIntyre, S., Romero, J., & Kling, G. W. (2002). Spatial-temporal variability in surface layer deepening and lateral advection in an embayment of Lake Victoria, East Africa. *Limnology and Oceanography*, *47*(3), 656–671. https://doi.org/10.4319/lo.2002.47.3.0656

Melack, J. M., Basso, L. S., Fleischmann, A. S., Botía, S., Guo, M., Zhou, W., Barbosa, P. M., Amaral, J. H. F., & MacIntyre, S. (2022). Challenges Regionalizing Methane Emissions Using Aquatic Environments in the Amazon Basin as Examples. *Frontiers in Environmental Science*, *10*(May), 1–26. https://doi.org/10.3389/fenvs.2022.866082

Melack, J. M., Hess, L. L., Gastil, M., Forsberg, B. R., Hamilton, S. K., Lima, I. B. T., & Novo, E. M. L. M. (2004). Regionalization of methane emissions in the Amazon Basin with microwave remote sensing. *Global Change Biology*, *10*(5), 530–544. https://doi.org/10.1111/j.1365-2486.2004.00763.x

Monismith, S. G., & MacIntyre, S. (2009). The Surface Mixed Layer in Lakes and Reservoirs. *Encyclopedia of Inland Waters*, *1*, 636–650. https://doi.org/10.1016/B978-012370626-3.00078-8

Oakey, N. S. (1982). Determination of the Rate of Dissipation of Turbulent Energy from Simultaneous Temperature and Velocity Shear Microstructure Measurements. *Journal of Physical Oceanography*, *12*, 256–271.

Obernosterer, I., & Benner, R. (2004). Competition between biological and photochemical processes in the mineralization of dissolved organic carbon. *Limnology and Oceanography*, *49*(1), 117–124. https://doi.org/10.4319/lo.2004.49.1.0117

Ojala, A., Bellido, J. L., Tulonen, T., Kankaala, P., & Huotari, J. (2011). Carbon gas fluxes from a brown-water and a clear-water lake in the boreal zone during a summer with extreme rain events. *Limnology and Oceanography*, *56*(1), 61–76. https://doi.org/10.4319/lo.2011.56.1.0061

Opperman, J., Hartmann, J., & Justus, R. (2017). *The Power of Rivers A Business Case*.

Osborn, T. R. (1980). Estimates of the Local Rate of Vertical Diffusion from Dissipation Measurements. *Journal of Physical Oceanography*, *10*(1), 83–89. https://doi.org/10.1175/1520-0485(1980)010<0083:EOTLRO>2.0.CO;2

Pacheco, F. S., Roland, F., & Downing, J. A. (2013). Eutrophication reverses whole-lake carbon budgets. *Inland Waters*, *4*(1), 41–48. https://doi.org/10.5268/IW-4.1.614

Pacheco, F. S., Soares, M. C. S., Assireu, A. T., Curtarelli, M. P., Abril, G., Stech, J. L., Alvalá, P. C., & Ometto, J. P. (2015). The effects of river inflow and retention time on the spatial heterogeneity of chlorophyll and water-air CO2 fluxes in a tropical hydropower reservoir. *Biogeosciences*, *12*(1), 147–162. https://doi.org/10.5194/bg-12-147-2015

Panneer Selvam, B., Natchimuthu, S., Arunachalam, L., & Bastviken, D. (2014). Methane and carbon dioxide emissions from inland waters in India - implications for large scale greenhouse gas balances. *Global Change Biology*, *20*(11), 3397–3407. https://doi.org/10.1111/gcb.12575

Paranaíba, J. R., Barros, N., Mendonça, R., Linkhorst, A., Isidorova, A., Roland, F., Almeida, R. M., & Sobek, S. (2018a). Spatially Resolved Measurements of CO2 and CH4 Concentration and Gas-Exchange Velocity Highly Influence Carbon-Emission Estimates of Reservoirs. *Environmental Science and Technology*, *52*(2), 607–615. https://doi.org/10.1021/acs.est.7b05138

Paranaíba, J. R., Barros, N., Mendonça, R., Linkhorst, A., Isidorova, A., Roland, F., Almeida, R. M., & Sobek, S. (2018b). Spatially Resolved Measurements of CO2and CH4Concentration and Gas-Exchange Velocity Highly Influence Carbon-Emission Estimates of Reservoirs. *Environmental Science and Technology*, *52*(2), 607–615. https://doi.org/10.1021/acs.est.7b05138

Peeters, F., & Kipfer, R. (2009). Currents in stratified water bodies 1: Density-driven flows. In *Encyclopedia of Inland Waters* (pp. 530–538). https://doi.org/DOI: 10.1016/B978-012370626-3.00080-6

Peirson, W. L., Beyá, J. F., Banner, M. L., Peral, J. S., & Azarmsa, S. A. (2013). Rain-induced attenuation of deep-water waves. *Journal of Fluid Mechanics*, *724*, 5–35. https://doi.org/10.1017/jfm.2013.87

Poindexter, C. M., Baldocchi, D. D., Matthes, J. H., Knox, S. H., & Variano, E. A. (2016). The contribution of an overlooked transport process to a wetland's methane emissions. *Geophysical Research Letters*, *43*(12), 6276–6284. https://doi.org/10.1002/2016GL068782

Rantakari, M., Heiskanen, J., Mammarella, I., Tulonen, T., Linnaluoma, J., Kankaala, P., & Ojala, A. (2015). Different Apparent Gas Exchange Coefficients for CO2 and CH4: Comparing a Brown-Water and a Clear-Water Lake in the Boreal Zone during the Whole Growing Season. *Environmental Science and Technology*, *49*(19), 11388–11394. https://doi.org/10.1021/acs.est.5b01261

Raymond, P. A., Hartmann, J., Lauerwald, R., Sobek, S., McDonald, C., Hoover, M., Butman, D., Striegl, R., Mayorga, E., Humborg, C., Kortelainen, P., Dürr, H., Meybeck, M., Ciais, P., & Guth, P. (2013). Global carbon dioxide emissions from inland waters. *Nature*, *503*, 355–359. https://doi.org/10.1038/nature12760

Raymond, P. A., Zappa, C. J., Butman, D., Bott, T. L., Potter, J., Mulholland, P., Laursen, A. E., Mcdowell, W. H., & Newbold, D. (2012). Scaling the gas transfer velocity and hydraulic geometry in streams and small rivers. *Limnology and Oceanography*, *2*, 41–53. https://doi.org/10.1215/21573689-1597669

Read, J. S., Hamilton, D. P., Desai, A. R., Rose, K. C., Macintyre, S., Lenters, J. D., Smyth, R. L., Hanson, P. C., Cole, J. J., Staehr, P. A., Rusak, J. A., Pierson, D. C., Brookes, J. D., Laas, A., & Wu, C. H. (2012). Lake-size dependency of wind shear and convection as controls on gas exchange. *Geophysical Research Letters*, *39*, 1–5. https://doi.org/10.1029/2012GL051886

Risk, D., Nickerson, N., Creelman, C., McArthur, G., & Owens, J. (2011). Forced Diffusion soil flux: A new technique for continuous monitoring of soil gas efflux. *Agricultural and Forest Meteorology*, *151*(12), 1622–1631. https://doi.org/10.1016/j.agrformet.2011.06.020

Rocha Lessa, A. C., dos Santos, M. A., Lewis Maddock, J. E., & dos Santos Bezerra, C. (2015). Emissions of greenhouse gases in terrestrial areas pre-existing to hydroelectric plant reservoirs in the Amazon: The case of Belo Monte hydroelectric plant. *Renewable and Sustainable Energy Reviews*, *51*, 1728–1736. https://doi.org/http://dx.doi.org/10.1016/j.rser.2015.07.067

Rodriguez, M., & Casper, P. (2018). Greenhouse gas emissions from a semi-arid tropical reservoir in northeastern Brazil. *Regional Environmental Change*, *18*(7), 1901–1912. https://doi.org/10.1007/s10113-018-1289-7

Roland, F., Vidal, L. O., Pacheco, F. S., Barros, N. O., Assireu, A., Ometto, J. P. H. B., Cimbleris, A. C. P., & Cole, J. J. (2010). Variability of carbon dioxide flux from tropical (Cerrado) hydroelectric reservoirs. *Aquatic Sciences*, *72*(3), 283–293. https://doi.org/10.1007/s00027-010-0140-0

Rooney, G. G., van Lipzig, N., & Thiery, W. (2018). Estimating the effect of rainfall on the surface temperature of a tropical lake. *Hydrology and Earth System Sciences*, *22*(12), 6357–6369. https://doi.org/10.5194/hess-22-6357-2018

Rosentreter, J. A., Borges, A. V., Deemer, B. R., Holgerson, M. A., Liu, S., Song, C., Melack, J., Raymond, P. A., Duarte, C. M., Allen, G. H., Olefeldt, D., Poulter, B., Battin,

T. I., & Eyre, B. D. (2021). Half of global methane emissions come from highly variable aquatic ecosystem sources. *Nature Geoscience*, *14*(4), 225–230. https://doi.org/10.1038/s41561-021-00715-2

Rudd, J. W. M. (1993). Are hydroelectric reservoirs significant sources of greenhouse gases. *Ambio*, *22*(4), 246–248.

Rudd, J. W. M., Furunati, A., Flett, R. J., & Hamilton, R. D. (1976). Factors controlling methane oxidation in shield lakes : The role of nitrogen fixation and oxygen concentration1. *Limnology and Oceanography*, *21*(3), 357–364.

Santoso, A. B., Hamilton, D. P., Schipper, L. A., Ostrovsky, I. S., & Hendy, C. H. (2020). High contribution of methane in greenhouse gas emissions from a eutrophic lake : a mass balance synthesis. *New Zealand Journal of Marine and Freshwater Research*, 1–20. https://doi.org/10.1080/00288330.2020.1798476

Schlesinger, W. H., & Bernhardt, E. S. (2013). *Biogeochemistry: An Analysis of Global Change*. Academic Press.

Serio, M. A., Carollo, F. G., & Ferro, V. (2019). Raindrop size distribution and terminal velocity for rainfall erosivity studies . A review. *Journal of Hydrology*, *576*(February), 210–228. https://doi.org/10.1016/j.jhydrol.2019.06.040

Shao, C., Chen, J., Stepien, C. A., Chu, H., Ouyang, Z., Bridgeman, T. B., Czajkowski, K. P., Becker, R. H., & John, R. (2015). Diurnal to annual changes in latent, sensible heat, and CO2 fluxes over a Laurentian Great Lake: A case study in Western Lake Erie. *Journal of Geophysical Research: Biogeosciences*, *120*, 1587–1604. https://doi.org/10.1002/2015JG003025.Received

Siddiqui, M. H. K., & Loewen, M. R. (2007). Characteristics of the wind drift layer and microscale breaking waves. *J. Fluid Mech.*, *573*, 417–456. https://doi.org/10.1017/S0022112006003892

Soued, C., & Prairie, Y. T. (2021). Changing sources and processes sustaining surface CO2 and CH4 fluxes along a tropical river to reservoir system. *Biogeosciences*, *18*(4), 1333–1350. https://doi.org/10.5194/bg-18-1333-2021

Soumis, N., Lucotte, M., Caneul, R., Weissenberger, S., Houel, S., Larose, C., & Duchemin, E. (2005). Hydroelectric Reservoirs as Anthropogenic sources of greenhouse gases. In *Water Encyclopedia: Surface and Agricultural Water* (pp. 203–210). https://doi.org/10.1002/047147844X.sw791

Spafford, L., & Risk, D. (2018). Spatiotemporal Variability in Lake-Atmosphere Net CO2 Exchange in the Littoral Zone of an Oligotrophic Lake. *Journal of Geophysical Research: Biogeosciences*, *123*(4), 1260–1276. https://doi.org/10.1002/2017JG004115

St. Louis, V. L., Kelly, C. A., Duchemin, É., Rudd, J. W. M., & Rosenberg, D. M. (2000). Reservoir Surfaces as Sources of Greenhouse Gases to the Atmosphere: A Global Estimate. *BioScience*, *50*(9), 766. https://doi.org/10.1641/0006-3568(2000)050[0766:RSASOG]2.0.CO;2

Stumm, W., & Morgan, J. J. (1996). Chemical Equilibria and Rates in Natural Waters. In *Aquatic chemistry*.

Takagaki, N., & Komori, S. (2007). Effects of rainfall on mass transfer across the air-water interface. *Journal of Geophysical Research: Oceans*, *112*(6), 1–11. https://doi.org/10.1029/2006JC003752

Takagaki, N., & Komori, S. (2014). Air – water mass transfer mechanism due to the impingement of a single liquid drop on the air – water interface. *INTERNATIONAL JOURNAL OF MULTIPHASE FLOW*, *60*, 30–39. https://doi.org/10.1016/j.ijmultiphaseflow.2013.11.006

Tang, K. W., McGinnis, D. F., Frindte, K., Brüchert, V., & Grossart, H. P. (2014). Paradox reconsidered: Methane oversaturation in well-oxygenated lake waters. *Limnology and Oceanography*, *59*(1), 275–284. https://doi.org/10.4319/lo.2014.59.1.0275

Tang, K. W., McGinnis, D. F., Ionescu, D., & Grossart, H. P. (2016). Methane production in oxic lake waters potentially increases aquatic methane flux to air. *Environmental Science and Technology Letters*, *3*(6), 227–233. https://doi.org/10.1021/acs.estlett.6b00150

Tennekes, H., & Lumley, J. L. (1972). *A FIRST COURSE IN TURBULENCE*. The Massachusetts Institute of Technology.

Thielicke, W. (2014). *The Flapping Flight of Birds: Analysis and application*. https://doi.org/10.1017/s036839310013768x

Thielicke, W., & Sonntag, R. (2021). Particle Image Velocimetry for MATLAB: Accuracy and enhanced algorithms in PIVlab. *Journal of Open Research Software*, *9*(June), 1–14. https://doi.org/10.5334/JORS.334

Thielicke, W., & Stamhuis, E. J. (2014). PIVlab – Towards User-friendly, Affordable and Accurate Digital Particle Image Velocimetry in MATLAB. *Journal of Open Research Software*, *2*, 1–10. https://doi.org/10.5334/jors.bl

Toledo, A., Talarico, M., Chinez, S., & Agudo, E. (1983). *The application of simplified models for eutrophication process evaluation in tropical lakes and reservoirs* (pp. 1–34). ABES (Brazilian Association of Sanitary Engineering).

Treut, L., Somerville, R., Cubasch, U., Ding, Y., Mauritzen, C., Mokssit, a, Peterson, T., Prather, M., Qin, D., Manning, M., Chen, Z., Marquis, M., Averyt, K. B., & Tignor, M. (2007). Historical Overview of Climate Change Science. *Earth*, *Chapter 1*(October), 93–127. https://doi.org/10.1016/j.soilbio.2010.04.001

Turk, D., Zappa, C. J., Meinen, C. S., Christian, J. R., Ho, D. T., Dickson, A. G., & McGillis, W. R. (2010). Rain impacts on CO2 exchange in the western equatorial Pacific Ocean. *Geophysical Research Letters*, *37*(23), 1–6. https://doi.org/10.1029/2010GL045520

UPME. (2016a). Boletín Estadístico: Minas y energía 2012 – 2016. *Ministerio de Minas y Energía*, 200.

UPME. (2016b). *Plan de expansión de referencia. Generación-Transmisión. 2016-2030*. 477.

Vachon, D., Prairie, Y. T., & Cole, J. J. (2010). The relationship between near-surface turbulence and gas transfer velocity in freshwater systems and its implications for floating chamber measurements of gas exchange. *Limnology and Oceanography*, *55*(4), 1723–1732. https://doi.org/10.4319/lo.2010.55.4.1723

van Boxel, J. (1998). Numerical model for the fall speed of raindrops in a rainfall simulator. *I.C.E. Special Report*, *1998/1*, 77–85.

Verburg, P., & Antenucci, J. P. (2010). Persistent unstable atmospheric boundary layer enhances sensible and latent heat loss in a tropical great lake: Lake Tanganyika. *Journal of Geophysical Research*, *115*(D11109), 1–13. https://doi.org/10.1029/2009JD012839

Wallin, M. B., Chmiel, H. E., Kokic, J., Denfeld, B. A., Sobek, S., Koehler, B., Isidorova, A., Bastviken, D., Eve, M.-, Einarsdóttir, K., Wallin, M. B., Koehler, B., Isidorova, A., Bastviken, D., Ferland, M. È., & Sobek, S. (2016). The role of sediments in the carbon budget of a small boreal lake. *Limnology and Oceanography*, *61*(5), 1814–1825. https://doi.org/10.1002/lno.10336

Wanninkhof, R. (1992). Relationship between wind speed and gas exchange over the ocean. *Journal of Geophysical Research*, *97*(C5), 7373–7382. https://doi.org/10.1029/92JC00188

Wanninkhof, R. (2014). Relationship between wind speed and gas exchange over the ocean revisited. *Limnology and Oceanography: Methods*, *12*, 351–362. https://doi.org/10.4319/lom.2014.12.351

West, W. E., Coloso, J. J., & Jones, S. E. (2012). Effects of algal and terrestrial carbon on methane production rates and methanogen community structure in a temperate lake sediment. *Freshwater Biology*, *57*(5), 949–955. https://doi.org/10.1111/j.1365-2427.2012.02755.x

West, W. E., Creamer, K. P., & Jones, S. E. (2016). Productivity and depth regulate lake contributions to atmospheric methane. *Limnology and Oceanography*, *61*, S51–S61. https://doi.org/10.1002/lno.10247

Winter, T. C. (2004). The Hydrology of Lakes. In P. E. O'Sullivan & C. S. Reynolds (Eds.), *The Lakes Handbook* (pp. 61–78).

Wüest, A., & Lorke, A. (2003). Small-Scale Hydrodynamics in Lakes. *Annual Reviews of Fluid Mechanics*, *35*(Section 3), 373–412. https://doi.org/10.1146/annurev.fluid.35.101101.161220

Wüest, A., & Lorke, A. (2009). Small-Scale Turbulence and Mixing: Energy Fluxes in Stratified Lakes. In *Encyclopedia of Inland Waters* (Vol. 1, pp. 628–635). https://doi.org/DOI: 10.1016/B978-012370626-3.00084-3

Xu, Y. J., Xu, Z., & Yang, R. (2019). Rapid daily change in surface water pCO2 and CO2 evasion: A case study in a subtropical eutrophic lake in Southern USA. *Journal of Hydrology*, *570*, 486–494. https://doi.org/10.1016/j.jhydrol.2019.01.016

Yang, L., Lu, F., Zhou, X., Wang, X., Duan, X., & Sun, B. (2014). Progress in the studies on the greenhouse gas emissions from reservoirs. *Acta Ecologica Sinica*, *34*(4), 204–212. https://doi.org/10.1016/j.chnaes.2013.05.011

Yang, R., Chen, Y., Du, J., Pei, X., Li, J., Zou, Z., & Song, H. (2022). Daily Variations in pCO2 and fCO2 in a Subtropical Urbanizing Lake. *Frontiers in Earth Science*, *9*(January), 1–16. https://doi.org/10.3389/feart.2021.805276

Yang, Y., Chen, J., Tong, T., Li, B., He, T., Liu, Y., & Xie, S. (2019). Eutrophication influences methanotrophic activity, abundance and community structure in freshwater lakes. *Science of the Total Environment*, *662*, 863–872. https://doi.org/10.1016/j.scitotenv.2019.01.307

Zappa, C. J., Ho, D. T., McGillis, W. R., Banner, M. L., Dacey, J. W. H., Bliven, L. F., Ma, B., & Nystuen, J. (2009). Rain-induced turbulence and air-sea gas transfer. *Journal of Geophysical Research: Oceans*, *114*(7), 1–17. https://doi.org/10.1029/2008JC005008

Zappa, C. J., Mcgillis, W. R., Raymond, P. A., Edson, J. B., Hintsa, E. J., Zemmelink, H. J., Dacey, J. W. H., & Ho, D. T. (2007). Environmental turbulent mixing controls on air-water gas exchange in marine and aquatic systems. *Geophysical Research Letters*, *34*, 1–6. https://doi.org/10.1029/2006GL028790